Nanomaterials in Joining

Constantinos A. Charitidis

Constantinos A. Charitidis

Nanomaterials in Joining

Also of interest

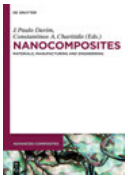

Series: Advanced Composites
J. Paulo Davim (Ed.)
ISSN 2192-8983
Published titles in this series:
Vol. 4: Machinability of Fibre-Reinforced Plastics (2015) Ed. By Davim, J. Paulo
Vol. 3: Metal Matrix Composites (2014) Ed. by Davim, J. Paulo
Vol. 2: Biomedical Composites (2013) Ed. by Davim, J. Paulo
Vol. 1: Nanocomposites (2013) Ed. by Davim, J. Paulo/Charitidis, Constantinos A.
Botana and Sainz (Eds); 2015
ISBN 978-3-11-033305-3, e-ISBN 978-3-11-033361-9

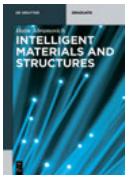

Intelligent Materials and Structures
Haim Abramovich, 2016
ISBN 978-3-11-033801-0, e-ISBN 978-3-11-033802-7

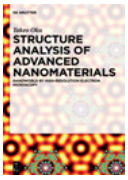

Structure Analysis of Advanced Nanomaterials: Nanoworld by High-Resolution Electron Microscopy
Takeo Oku, 2014
ISBN 978-3-11-030472-5, e-ISBN 978-3-11-030501-2

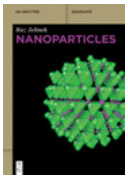

Nanoparticles
Raz Jelinek, 2015
ISBN 978-3-11-033002-1, e-ISBN 978-3-11-033003-8

Nanotechnology Reviews
Kumar, Challa (Editor-in-Chief)
ISSN 2191-9089, e-ISSN 2191-9097

Nanomaterials in Joining

Edited by
Constantinos A. Charitidis

DE GRUYTER

Editor
Prof. Dr. Constantinos A. Charitidis
National Technical University of Athens
15773 Athens
charitidis@chemeng.ntua.gr

ISBN 978-3-11-033960-4
e-ISBN (PDF) 978-3-11-033972-7
e-ISBN (EPUB) 978-3-11-038950-0
Set-ISBN 978-3-11-033973-4

Library of Congress Cataloging-in-Publication Data
A CIP catalog record for this book has been applied for at the Library of Congress.

Bibliographic information published by the Deutsche Nationalbibliothek
The Deutsche Nationalbibliothek lists this publication in the Deutsche Nationalbibliografie; detailed bibliographic data are available on the Internet at http://dnb.dnb.de.

Cover image: Galileo Satellite artist impression. *Credit@ESA-J.Huart*
Typesetting: PTP Protago-TEX-Production, Berlin
Printing and binding: CPI books GmbH, Leck
♾ Printed on acid-free paper
Printed in Germany

www.degruyter.com

Preface

Nanomaterials in Joining consists of chapters written by expert scientists and engineers from the international materials community who contribute important research works in the field of materials science and related subjects with emphasis on composite nanomaterials and dissimilar joints. These contributions focus on new applications of nanomaterials as fillers into polymeric and metallic matrices as well as on mechanical and structural characterization.

Nanomaterials are synthesized and characterized by such tools and techniques that combine multidisciplinary fields of physics, chemistry and engineering. By incorporating the appropriate nanomaterials as fillers into the matrices, enhancement of specific material properties, especially of those that depend on surface microstructure, is achieved.

This book was prepared for those who are seeking the most up-to-date information on the incorporation of carbon nanotubes into polymeric and metallic matrices, corrosion issues, and mechanical characterization of composite nanomaterials and dissimilar joints.

In the first chapter "Multiwalled carbon nanotubes – Strength to polymer composites", various carbon nanotubes are embedded inside epoxy resins with different surface modifications, so as to improve the mechanical properties. Better carbon nanotube dispersion (less agglomeration) and the absence of defects can achieve improved mechanical strength. This work suggests that even low quantity multiwalled carbon nanotubes could drastically change the behavior of the epoxy resin and open a series of new possible applications for this material.

In the second chapter "Dissimilar friction stir welding of aluminum alloys reinforced with carbon nanotubes", carbon nanotubes are incorporated as reinforcing fillers into dissimilar metal joints produced by friction stir welding, after process parameter optimization. The impact of this incorporation on the microstructure and mechanical properties of these joints is studied on both local and global level.

The next chapters are focused on the corrosion and corrosion protection of multimaterial assemblies.

In the chapter "Corrosion issues in joining lightweight materials: A review of the latest achievements", the author reviews the latest results of studies focused on corrosion issues while joining lightweight materials. The most common corrosion phenomena are observed and described in joined materials, emphasizing the corrosion issues in assemblies combining different metals and in assemblies combining metals with nonmetals. This chapter could prove to be particularly useful to a broader audience of readers who are searching for the latest information on corrosion issues in light-weight structures.

In the chapter "Protection of Multimaterial assemblies", different strategies for the protection of multimaterial structures are briefly overviewed. The main focus is on

the new alternative protection systems that are based on a combination of synergistic inhibiting mixtures introduced into protective coatings. A road map which can be followed in order to create an efficient active protection coating for hybrid structures is suggested.

In the last chapter "Failure of dissimilar material bonded joints" the authors present the basic failure mechanisms of bonded joints. The failure prediction of adhesively bonded joints is a complex undertaking, as there are several parameters that can cause premature failure. The recent developments in nanotechnology have increased the complexity of the fracture mechanics assessment of such joints, since the presence of nanoparticles introduces further parameters that influence crack initiation and propagation.

To sum up, this book will be useful to everyone who is interested in applications of nanomaterials and dissimilar joining, and is especially oriented towards graduate students and young researchers, aiming to facilitate their introduction to this novel area of research.

It is my pleasure to express my gratitude to all the contributors of the chapters in this book. I would like to acknowledge the superb assistance that the staff of De Gruyter has provided for the publication of this work.

Contents

Preface —— V

List of contributing authors —— IX

Pravin Jagdale, Aamer. A. Khan, Massimo Rovere, Carlo Rosso,
and Alberto Tagliaferro

1 Multiwalled Carbon nanotube – Strength to polymer composite —— 1
1.1 Introduction —— **1**
1.2 Material and methods —— **4**
1.2.1 Epoxy resin in general —— **4**
1.2.2 Epoxy resin in sample preparation —— **5**
1.2.3 Multi walled carbon nanotubes (MWCNTs) —— **5**
1.2.4 MWCNT Nanofiller epoxy composite preparation —— **6**
1.2.5 Preparation of epilox CNT nanocomposites —— **7**
1.3 Mechanical analysis —— **8**
1.4 FESEM details with sample preparation —— **11**
1.5 Results and discussion —— **11**
1.6 Ultimate tensile stress (UTS) —— **16**
1.6.1 Strain at break —— **16**
1.6.2 Yield point —— **16**
1.6.3 Resilience —— **18**
1.6.4 Toughness —— **18**
1.6.5 Young's modulus —— **19**
1.7 Conclusions —— **19**
1.8 Future trends —— **20**

D.I. Pantelis, P.N. Karakizis, D.A. Dragatogiannis, and C.A. Charitidis

2 Dissimilar friction stir welding of aluminum alloys reinforced with carbon nanotubes —— 23
2.1 Introduction —— **23**
2.2 Experimental procedure —— **26**
2.3 Results and discussion —— **29**
2.3.1 First series of experiments —— **29**
2.3.2 Second series of experiments —— **41**
2.4 Conclusions —— **49**

M.F. Montemor

3 Corrosion issues in joining lightweight materials: A review of the latest achievements —— 53
3.1 Introduction —— **53**

3.2 General aspects of corrosion in joints —— **54**
3.3 Corrosion in lightweight metallic joints —— **56**
3.3.1 Steel and lightweight metals —— **57**
3.3.2 Lightweight metals —— **59**
3.3.3 Coatings to minimize corrosion in multimetal assemblies —— **62**
3.4 Corrosion in metal-nonmetal joints —— **63**
3.4.1 Coatings to minimize corrosion in hybrid assemblies —— **66**
3.5 Future trends —— **67**

Mikhail L. Zheludkevich, Silvar Kallip, and Maria Serdechnova
4 Protection of multimaterial assemblies —— 73
4.1 Demands on light weight engineering and associated issues —— **73**
4.2 Approaches to mitigate corrosion issues in multimaterial systems —— **80**
4.2.1 Passive protection —— **80**
4.2.2 Active protective coatings with corrosion inhibitors —— **84**
4.3 Concluding remarks —— **96**

M. Konstantakopoulou, A. Deligianni, and G. Kotsikos
5 Failure of dissimilar material bonded joints —— 103
5.1 Introduction —— **103**
5.1.1 Adhesively bonded joints —— **104**
5.1.2 Effect of adhesive thickness —— **109**
5.1.3 Carbon nanotube-enhanced adhesively bonded joints —— **112**
5.2 Conclusions —— **118**

Index —— 123

List of contributing authors

C.A. Charitidis
Laboratory Unit of Advanced
Composite, Nano-Materials and Nanotechnology
School of Chemical Engineering
National Technical University of Athens
9 Heroon, Polytechneiou st., Zografos, Athens
GR-15773, Greece
charitidis@chemeng.ntua.gr

A. Deligianni
School of Mechanical & Systems Engineering
Stephenson Building
Newcastle University
Newcastle upon Tyne, NE1 7RU
United Kingdom

D.A. Dragatogiannis
Laboratory Unit of Advanced
Composite, Nano-Materials and Nanotechnology
School of Chemical Engineering
National Technical University of Athens
9 Heroon, Polytechneiou st., Zografos, Athens
GR-15773, Greece
ddragato@chemeng.ntua.gr

Pravin Jagdale
Department of Applied Science and Technology
(DISAT)
Politecnico di Torino
10129, Italy

Silvar Kallip
University of Aveiro
DEMAC/CICECO
3810-193 Aveiro, Portugal

P.N. Karakizis
Shipbuilding Technology Laboratory
School of Naval Architecture and Marine
Engineering
National Technical University of Athens
9 Heroon, Polytechniou st., Zografos, Athens
GR-157 80, Greece

Aamer. A. Khan
Department of Applied Science and Technology
(DISAT)
Politecnico di Torino
10129, Italy

G. Kotsikos
School of Mechanical & Systems Engineering
Stephenson Building
Newcastle University
Newcastle upon Tyne, NE1 7RU
United Kingdom
george.kotsikos@newcastle.ac.uk

M. Konstantakopoulou
School of Mechanical & Systems Engineering
Stephenson Building
Newcastle University
Newcastle upon Tyne, NE1 7RU
United Kingdom

M.F. Montemor
CQE, Instituto Superior Técnico
Universidade de Lisboa
Av. Rovisco Pais
1049-001 Lisboa, Portugal
mfmontemor@tecnico.ulisboa.pt

D.I. Pantelis
Shipbuilding Technology Laboratory
School of Naval Architecture and Marine
Engineering
National Technical University of Athens
9 Heroon, Polytechniou st., Zografos, Athens
GR-157 80, Greece

Carlo Rosso
Department of Mechanical and Aerospace
Engineering (DIMEAS)
Politecnico di Torino
10129, Italy

Massimo Rovere
Department of Applied Science and Technology (DISAT)
Politecnico di Torino
10129, Italy

Alberto Tagliaferro
Department of Applied Science and Technology (DISAT)
Politecnico di Torino
10129, Italy

Maria Serdechnova
MagIC, Institute of Materials Research
Helmholtz-Zentrum Geesthacht
Max Planck Straße 1
21502 Geesthacht, Germany

Mikhail L. Zheludkevich
MagIC, Institute of Materials Research
Helmholtz-Zentrum Geesthacht
Max Planck Straße 1
21502 Geesthacht, Germany
and
University of Aveiro
DEMAC/CICECO
3810-193 Aveiro, Portugal

Pravin Jagdale, Aamer. A. Khan, Massimo Rovere, Carlo Rosso, and Alberto Tagliaferro

1 Multiwalled Carbon nanotube – Strength to polymer composite

Abstract: Carbon nanotubes (CNTs), a rather fascinating material, are among the pillars of nanotechnology. CNTs exhibit unique electrical, mechanical, adsorption, and thermal properties with high aspect ratio, exceptional stiffness, excellent strength, and low density, which can be exploited in the manufacturing of revolutionary smart nano composite materials. The demand for lighter and stronger polymer composite material in various applications is increasing every day. Among all the possibilities to research and exploit the exceptional properties of CNTs in polymer composites we focused on the reinforcement of epoxy resin with different types of multiwalled carbon nano tubes (MWCNTs). We studied mechanical properties such as stress, strain, ultimate tensile strength, yield point, modulus and fracture toughness, and Young's modulus by plotting and calculating by means of the off-set method. The mechanical strength of epoxy composite is increased intensely with 1 and 3 wt.% of filler.

1.1 Introduction

Life on Earth is based on carbon. To create living matter from carbon, organisms carry out chemical reactions such as photosynthesis. This known mechanism of carbon fixation represents the largest bridge between the earth's nonliving chemistry and life. Carbon is known to be the most versatile element on earth [1]. Several allotropes of carbon are present in nature: the best known are graphite, diamond, and amorphous carbon. New nanostructured allotropes of carbon such as Bucky balls and nanotubes have been discovered in recent decades [2] and more recently other more exotic allotropes such as graphene [3, 4]. Carbon nanotubes (CNTs) are one of the fascinating carbon structures which has attracted a great deal of attention. CNTs of a nanoscale dimension (1-D) have become well known over the past 15 years, but according to Robert Floyd Curl, Jr., (chemistry, Nobel Prize in 1996), in ancient times Indian craftsmen used nanotechnology in wootz steel as well as in paintings. Marianne Reibold et al. (University of Dresden) discovered the dispersion of CNTs in Damascus steel, famous during the middle ages, which was extraordinarily strong and flexible [5]. In 1952, the Russian scientists Radushkevich et al. published clear images of tubes made of carbon 50 nanometers in diameter [6]. The term 'nanotubes' for carbon nanotubes was first used by Wiles and Abrahamson in 1978. In 1987 Hyperion Catalysis International (USA) published a series of patents on the production and the use of 'nanofibrils' in polymers as fillers [7]. The world made an increased acquaintance with CNTs after Iijima's detailed informative rediscovery in 1991 [8]. The first observations which Sumio made

were of multiwalled nanotubes [9]. Multiwalled carbon nanotubes (MWCNTs) are generally described as a type of hollow and lengthy concentric cylinder ranging from 6 to 25 or more graphite sheets on a nanoscopic level [10]. The separation between the graphene layers (interlayer spacing) is close to 0.34 nm [7, 11]. Graphene sheets are rolled at specific and discrete angles known as "chiral angles". The combination of the radius of the CNTs and the rolling angle defines the properties of the nanotube [12–15]. CNTs are available in three unique geometries (Fig. 1.1) which are armchair (n, n), chiral (n, m) and zigzag (n, 0), the number in parenthesis indicating the number of primitive vectors needed to close the tube. Their electrical characteristics differ depending on these variations, acting either as metals or as semiconductors.

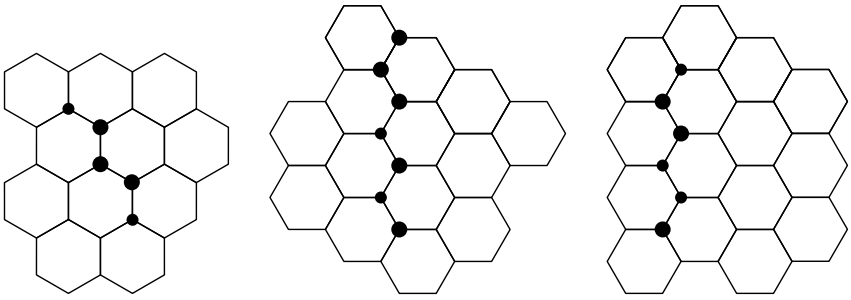

Fig. 1.1: Different form of chirality in CNT.

Who discovered carbon nanotubes is no longer as important as who can come up with the most practical applications. CNTs can be considered to be the next generation of carbon fibers [16]. CNTs have extraordinary mechanical strength in terms of tensile strength and elastic modulus. This property also made it popular in the fields of composites. The use of CNTs as filler in composites has been given significant attention because of their remarkable thermal, mechanical, electrical, and other properties [17–19]. A variety of matrices such as ceramics, metal, and polymer for nanocomposite study has been under investigation. Polymer nanocomposites are used in all industries ranging from civil, infrastructure, automobiles, electronic equipment, aerospace, and smart textile and military equipment. Lighter and stronger materials are what is needed at present, and polymer nanocomposites are perfect for this purpose. Polymer nanocomposite materials save energy, are easy to handle and process, possess a long life, and have adequate resistance to atmospheric conditions and chemicals [16, 22, 29].

The CNT filler used for polymer nano composite have different morphology, structure, and composition [20]. Even very small volume fractions of CNT in composites dramatically alter the composite properties such as electrical, optoelectronic,

thermal, and mechanical properties [21–24]. Polymer nanocomposite materials are organic polymer matrices containing dispersed inorganic/organic particulates having at least one dimension below 100 nm. The dispersion is aimed at improving the structural morphology, properties and the overall performance of the polymer (Table 1.1) [11, 12, 25–27]. Nanocomposites having outstanding mechanical properties and ultralight weight are already on the market [7, 20, 28–30].

Tab. 1.1: Characteristics and applications of nanofillers in polymer matrix composite materials [22].

Characteristics	Applications
Physical strength, specific toughness, light weight	Aerospace, construction, sporting goods
High dimensional stability, low coefficient of thermal expansion, low abrasion	Printed circuit boards, missile structures, aircraft brakes, aerospace antennas and support structures, large telescopes, optical benches, waveguides for stable high-frequency (gigahertz) precision measurement frames
Vibration damping, strength, toughness	Audio equipment, including microphones and speakers; robotic arms
Electrical conductivity	Airframes and aircraft skin materials, novel tooling, casings and bases for electronic equipment, electromagnetic interference (EMI) and radio frequency (RF) shielding, brushes
Low biological reactivity, permeability by x-rays	Medical prostheses, surgery and x-ray equipment, implants, tendon/ligament repair
Fatigue resistance, self-lubrication	General engineering applications with moving parts, such as automobiles
Low chemical reactivity, high corrosion resistance	Chemical exposure; radiation fields; valves, seals, and pump components
Electromagnetic properties	Electronic devices; motor and generator parts; radiological equipment

As we are considering nanocomposites based on epoxy resin, let us spend a few words on it here. The first commercial exploration of the properties of epoxy resins was by I.G. Farben Industries in Germany during the 1930s, and from that time on epoxy resins have been put to industrial uses more than any other resins. Epoxy resins adhere well to a wide variety of reinforcing agents. Their very low shrinkage [31–33] make them popular in composite industry. Epoxy resins in a cured state are very resistant to chemical influences and offer excellent electrical insulation.

The rising global demand for industrial applications like aerospace and wind energy industries is propelling research in epoxy resin composites. Epoxy resin-based composites provide flexibility and reduction of the overall weight of the material, enhancing the creep and fatigue resistance. The main applications of epoxy resin are found in formulations for mortars, screeds, and polymer concretes for adhesion primers and coatings in civil as well as mechanical engineering for corrosion protec-

tion [13], etc. Epoxy composites are used in specialized sophisticated structures and are the preferred choice where functionality is most importanct [34]. Epoxy resins do have some disadvantages, e.g. they are sensitive to moisture, and the heat distortion point, the dimensions, and the physical properties decrease with moisture take-up. High temperature affects their toughness: they have a high coefficient of thermal expansion when compared to other thermosets, are sensitive to UV, etc. There is still much need for researching and exploiting the exceptional properties of MWCNTs in epoxy polymer composites to tackle such limitations.

The focus in this chapter is on the reinforcement of epoxy resin with several types of MWCNTs to study their mechanical properties such as stress, strain, ultimate tensile strength, yield point, modulus, and fracture toughness.

1.2 Material and methods

1.2.1 Epoxy resin in general

Epoxy resins are thermosetting polymers that contain an epoxide ring of the basic functional group. The basic raw materials required for the production of epoxy resins include bisphenol A (BPA), epichlorohydrin, phenols, aromatic amines, and aliphatic alcohols. Epoxides are three-membered rings with two carbon atoms and one oxygen atom (Fig. 1.2).

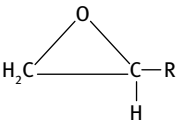

Fig. 1.2: Epoxide ring.

Epoxides can be classified as difunctional to polyfunctional epoxides. A curing agent/cross linker hardens the epoxides without releasing any byproduct compounds and with a minimal shrinkage to form a rigid material bearing high resistance to solvents and stable dimensions at elevated temperatures. Diglycidyl ether of bisphenol A with its repeating units is the most widely used difunctional epoxy, as shown in the Fig. 1.3.

Polyfunctional epoxy with aromatic and heterocyclic glycidyl amine groups are used for high-temperature aerospace applications. These compounds contain tetraglycidyl methylene dianiline, (TGMDA) groups which guarantee performance in such conditions [31, 32].

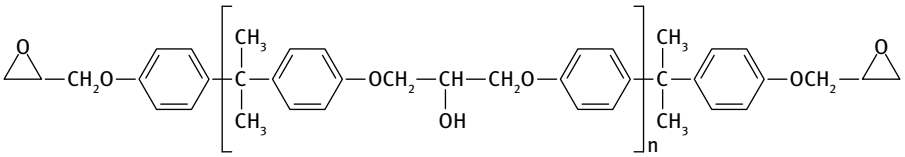

Fig. 1.3: Di-functional epoxy resin.

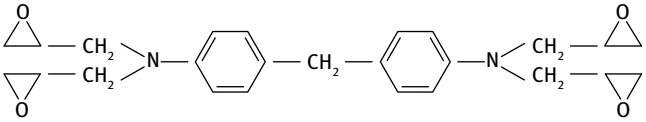

Fig. 1.4: Tetraglycidyl Methylene Dianiline (TGMDA).

1.2.2 Epoxy resin in sample preparation

Commercially modified Epilox resin (T 19-36/700, LEUNA-Harze GmbH, Germany) was used for this study. It is a colorless, low viscosity (650–750 mPa/s at 25 °C) epoxy resin with a reduced crystallization tendency and a density of 1.14 g · cm^{-3}. Its chemical composition is Bisphenol-A epichloro hydrine (50–100 wt.%) and oxirane, mono-{(C12-14-alkyloxy) methyl derivatives (10–25 wt.%). To complete the polymerization reaction, a cross linker was used.

Epilox cross linker (H10-31, LEUNA-Harze GmbH, Germany) is a liquid, colorless, low viscosity (400–600 mPa s) modified cycloaliphatic polyamine epoxide adduct with a density of 1 g · cm^{-3} and containing 3-aminomethyl-3,5,5-trimethylcyclohexyl (25–50 wt.%), benzyl alcohol (25–50 wt.%), and nonyl phenol (<5 wt.%). 3-aminomethyl-3,5,5-tri-methylcyclohexyl was in a clear liquid with a density (0.24 g/ml at 200 °C).

1.2.3 Multi walled carbon nanotubes (MWCNTs)

MWCNTs can be synthesized by various processes. The three most widely used methods are visible light vaporization, arc discharge, and catalytic chemical vapor deposition (often abbreviated to chemical vapor deposition (CVD)).

The visible-light method can be further classified into three separate methods of synthesis namely: (i) laser ablation, in which a pulsed laser is used to carry out the synthesis of carbon nano tubes, (ii) a continuous laser is used for synthesis in laser vaporization method, while in (iii) the solar vaporization method a continuous multiwavelength light from a solar furnace source is used to carry out the process. Other methods used to synthesize CNTs are flame synthesis, liquid hydrocarbon synthesis,

and catalytic plastic pyrolysis. These methods are not used for bulk production, so they are of less significance compared to the widely-used CVD method.

CVD is a thermal reaction in which a gaseous hydrocarbon is cracked into carbon and other constituents in the presence of a catalyst. The catalyst is usually a transition metal such as cobalt, iron, or nickel. The MWCNT growth reaction is aided by a catalyst. In-house MWCNT growth was performed by using iron as a catalyst along with camphor (Sigma Aldrich 99 % purity) and waste polyethylene granules as a carbon source. The system was set to adopt the floating catalyst method. In the floating catalyst method, the metal particles are transferred by an inert gas carrier (argon/helium) to a nonreactive silicon dioxide surface. The temperature of the reactor is adjusted in a way that allows the cracking of the carbon source but not the pyrolysis of the carbon-containing species. For a given combination of the catalyst and gas mixture that is effective in producing carbon nanotubes, MWCNTs formation is favored for the formation of SWCNTs at a lower temperature range of 700~800 °C and at a high temperature range of 850~950 °C. The main advantage of this system is that it can easily be scaled to commercial scale CNT production [7, 11, 12, 15]. This method was adopted to synthesize MWCNTs (FCCF340 and P3) in house (carbon group, Politecnico di Torino). Commercial functionalized and graphitized MWCNTs were purchased from Cheaptubes, USA, and normal MWCNTs (MW7) were provided by Nanothinx, Greece. The detailed specifications of MWCNTs are listed in Table 1.2.

Tab. 1.2: MWCNTs characterisation.

Code	Type	Diameter nm	Length µm	Purity weight %
MW7	MWCNTs	25~45	>10	98.5
MWF3	-COOH functionalized	<8	10~30	95
MWG2	Thin craphitized	8~15	10~50	99
FCCF340	In-house made from camphor	50	179	85

1.2.4 MWCNT Nanofiller epoxy composite preparation

Dispersion of the nano scale filler in the polymer matrix plays a key role in determining composites properties. Nano scale fillers exhibit a surface area of several orders of magnitude larger than the surface area possessed by microscale particles. The surface area of CNTs behaves as an interface to transfer the stress from polymer matrix to the individual nanotube and dissipate the effect of the load applied. But in nanoscale particles secondary forces are prevalent, and for this reason CNTs have a strong tendency to form agglomerates. Exploitation of the remarkable properties of CNTs in polymers is therefore dependant on their homogeneous dispersion in the polymer matrix, good breaking up of the carbon nanotube agglomerates, and adequate wetting of CNTs with polymer. Parameters that affect the quality of dispersion are length, purity, sur-

face modification such as functionalization, graphitisation such as the degree of entanglement, polymer viscosity [15, 20, 23, 29]. This is why we choose different kinds of MWCNTs to study the mechanical behavior in epoxy polymer. Good dispersion of MWCNTs in polymer matrix can be achieved by either mechanical or chemical means. In the first case MWCNTs can be dispersed into low-viscosity liquids (either polymer or cross linker) by using mechanical shear mixing before polymerisation starts.

1.2.5 Preparation of epilox CNT nanocomposites

Epoxy resin (LEUNA-Harze GmbH, T 19-36/700) (63 wt.%), cross linker (LEUNA-Harze GmbH, H 10–31) (37 wt.%) and filler CNTs (1 and 3 wt.%) (as shown in Table 1.3) were thoroughly mixed with mechanical stirring (20,000 RPM for 2 min). High-speed mechanical mixing initiates the exothermic polymerisation between the resin and cross linker, resulting in evolving entrapped gas bubbles in the composites. Sonication (ultrasonic frequency 37 kHz for 15 min) followed by degassing in the vacuum (50 mbar for 30 min) steps have been subsequently undertaken in order to get rid of these entrapped gas bubbles before the composite completes its polymerisation reaction. Before the onset of polymerization, the composite mixtures were moulded into dog-bone shapes (ASTM D 638 standard) as shown in Fig. 1.5. Handling strength of these composite occurred in 24 h (with temperature >25 °C), and complete curing was achieved after 5–7 days at 25 °C. To cure the moulds faster, however, they were kept in the oven at 70 °C for 4 h. As mentioned earlier the composites were prepared with 1 and 3 wt.% of MWCNT filler concentrations. Before beginning analysis, the thickness, width, and length of the composite samples were measured. These dimensions were approximately (±0.1 mm) the same for each sample. Defective samples (with uneven surfaces and surface-entrapped air bubbles) were not considered for further analysis.

Tab. 1.3: Epoxy and epoxy composite component quantity required (in grams).

Epoxy composite	*Epoxy resin*	*Cross linker*	*Filler*
	(g)		
Blank	63	37	–
1 % Filler	62.37	36.63	1.0
3 % Filler	61.11	35.89	3.0

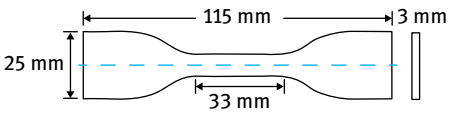

Fig. 1.5: Schematic diagram of dog-bone shaped composite samples for mechanical analysis.

1.3 Mechanical analysis

For mechanical testing we used a Q-test 10 tensile tester by MTS, a very flexible machine. It can be used to investigate the mechanical properties of materials ranging from plastics to composite materials to metals. It is equipped with multiple jaws to hold the material specimens. The machine can be provided with several load cells, ranging from 50 N to 10 kN. In the reported tests the machine was equipped with a 10 kN load cell. The machine is also equipped with an extensometer and automatic control systems. The distance between the jaws can be adjusted manually. The machine operates on the working principle of a constant rate of traverse ranging from 0.025 mm/min to 1 m/min. One jaw is fixed at the bottom while the top jaw pulls the specimen upwards it and measures the reaction force by means of the load cell. The specimen is stretched at a uniform deformation velocity until it breaks. The load and elongation graphs are displayed on the computer screen attached to the machine, and these data are exported to an ASCII file for subsequent analysis. The whole arrangement is shown in Fig. 1.6.

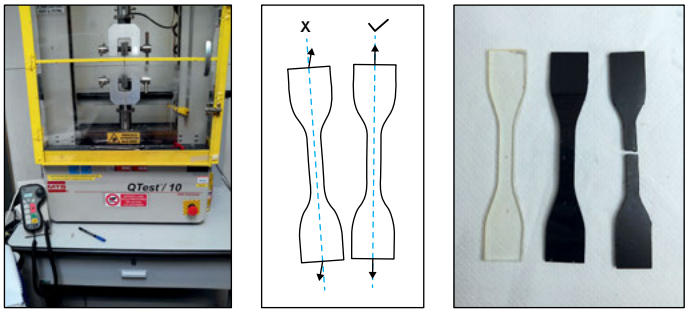

Fig. 1.6: (a) Q-test 10 analysis instrument; (b) proper sample fixing; (c) actual sample for analysis.

The traverse speed is set before testing the specimen. The value was set at 0.5 mm/min traverse speed. The software requires the dimensions of the test specimen to be according the ASTM D-638 standard. The dimensions provided for analysis were the length, measuring length, thickness, and width of the specimen. Mechanical data (tensile load F vs. displacement d) obtained from instrumental software was further elaborated to determine elongation, stress, strain, Young's modulus, and fracture toughness values.

As a first step the load and displacement values were converted to stress (MPa) and strain (adimensional), respectively. The average stress σ is defined as "the ratio of the tensile load applied to the area of the original cross section"[35]:

$$\sigma = \frac{F}{S_{initial}}. \tag{1.1}$$

Strain is a dimensionless quantity that describes the ratio of change in length (d) to the original length of composite [35]

$$\varepsilon = \frac{d}{L_{initial}}. \tag{1.2}$$

Stress vs. strain plots are the most common way of reporting data. A typical data plot (see Fig. 1.7) can be divided in three regions:

(1) *elastic region*: the linear (or quasi-linear) reversible part at low strain; removing the stress will bring back the specimen to the initial geometry;
(2) *plastic region*: departure from linearity occurs and irreversible elongation enters into play; a permanent elongation remains even if the stress is removed;
(3) *fracture region*: the final part of the plot leading to specimen failure through fracture.

In order to classify the materials and to better describe their behavior, several quantities are commonly defined and reported. The relevant quantities (see Fig. 1.7) are as follows:

(1) *Young's modulus (E)*: its value corresponds to the slope of the fitting line of the elastic region and gives information on the elasticity and rigidity of the material
(2) *Yield point*: around this point a transition from elastic to plastic behavior occurs. The yield point is conventionally defined as the point of intersection between the material curve and a line parallel to the elastic one having an offset strain of 0.2 %. The coordinates of the yield point give the information about *yield stress* (σ_Y) and *yield strain* (ε_Y). Higher values σ_Y and ε_Y mean a higher load-bearing capability in the elastic region. These two quantities directly affect the capability of the material to absorbing energy in the elastic region
(3) *Modulus of resilience* (u_o). Resilience describes the ability of the material to absorb energy while being deformed elastically, and return the supplied energy on unloading. It corresponds to the maximum value of the elastic energy density that the material can withstand before the onset of plastic deformation. The parameter u_o can be calculated evaluating the area under the stress-strain curve from the origin to the yield point, approximately equal to

$$u_o = \frac{1}{2}\sigma_Y \epsilon_Y = \frac{1}{2}\frac{\sigma_y^2}{E} \tag{1.3}$$

(4) *Ultimate strength point*: this is the point with the maximum stress value on the stress-strain curve. A further increase of strain leads to relevant shrinking of the specimen section ultimately leading to fracture
(5) *Ultimate tensile strength* (UTS, also known as "tensile strength"): this is the stress value that corresponds to the ultimate strength point. Its value in a composite is affected by preparation method, defects in the material, and temperature of the material and the environment

(6) *Fracture point*: this is the last point recorded for the stress-strain curve before specimen failure. Strain at fracture point (also: strain at break) defines the ability of a material to elongate under tensile loads. It also expresses the capability of a material to resist changes of shape without crack formation.

(7) *Fracture toughness* (K, also known as "toughness"): this is the amount of energy density the material can absorb before fracture occurs. Hence it describes the ability of a material to absorb energy and deform plastically without fracturing. Its value is the area under the stress-strain curve from the origin to the fracture point displacement ε_f

$$K = \int_0^{\varepsilon_f} \sigma \, d\epsilon. \tag{1.4}$$

A dedicated software has been developed in-house that automatically identifies all the relevant points and calculates the relevant quantities of the stress-strain curve.

The two extreme behaviors of materials are ductile (Fig. 1.7) and brittle (Fig. 1.8). In the first case, after the ultimate strength point there is a wide plastic region. In the second case, the failure occurs just after the end of the elastic region (i.e. the fracture point is very close to the yield point and corresponds also to the ultimate strength point). Plastic region is almost absent.

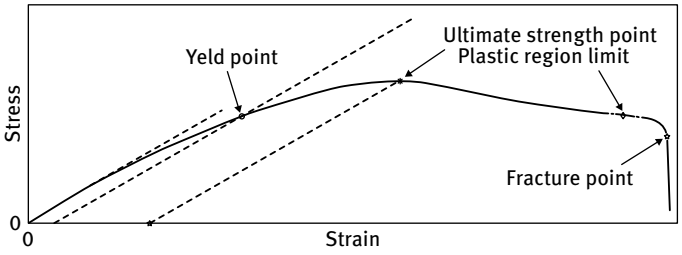

Fig. 1.7: Ductile behavior.

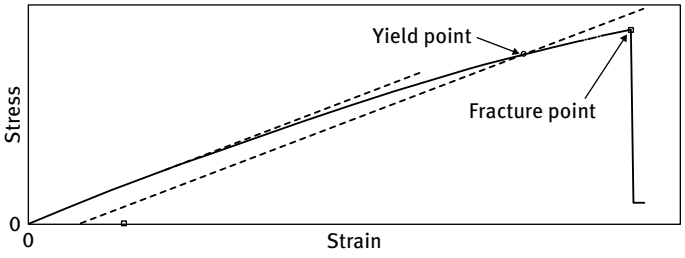

Fig. 1.8: Brittle behavior.

1.4 FESEM details with sample preparation

A ZEISS SUPRA™ 40 field emission scanning electron microscope (FESEM) was used to deliver high quality and high resolution images of nanoscale materials to meet the demands and challenges involved in the study of application of nanoscale materials. The mechanically fractured composite part was chosen for analysis. Generally the specimens to be analysed are prepared by cryofracturing them in liquid nitrogen. In this study, we prefer to cut the samples close to a mechanically broken part. Care was taken to keep the mechanically modified surface untouched and undamaged in sample preparation. The samples were mounted on aluminum studs in order to be able to observe them from a top view. A chromium coating of 5–7 nm thickness was deposited by electron sputtering to avoid the charging effect.

FESEM analysis of epoxy polymer shows the slipping of the polymeric chain during the application of the tensile force which causes the composite to break. The epoxy fractured surface (Fig. 1.9) is more uniform and defect free, which is ideally a benchmark condition for mechanical property of polymeric sample.

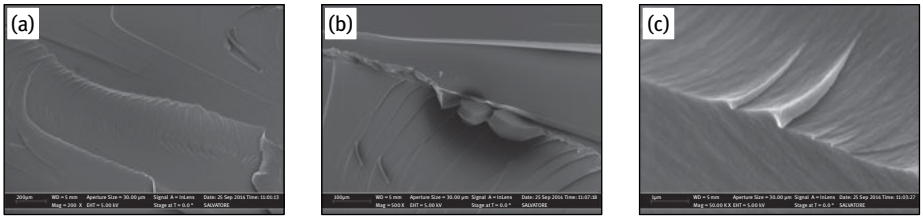

Fig. 1.9: FESEM analysis of the epoxy resin specimens.

1.5 Results and discussion

All the produced specimens were tested, and the data were collected and analyzed. In the following the different behaviors of the specimens are highlighted, the presence of MWCNTs, is shown in the FESEM images of the fracture region for each specimen type, and conclusions are drawn.

The first analyzed group of specimens is the MW7. In Fig. 1.10 the tensile behavior of this group is compared with the blank epoxy. In Fig. 1.11 the FESEM analysis is represented for showing the presence of MWCNTs. This approach is used also for the other group of specimens.

Composites prepared with MW7 show the presence of microbubbles. They create a weak point for fracture, leading to a premature failure of the composite during the course of the application of stress. The microbubble size is larger in 3 % MW7 sample, with a consequent reduction of the plastic region. Moreover, MW7 CNTs have a tendency to form big chunks due to Van der Waal's forces (MW7 and also MWG2-1).

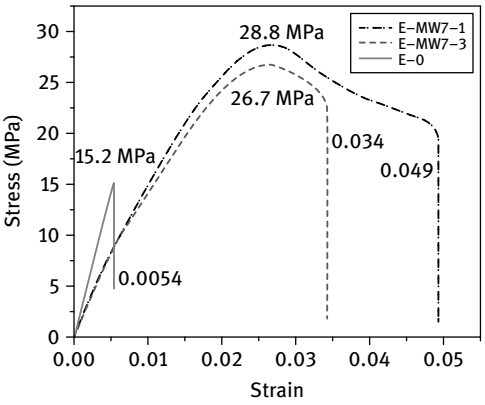

Fig. 1.10: Tensile behavior of MW7.

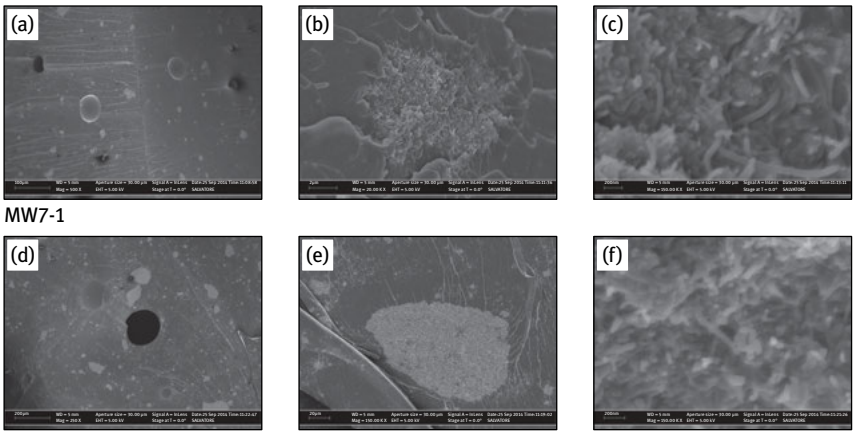

Fig. 1.11: FESEM of MW7 specimens: CNTs are clearly visible in the rightmost column.

The agglomerations have a great impact on localizing the mechanical forces to create a fracture point during the course of elongation by a tensile force. Chunks also reduce the ability to stop the slippage of the polymer chains one over another. We speculate that the two phenomena can be related, with big chunks leading to bubble formation during the preparation procedure (the reasons for this still need to be investigated). On the basis of Fig. 1.10, it is possible to conclude that the MW7 group presents an increment of the UTS and a reduction of the Young's modulus with respect to the blank epoxy. In addition, a change of the behavior from brittle to ductile can be underlined.

The same analysis is made for the MWF3 specimen group (Figs. 1.12 and 1.13). The two percentages of CNTs lead to remarkably different behavior. The MWF3-3 specimen

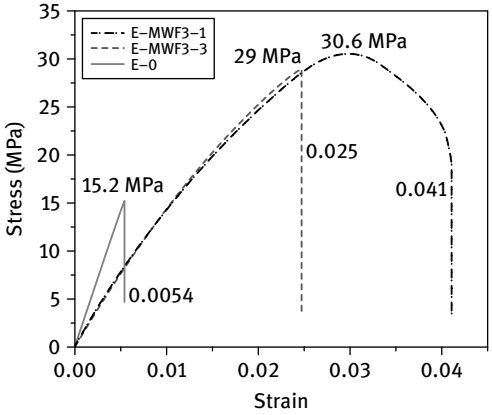

Fig. 1.12: Tensile behavior of MWF3.

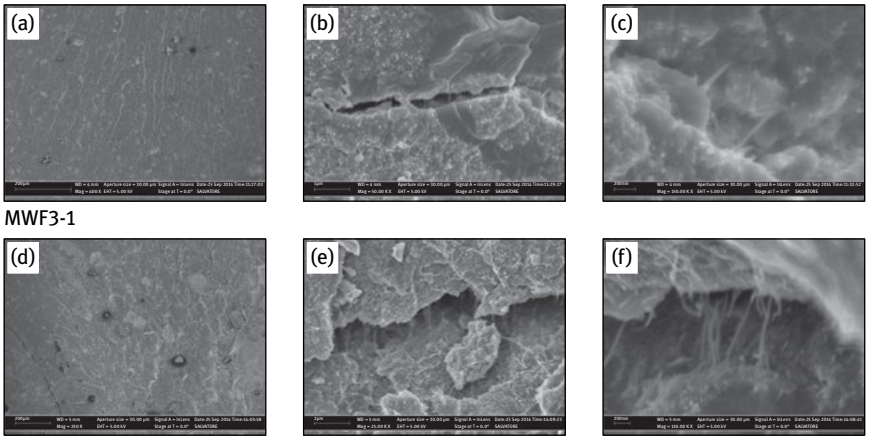

Fig. 1.13: FESEM of MWF3 specimens: CNTs are clearly visible in the rightmost column.

presents a brittle behavior, while the MWF3-1 has a more plastic one. The analysis of FESEM images suggest that the reason for that behavior may be related to the presence of chunks. On the other hand the values of the yield stress and Young's modulus of the two specimens are similar, suggesting that the main effect on the elastic region is saturating at low CNT contents.

By considering the curves of the third group (MWG2 specimens, Figs. 1.15 and 1.16), we observe that the introduction of MWCNTs in the epoxy matrix changes the behavior of the material from brittle to ductile, increases the UTS, and decreases the Young's modulus, as depicted for the previous groups. In this case the higher values of UTS and toughness are reached at a lower filler percentage, but the material with higher

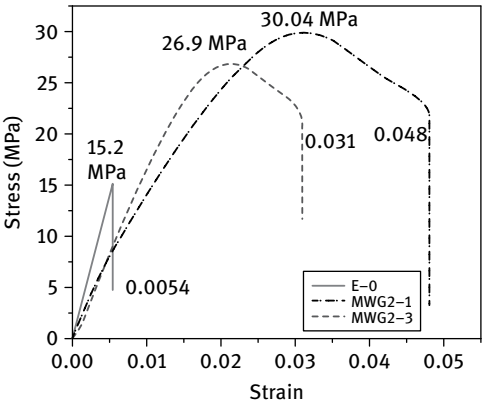

Fig. 1.14: Tensile behavior of MWG2.

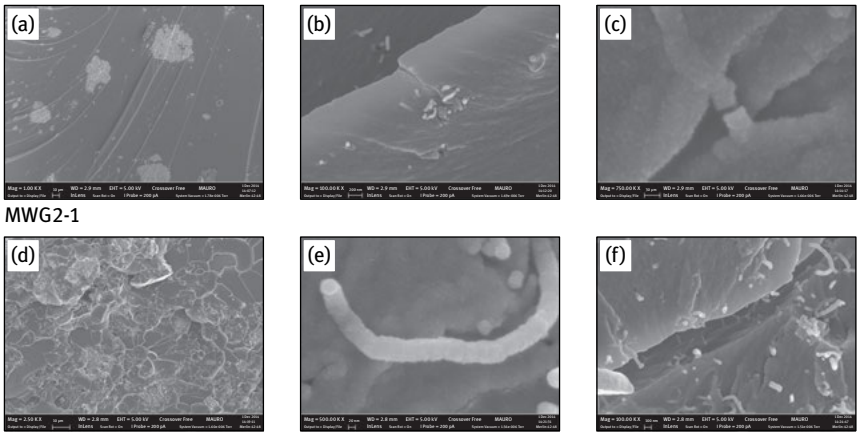

Fig. 1.15: FESEM of MWG2 specimens: CNTs are clearly visible in the rightmost column.

percentage of filler presents a higher Young's modulus and a lower UTS and toughness with respect to the other filler percentage.

The FCCF340 group presents a perfect ductile behavior and no great difference in terms of toughness. A little increase of UTS and Young's modulus is presented by the specimen with more filler (3 %) (see Figs. 1.16 and 1.17).

Good and evenly distributed filler (made and functionalized in-house) MWCNTs add to the strength of the polymers and enhance the load-carrying capacity. In this case it seems that there is a good interaction between the filler and the polymer matrix. There is significant interfacial bonding between the filler and the matrix. The stress is transferred from the matrix to the filler particles, and the particles help transfer this stress to single fibres, thus adding to the strength of the composite. A functionalized

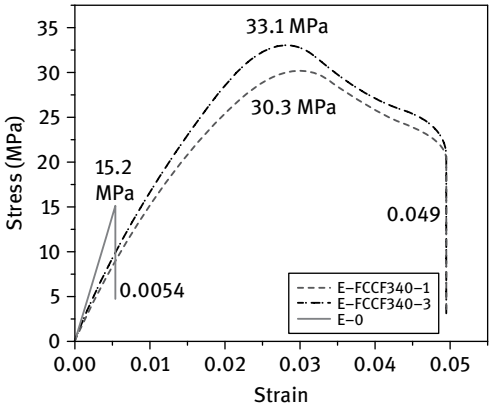

Fig. 1.16: Tensile behavior of FCCF340.

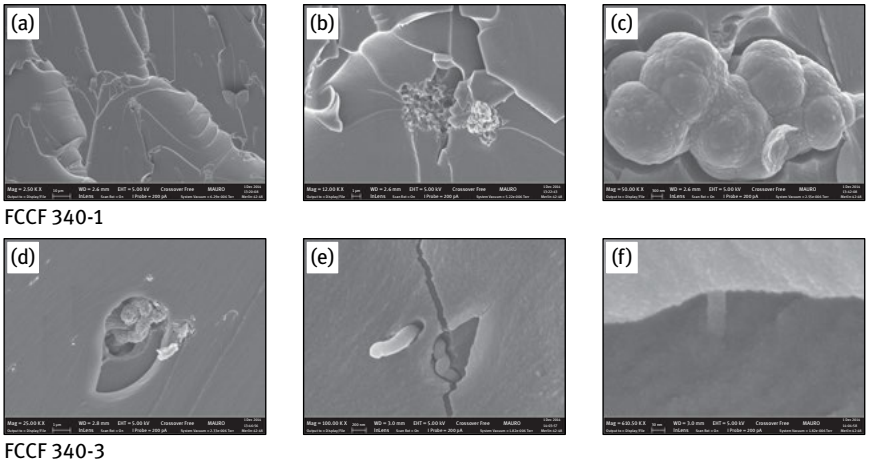

Fig. 1.17: FESEM of FCCF340 specimens: CNTs are clearly visible in the rightmost column.

MWCNTs (MWF3) family has better tensile properties due to the better interaction between the filler and the matrix, thus preventing these layers from slipping over each other during the application of the tensile force. Whereas in-house made MWCNTs (FCCF340) have a high aspect ratio, with some round shape carbon growth which allows for better interaction with epoxy resin result in getting better or comparable mechanical property than other MWCNT families tried in this study.

By comparing all the extracted data, some additional considerations can be taken.

1.6 Ultimate tensile stress (UTS)

The comparative study of UTS (Fig. 1.18) shows that MWCNTs of all kinds enhance the UTS from 15.2 MPa (epoxy polymer) to 26–33 MPa. The maximum UTS was observed for in-house made MWCNTs (FCCF340) with 3 wt.%. So in terms of UTS it is possible to conclude that the MWCNTs, independent of their type and percentage, can nearly double the UTS of the matrix material.

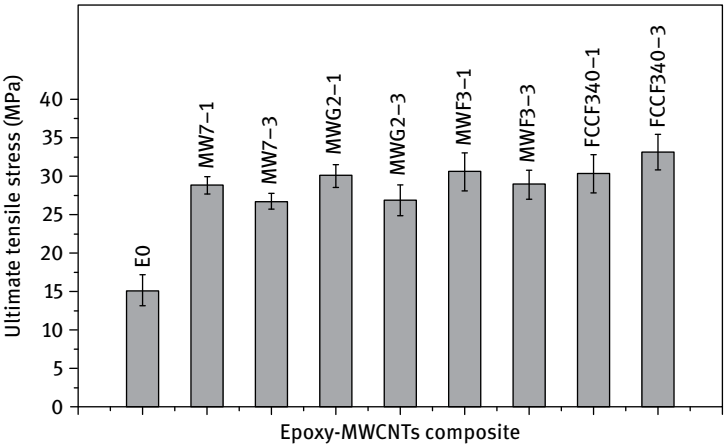

Fig. 1.18: Ultimate tensile strength comparisons.

1.6.1 Strain at break

Almost 10 time better elongation under stress is observed (Fig. 1.19) in comparison with epoxy polymer and composite with in-house made CNTs FCCF-340 (1 and 3 wt.%), Normal MW7 (1 wt.%) and graphitized MWG2 (1 wt.%) nanofillers. This means that the filler increases the plastic region of the matrix material, increasing the capability of the material to withstand a crack without failing.

1.6.2 Yield point

The ductile material, as the composite material that experiences a plastic zone in the stress-strain chart, is usually preferred for the design of mechanical and structural component, because a "reservoir" of strength is guaranteed by the plastic region. In fact, the ultimate tensile strength (UTS) is usually higher than the yield limit, so fixing the yield limit as the failure threshold, before having the complete failure of the structure there is an additional increment of force. The design criteria are based on the yield limit, so this value indicates the capability of the material to last. As an example,

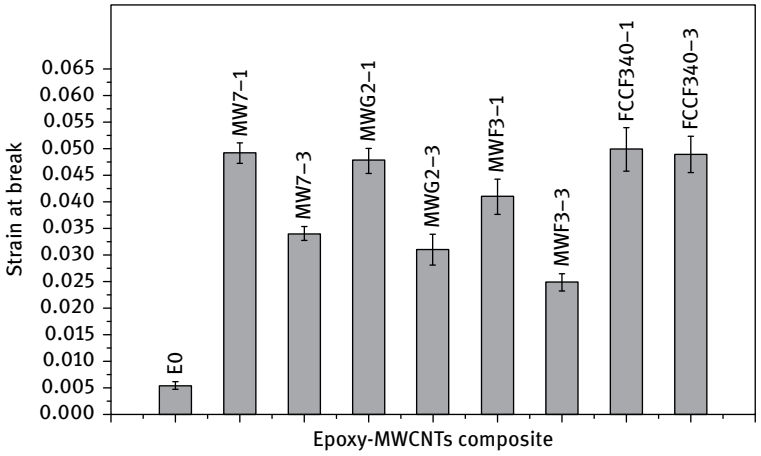

Fig. 1.19: Strain at break comparison.

consider a shaft for transmitting a torque. If the shaft is made in pure epoxy without filler, the nominal transmitted torque can be considered as reference and set to 1 Nm. If the same shaft is made of epoxy filled with MWCNT, the transmitted torque increases to at least 2.4 Nm (MW7-3). This means that the same shaft with the same weight can transmit more than double the reference torque.

By analyzing Fig. 1.20, it is possible to highlight that the presence of the filler almost always more than doubles the yield stress. A small variation with respect to the filler percentage can be seen. In fact, for MW7, MWG2, and MWF3 a 1 % filler amount leads to higher values of yield stress with respect to the 3 % case. The trend is inverted for FCCF340, as it occurs for traditional fillers in plastic material.

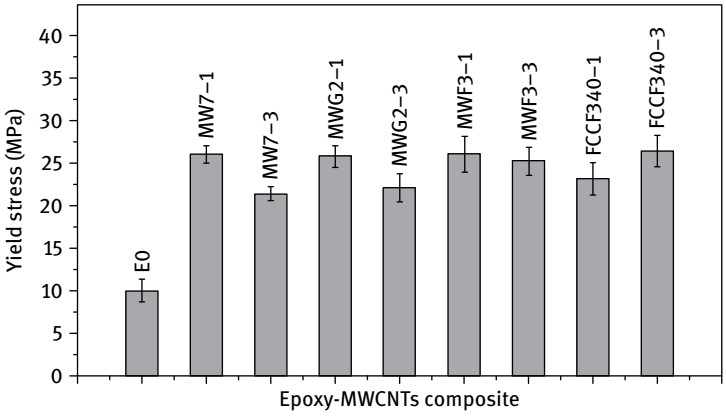

Fig. 1.20: Yield stress comparison.

1.6.3 Resilience

The highest value of resilience was shown by the MWF3 group with 1wt.% CNT addition (Fig. 1.21). Multiwall graphitized MWCNTs (MWG2-1) in 1 wt.% showed the second best results, as depicted in the graph. The resilience could be considered as an indicator of the elastic capability of the material. Let us consider the same shaft as above. The higher the resilience of the material, the higher is the elastic energy accumulated during the loading process, so that a higher resilience material allows us to design a shaft that, with the same external load, deforms less, or, with the same size of the shaft, can accumulate more energy. This means that the presence of MWCNTs inside the epoxy resin increases the possibility of accumulating elastic energy in the material.

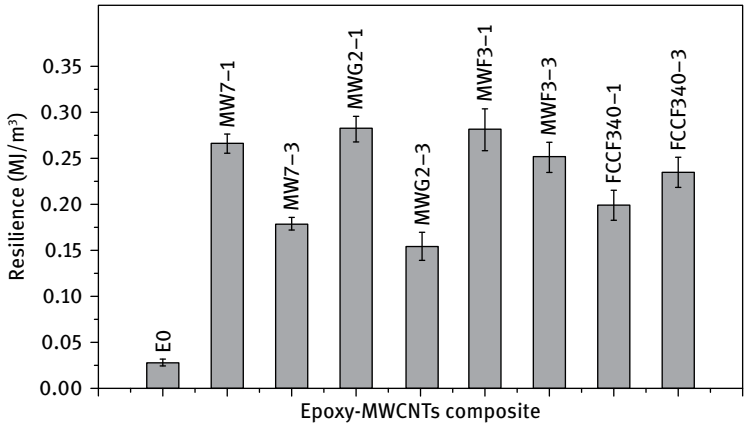

Fig. 1.21: Resilience comparison.

1.6.4 Toughness

Higher toughness indicates that a higher energy per unit volume can be absorbed in the plastic region before breaking. The best results were shown by the in-house generated MWCNTs (FCCF340-3) in 3 % by weight of the composite. Multiwall graphitized CNTs showed the second-best results. An impact test is required for obtaining fully reliable information about the fracture behavior, but the higher the toughness, the higher is the capability of the material to guarantee safety of the design, because a great plastic energy amount is present. On the basis of Fig. 1.22 and Figs. 1.10, 1.12, 1.14, and 1.16 we can clearly see evidence of the brittle or ductile behavior of the different materials. Referring to Figs. 1.10, 1.12, 1.14, and 1.16, the base epoxy and MWF3-3 do not show a relevant plastic region, so they can be considered as brittle (in fact they have lower values of toughness). On the basis of the chart in Fig. 1.22 a threshold for transition between brittle and ductile behavior could be set at 0.5 MJ/m^3. If the mate-

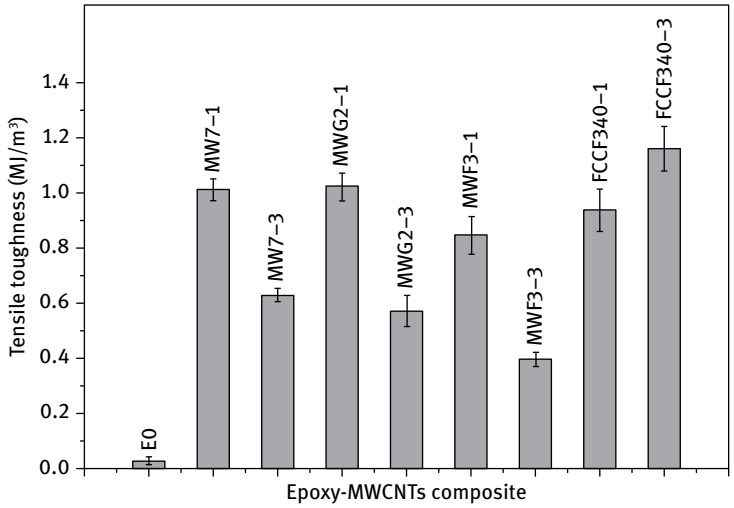

Fig. 1.22: Tensile toughness comparisons.

rial has toughness lower than this value, it can be considered as brittle; otherwise it presents an important plastic behavior.

1.6.5 Young's modulus

The highest value of Young's modulus (1850 MPa) was obtained (Fig. 1.23) by the composite prepared by graphitized MWCNTs (MWG2-3) with 3 wt.% of filler, but it is still approximately 1000 MPa less than the epoxy resin. The second-best results were shown by in-house generated MWCNTs (FCCF340-3) with 3 % by weight of filler. The value for Young's modulus was 1700 MPa.

Overall mechanical results show that in most of the analysis in-house made MWCNTs (FCCF340) show better or comparable results as compared to commercial MWCNT nanofillers. It is possible to underline that the presence of the filler decreases in the same manner as the Young's modulus, more or less halving it.

1.7 Conclusions

As highlighted in the previous discussion, the presence of MWCNTs inside epoxy resin changes its behavior from brittle to ductile and increases the UTS and the yield stress, but it decreases the Young's modulus. The mechanism that justifies this variation is probably related to the MWCNTs capability to block the crack propagation and support the sliding of the polymeric chain. So the stress for breaking the material is increased,

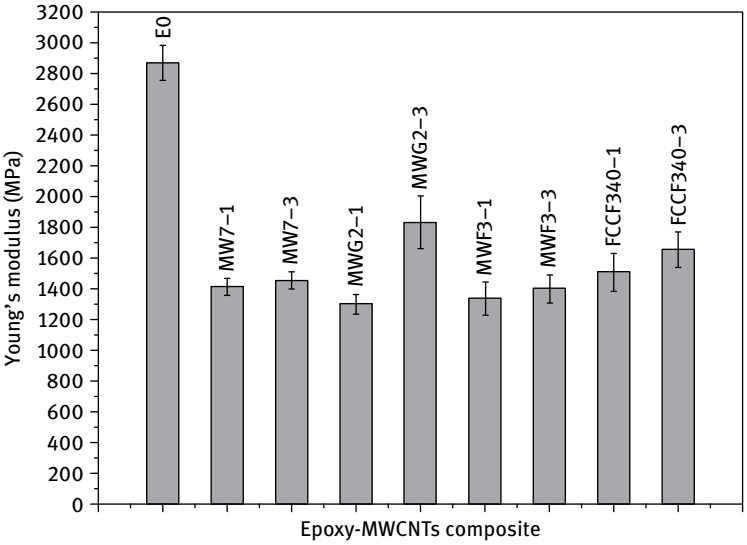

Fig. 1.23: Young's modulus comparison.

the plastic deformation is favored, but at the same time the polymeric chain tends to slide instead of react, so the Young's modulus lowers.

MWCNTs with different surface modification with higher aspect ratios (length to diameter ratio) showed improvement in the tensile properties. Better MWCNT dispersion (less agglomeration) and less or no defect may better achieve improved mechanical strength. In-house made MWCNTs with cheaper sources have better or comparable mechanical properties, like commercial MWCNTs in composites. The nanostructural dimensions have a great impact on dispersion in the matrix, which will continue to impact on the mechanical property of the composite.

This work suggests that the presence of small quantities of MWCNT could drastically change the behavior of the epoxy resin and open the way for a series of new possible applications of this material.

1.8 Future trends

- The rheological behavior of carbon nanotubes reinforced polymer composites has not been studied thoroughly until now. Investigation in this area will aid in the further improvement of the properties of the polymer composite.
- CNTs can be used to substitute carbon fibers and carbon black in many applications.
- There is much room for work in the areas of CNT-polymer composites prepared by coagulation, solution processing, and in-situ polymerization.

- Comparison should be done with other mechanical dispersion techniques such as calendaring and sonication in order to find the best possible way to have a good even dispersion of the carbon nanotubes in the polymer matrix.
- Cheaper and higher production of CNTs is needed to further increase the market share in the composites sector.

Acknowledgement

We thank Dr. Salvatore Guastella (Polytechnic of Turin, Italy) for valuable discussion, Nanothinx for providing their CNTs, and LEUNA-Harze GmbH, Germany for epoxy resin. We also thank the Higher Education Commission (HEC) of Pakistan for their financial support for Mr. Aamer during the course of his research work.

References

[1] Paradise M, Goswami T. 2007. Carbon nanotubes – Production and industrial applications, *Mater. Des.* **28**(5), 1477–1489.
[2] Kroto HW, Heath JR, O'Brien SC, Curl RF, Smalley RE. 1985. C60: Buckminsterfullerene, *Nature* **318**(6042), 162–163.
[3] Harris PJF. 2004. Fullerene-related structure of commercial glassy carbons, *Philos. Mag.* **84**(29), 3159–3167.
[4] Iijima S. 1980. Direct observation of the tetrahedral bonding in graphitized carbon black by high resolution electron microscopy, *J. Cryst. Growth* **50**(3), 675–683.
[5] Reibold M, Paufler P, Levin AA, Kochmann W, Pätzke N, Meyer DC. 2006. Materials: carbon nanotubes in an ancient Damascus sabre, *Nature* **444**(7117), 286.
[6] Radushkevich LV, Luk'yanovich VM. 1952. The structure of carbon forming in thermal decomposition of carbon monoxide on an iron catalyst, *Sov. J. Chem. Phys.* **26**, 88–95.
[7] Mcnally T, Pötschke P. 2011. *Polymer-Carbon Nanotube Composites*, Series in. Cambridge, UK, Woodhead Publishing Limited.
[8] Iijima S. 1991. Helical microtubules of graphitic carbon, *Nature* **354** 56–58.
[9] Burstein E. 2003. A major milestone in nanoscale material science: the 2002 Benjamin Franklin Medal in Physics presented to Sumio Iijima, *J. Franklin Inst.* **340**(3–4), 221–242.
[10] Yamabe T. 1995. Recent development of carbon nanotube, *Synth. Met.* **70**(1–3), 1511–1518.
[11] Grady BP. 2011. *Carbon Nanotube-Polymer Composites: Manufacture, Properties, and Applications*, Unabridged, New Jersey, Johne Wiley & Sons Inc.
[12] Dai H. 2002. Carbon Nanotubes: Synthesis, Integration, and Properties, *Acc. Chem. Res.* **35**(12), 1035–1044.
[13] Kalamkarov AL, Georgiades AV, Rokkam SK, Veedu VP, Ghasemi-Nejhad MN. 2006. Analytical and numerical techniques to predict carbon nanotubes properties, *Int. J. Solids Struct.* **43**(22–23), 6832–6854.
[14] Cao G, Chen X. 2007. The effects of chirality and boundary conditions on the mechanical properties of single-walled carbon nanotubes, *Int. J. Solids Struct.* **44**(17), 5447–5465.
[15] Shaffer MSP, Sander JKW. 2006. Carbon nanotube/nanofibre polymer composites, in S.G. Advani (ed.), *Processing and Properties of nano composites*, World Scientific Publishing Co. pvt. Ltd., 1–59.

[16] Song K, Zhang Y, Meng J, Green E, Tajaddod N, Li H, Minus M. 2013. Structural Polymer-Based Carbon Nanotube Composite Fibers: Understanding the Processing–Structure–Performance Relationship, *Materials (Basel)*. **6**(6), 2543–2577.
[17] Bokobza L. 2007. Multiwall carbon nanotube elastomeric composites: A review, *Polymer (Guildf)*. **48**(17), 4907–4920.
[18] Fiedler B, Gojny FH, Wichmann MHG, Nolte MCM, Schulte K. 2006. Fundamental aspects of nano-reinforced composites, *Compos. Sci. Technol.* **66**(16), 3115–3125.
[19] Her S-C, Lai C-Y. 2013. Dynamic Behavior of Nanocomposites Reinforced with Multi-Walled Carbon Nanotubes (MWCNTs), *Materials (Basel)*. **6**(6), 2274–2284.
[20] Du F, Fischer JE, Winey KI. 2003. Coagulation method for preparing single-walled carbon nanotube/poly(methyl methacrylate) composites and their modulus, electrical conductivity, and thermal stability, *J. Polym. Sci. Part B Polym. Phys.* **41**(24), 3333–3338.
[21] Ash BJ, Siegel RW, Schadler LS. 2004. Glass-transition temperature behavior of alumina/PMMA nanocomposites, *J. Polym. Sci. Part B Polym. Phys.* **42**(23), 4371–4383.
[22] Ash LSSBJ, Eitan A. 2004. Polymer nanocomposites with particle and carbon nanotube fillers, in KPA Schwarz, CI. Contescu (eds.), *Dekker Encyclopedia of Nanoscience and Nanotechnology*, 1st ed., New York, Marcel Dekker, 2917–2930.
[23] Coleman JN, Khan U, Blau WJ, Gun'ko YK. 2006. Small but strong: A review of the mechanical properties of carbon nanotube–polymer composites, *Carbon N. Y.* **44**(9), 1624–1652.
[24] Ramana VG, Balaji P, Kumar N, Jain P. 2010. Mechanical properties of multi-walled carbon nanotube reinforced polymer composites, *Indian J. Eng. Mater. Sci.* **17**(210), 331–337.
[25] Park C, Wilkinson J, Banda S, Ounaies Z, Wise KE, Sauti G, Lillehei PT, Harrison JS. 2006. Aligned single-wall carbon nanotube polymer composites using an electric field, *J. Polym. Sci. Part B Polym. Phys.* **44**(12), 1751–1762.
[26] Hashim A (Ed.). 2011. *Advances in Nanocomposite Technology*. InTech.
[27] Reddy B (Ed.). 2011. *Advances in Nanocomposites – Synthesis, Characterization and Industrial Applications*, InTech.
[28] Wenjie Wang NSM. 2007. Characterization of NanotubeReinforced Polymer Composites, in DS Yellampalli (ed.), *Carbon Nanotubes – Polymer Nanocomposites*, 1st ed., Croatia: InTech, 155–172.
[29] Bal S. Samal SS. 2007. Carbon nanotube reinforced polymer composites – A state of the art, *Bull. Mater. Sci.* **30**(4) 379–386.
[30] Zanello LP, Zhao B, Hu H, Haddon RC. 2006. Bone cell proliferation on carbon nanotubes, *Nano Lett.*, **6**(3), 562–567.
[31] Xanthos M (Ed.). 2010. *Functional Fillers for Plastics*, 2nd ed. John Wiley & Sons Inc, 531.
[32] Akovali G (Ed.). 2001. *Handbook of composite fabrication*, Illustrate. iSmithers Rapra Publishing, 196.
[33] Andrews R, Weisenberger M. 2004. Carbon nanotube polymer composites, *Curr. Opin. Solid State Mater. Sci.* **8**(1), 31–37.
[34] May C (Ed.). 1987. *Epoxy Resins: Chemistry and Technology*, 2nd ed. CRC Press, 1288.
[35] Davis JR. 2004. *Tensile Testing*, 2nd ed. ASM International, 279.

D.I. Pantelis, P.N. Karakizis, D.A. Dragatogiannis,
and C.A. Charitidis

2 Dissimilar friction stir welding of aluminum alloys reinforced with carbon nanotubes

Abstract: This chapter is devoted to studying the possibility of incorporating carbon nanotubes (CNTs) as reinforcing fillers in dissimilar metal matrices joints produced by friction stir welding (FSW), as well as the impact of this incorporation on the microstructural and mechanical properties of these joints. Carbon nanotubes are extensively used as a reinforcing material in nanocomposites, due to their high stiffness and strength. FSW is a solid-state welding process of joining aluminum and other metallic alloys and has been employed in the aerospace, rail, automotive, and marine industries. Recently, friction stir processing (FSP), a derivative method of FSW, has been employed as an alternative for the production of metal matrix composites (MMCs). In this work, the process parameters were optimized in order to achieve nondefective welds, with and without the addition of CNTs. Two main cases were studied: (1) FSP was optimized by changing the tool rotational and travel speed as well as the number and direction of FSW passes, and (2) a Taguchi design scheme was adopted to further investigate the FSP in relevance to three factors (number, direction of passes, and tool rotational speed). Mechanical behavior was studied, and the local mechanical properties of the produced MMCs were compared with their bulk counterparts and parent materials. More specifically, the measured mechanical properties in the micro- and nanoscale (namely hardness and elastic modulus) are correlated with the microstructure and the presence of fillers.

2.1 Introduction

Aluminum alloys play a major role in today's manufacturing processes due to their properties, such as good corrosion and wear resistance as well as their high strength-to-weight ratio. Nevertheless, aluminum alloys tend to show low weldability while using conventional welding methods, and as a result severe adhesive wear may be observed. This drawback can be overcome by the incorporation of ceramic particles into the metal matrix. Most of the methods for producing metal matrix composites (MMCs) reported in literature, [1–4] require the melting of the metal matrix and hence result in solidification-related drawbacks. In order to solve these issues friction stir processing (FSP), a derivative method of friction stir welding (FSW), can be applied.

FSW is a solid-state welding method that was invented at The Welding Institute (TWI) of the UK in 1991 [5]. Welding takes place as a nonconsumable rotating tool travels down the joint line of metal plates (see Fig. 2.1). The tool consists of a specially designed pin and an appropriate shoulder, which plays a major role in the heat input,

and subsequently in the quality, of the welds and their mechanical properties (see Fig. 2.1). This technique eliminates most of the drawbacks of fusion welding such as porosity, inclusions, and solidification cracks, as no melting of the material occurs.

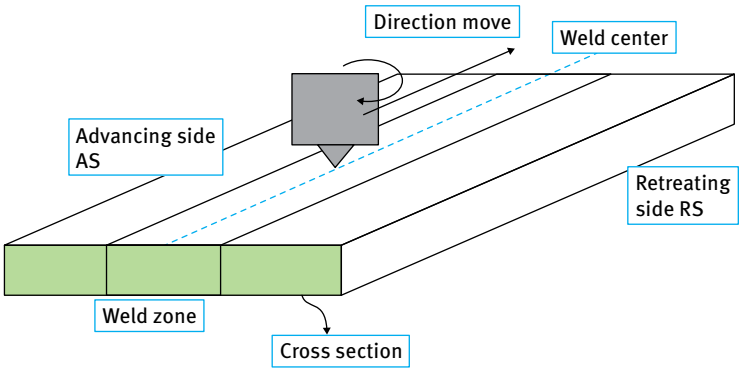

Fig. 2.1: Schematic drawing of friction stir welding.

Friction stir welding can also be used to weld dissimilar alloys. Jonckheere et al. [7] studied the welding of AA2014-T6 with AA6061-T6 and observed that the temperature is relative to the amount of each alloy in the weld nugget. Amancio-Filho et al. [8] studied the mechanical properties of the welding between AA2024-T351 and AA6056-T4, concluding that the welds fail in the area which is annealed by the heat generated by the FSW tool, while Steuwer et al. [9] focused on the residual stresses of the welds of AA5083 with AA6082. Furthermore, Tanaka et al. [10] studied the welding of mild steel with AA7075-T6 and the strength of the weld in relation to the intermetallic compounds' thickness and welding parameters. Regardless of the formation of layers thinner than those of the resolution of FE-SEM IMC, the specimens failed in the AA7075/mild steel weld nugget. Murr et al. [11] studied the welding of AA1100 with AA6061, reporting that the weld zones' microstructure includes some degree of dynamic recrystallization, while in the welding of AA6061 with Cu the dissimilar aluminum/copper system manifested a more complex microstructure. Further work by Murr et al. was conducted on intercalation vortices and related microstructural features in the friction stir welding of dissimilar metals, such as AA2024 with AA6061 and AA6061 with Cu, at various rotational and transverse speeds [12]. They observed that the mixing or vortex-like intercalations at the aluminum/copper weld zone is a manifestation of the solid-state flow, facilitated by dynamic recrystallization in the welds. Also, Cavaliere et al. studied the welding of AA2024 with AA7075, and both the grain structure and precipitates' distribution differences originated by the process were investigated in depth via optical microscopy [13].

Friction stir processing is a promising technique for producing MMCs, and it is mostly used to modify and improve the microstructure, mainly near the surface (see Fig. 2.2). By incorporating the appropriate micro or nanoparticles as fillers into the matrices, enhancement of specific material properties, especially of those that depend on the surface microstructure, is achieved. These particles are introduced into the material's near-surface layers, resulting in localized microstructural modification. As a consequence, FSP technique is emerging to be a very effective solid-state processing technique that can provide localized modification, as well as control of the material microstructure, in the near-surface layers of the processed metallic component. Potential applications of aluminum alloys reinforced with several nanoparticles may include (but are not limited to): high performance structural components requiring high durability, automotive engines and high speed machinery parts requiring high wear and thermal resistance, armor and protection components with the ability to absorb high energy impacts and thermal shocks, aeronautic and aerospace components requiring functionally graded material properties, as well as electronic and optical instruments.

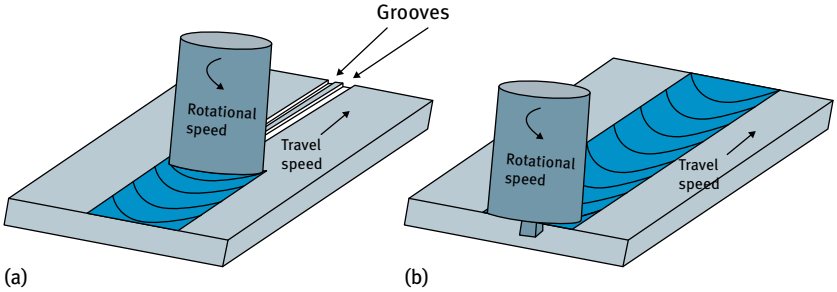

Fig. 2.2: Schematic drawing of (a) FSP cover pass using pin-less tool (b) FSP pass.

Some of the advantages of FSP and FSW are listed below:

(a) FSP and FSW are green processes, as the heat generation originates from friction and plastic deformation, in the absence of toxic fumes, radiation and noise, characteristics that classify FSP as a green and energy-saving technique.
(b) FSP and FSW are short-route, solid-state processing techniques with one step processing that achieve microstructural refinement, densification, and homogeneity.
(c) The microstructure and mechanical properties of the processed zone can be accurately controlled by optimizing the FSP tool design, FSP parameters and the application of active cooling/heating.
(d) The depth of the processed zone can be optionally adjusted by changing the length of the tool pin, with the depth ranging from several hundred micrometers to tens of millimeters; it is difficult to achieve a manually adjusted processed depth using other metalworking techniques.

(e) FSP and FSW are versatile techniques with a comprehensive function for the fabrication, processing, and synthesis of materials.
(f) FSP and FSW do not alter the shape and size of the processed components.

In comparison to unreinforced aluminum alloys, aluminum matrix composites reinforced with ceramic particles exhibit higher strength and stiffness, improved tribological characteristics, as well as increased creep and fatigue strength [14–19]. Metal matrix composite materials are mainly being produced using aluminum alloy substrates reinforced with SiC [20] and Al_2O_3 particles [21], as well as copper substrates reinforced with particles of boron carbide [22]. Furthermore, surface hybrid nanocomposites have been produced and studied; results show improved hardness and mechanical properties when using aluminum alloys substrate and reinforcement of graphite/Al_2O_3 [23]. Carbon nanotubes have been used as reinforcement in the metal matrix as well. Liu et al. applied FSP on AA1016, which had surface holes filled with multiwalled carbon nanotubes [24]. The resulted MMC had superior mechanical properties when compared to the corresponding base metal. Lim et al. produced an AA7075 matrix multi-walled carbon nanotubes (MWCNT) reinforced composite via single pass FSP using a thin AA6111 plate as a cover for the MWCNT filled groove [25]. The distribution of nanoparticles in the metal matrix was inhomogeneous, with multiple FSP passes being a potential solution to that issue. Sun et al. applied FSW with the addition of particles (before friction stir welding, SiC particles were incorporated between two copper plates) [26]; this resulted in the improvement of the mechanical properties of the Cu joints. The same technique was performed by Byung-Wook et al. [27] and Bahrami et al. [28] who improved the mechanical properties of AA5083 and AA7075 joints, respectively, using SiC particles as a reinforcing material. Bahrami et al. [29] also studied the influence of the tool pin design on the distribution of the SiC powder in the weld nugget of AA7075 and the resulting mechanical properties. Although the threaded tapered tool pin resulted in the lowest average microhardness value, the most uniform particle distribution was achieved. Recently, Pantelis et al. [30] incorporated SiC nanoparticles in the weld nugget of dissimilar Friction Stir Weds of AA5083-H111 with AA6082-T6. The results showed improvement of the mechanical properties of the welds as compared to the their reinforcement-lacking counterparts without nanoparticle reinforcement.

2.2 Experimental procedure

Rolled plates of AA5083-H111 and AA6082-T6 with dimensions of $200 \times 100 \times 3$ mm^3 were used as parent materials. Their chemical composition is shown in Table 2.1. The CNTs used as reinforcing material were produced via chemical vapor deposition (CVD). They had an average diameter of 50 nm and length over 10 μm as presented in Fig. 2.3.

Tab. 2.1: Chemical composition of 5083-H111 and 6082-T6 Al alloys (wt.%).

	Si	Fe	Cu	Mn	Mg	Cr	Zn	Ti	Ni	Ga	V	Al
5083-H111	0.37	0.32	0.072	0.53	4.5	0.093	0.044	0.03	0.005	0.011	0.013	bal.
6082-T6	1.07	0.28	0.04	0.7	1.15	0.024	0.04	0.015	0.005	0.013	0.016	bal.

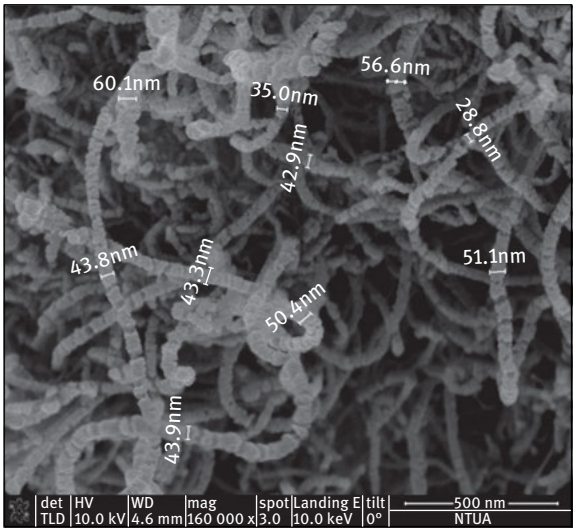

Fig. 2.3: SEM micrograph of the CNTs.

The machine used in the procedure was a custom-made friction stir welding machine of the Shipbuilding Technology Laboratory of the School of Naval Architecture and Marine Engineering of the National Technical University of Athens. The FSW tool was made of heat treated steel "SVERKER 21" (at 61 HRC) and consisted of a flat shoulder with a diameter of 23 mm and a cylindrical left-handed threaded pin with a diameter of 6 mm and height of 2.8 mm.

During the experiments the welding was conducted parallel to the rolling direction of the plates. The nanoparticles were incorporated into half grooves machined at the joining faces of the plates. Fig. 2.4 depicts the groove with dimensions of 180 mm length, 1 mm width and 2.5 mm depth that was created when the plates were rigidly

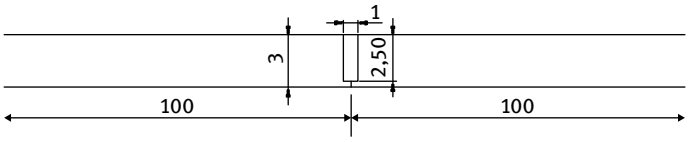

Fig. 2.4: Geometric characteristics of the machined grooves.

connected on the clamping arrangement. The CNTs after being mixed with ethanol to become more manageable were pressed tightly into the groove. The central line of the rotating pin was aligned along with the groove.

After friction stir welding was completed, the specimens were cut at a transverse section in regard to the welding direction, and buffing and polishing was conducted. In order to observe the specimens' microstructure, they were etched with "modified Poulton's reagent" and macroscopically observed using an optical stereoscope (Leica MZ6). The specimens with the best particle distribution were then selected and observed using an optical microscope (Leica DMILM) and a scanning electron microscope (Jeol JSM 6390LV) equipped with the energy dispersive spectroscopy system Oxford Inca Energy 250. The software "Leica Application Suite" was used in order to measure the grain size of the optimum specimen.

A Wolpert Wilson 402MVD microhardness tester was utilized in order to measure the longitudinal Vickers microhardness distributions of the welds. The load applied was 300 g. The average longitudinal microhardness measurements were made along two lines residing 1 mm and 2 mm under the surface.

Tensile specimens were machined perpendicular to the welding direction according to the ASTM E 8M-04 standard. An MTS hydraulic mechanical testing machine of 100 kN maximum load was employed in order to conduct the tensile tests. The elongation was measured with an Epsilon ±25 mm extensometer at a deformation speed of 0.5 mm/min.

Nanoindentation testing was performed using a nanomechanical test instrument, which allows the application of loads ranging from 1 to 30,000 μN and records the displacement as a function of applied loads with high load (1 nN) and displacement resolutions (0.04 nm). The nanomechanical test instrument employed in this study is equipped with a scanning probe microscope (SPM), in which a sharp probe tip moves in a raster scan pattern across the sample surface, using a three-axis piezo positioner. In all nanoindentation tests, a total of 10 indents are averaged to determine nanomechanical values for statistical purposes, with a spacing of 50 μm, in a clean area environment with 45 % humidity and 23 °C ambient temperature. In order to operate under closed loop displacement control (DC), feedback control option was used. The nanoindentation tests were conducted with a Berkovich (three-side pyramid) diamond indenter (average radius of 100 nm) with 40 s loading and unloading segment time separately and 3 s of holding time at various penetration depths. All nanoindentation measurements were performed 2 mm under the welding substrate, longitudinally and in transverse directions (in the middle of the weld nugget), at the cross-section of the welds. Prior to indentation, the area function of the indenter tip was calibrated in fused silica, a standard calibration material [31]. The surface of the samples prior to conducting the nanoindentation measurements, was prepared by grinding and polishing.

2.3 Results and discussion

To the best of the authors' knowledge, there has been no study related to the FSW of dissimilar aluminum alloys with the addition of CNTs. In this work, the optimization of welding of the dissimilar aluminum alloys AA5083-H111 and AA6082-T6 with incorporation of CNTs was studied by changing the tool rotational and travel speed as well as the number and the direction of FSW passes, which affect the distribution of the nanoparticles in the weld nugget. Also, the present work focuses on the mechanical properties of the optimum joint by tensile and indentation methods. The results were then compared to an identical joint without reinforcement. Nanoindentation was used to elucidate the effect of reinforcing fillers on the mechanical properties taking into account the microstructure. Two series of experiments were conducted. The choice of parameters for the first experiment lies on on the authors' experience from past experiments with other nanofillers incorporated into metal matrices, whereas the parameters of the second one were determined by Taguchi analysis. Both of them are analysed in the following paragraphs.

2.3.1 First series of experiments

First, the optimum parameters of welding AA5083-H111 to AA6082-T6 without carbon nanotube addition were determined by altering the rotational speed from 600 to 1180 RPM, the traverse speed from 60 to 85 mm/min and the tool tilt angle from 0 to 4 °. These parameters are presented in Table 2.2. It should be mentioned that the resulting specimen was also used for comparison purposes.

Tab. 2.2: Optimum welding parameters of the unreinforced welding of AA5083-H111 with AA6082-T6.

Passes (mm)	Rotational speed (RPM)	Traverse speed (mm/min)	Shoulder diameter (mm)	Tool pin height (mm)	Tool Pin diameter (mm)	Tool pin shape	Tilt angle	Tool pin penetration Depth (mm)
1	750	85	23	3	6	cylindrical threaded	3 °	2.50

An FSW test with CNT addition was conducted adopting the above parameters (test 5 on Table 2.3), but it presented defects such as porosity and severe CNT agglomeration. According to literature [32], a more uniform nanoparticle distribution in the weld nugget can be achieved by increasing the number of FSP passes. Also, various studies conducted in the Shipbuilding Technology Laboratory regarding friction stir processing, indicated that alternating the direction of the FSP passes as well as increasing

the rotational speed of the tool can have a positive impact on the distribution of the nanoparticles. Based on this feedback, the authors concluded in the conditions presented in Table 2.3 for the various friction stir tests that they conducted. The same tool was used in all experiments, namely one with a cylindrical left-hand threaded pin. This was because the material flow created by this specific pin, results in very good material mixing. The transverse speed, tool tilt angle and tool pin penetration depth were also kept constant at 85 mm/min, 3 °, and 2.50 mm respectively, because alternating the rotational speed is sufficient a variable in order to change the weld pitch. The theoretical volume fraction (V_f) of the carbon nanotubes in the weld nugget, which is calculated by equation (1) according to literature [22], was 13.8 % in every experiment:

$$V_f = \frac{\text{Area of groove}}{\text{Projected area of tool pin}} * 100 \tag{2.1}$$

In all the tests the + and – symbols denote that the AA5083-H111 is located at the advancing and the retreating side, respectively. It should also be noted that, for all the experiments, before the welding process the grooves were covered by one FSP pass with a flat pinless tool 23 mm in diameter, using the same conditions of the welding, in order to prevent the CNTs from being ejected out of the groove during FSW.

Tab. 2.3: Welding parameters of AA5083-H111 with AA6082-T6 with nanoparticle reinforcement.

N° of specimens	Number of passes (mm)	Rotational speed (RPM)	Direction of passes
1	3	750	+ + +
2	2	750	+–
3	2	1180	+–
4	3	1180	+ + +
5	1	750	+
6	2	750	++
7	2	1180	++
8	1	1180	+
9	4	750	+ + ++

2.3.1.1 Macrostructural study

The macrographs of the cross section of all the specimens (except specimen 9) are presented in Fig. 2.5. Specimen 9 presented a massive groove-like defect, and as a result it could be neither buffed nor polished. By observing the micrographs at Figs. 2.5(a) and (d), it is concluded that the application of three passes in the same direction resulted in a better distribution of the particles and exhibited lower particle agglomeration levels than the application of less – as well as more – passes. It is also observed that the increase of the rotational speed created a more homogeneous distribution and a thinner flow arm. The application of two passes of the opposite direction creates an heterogeneous distribution as there were large particle-rich and particle-free areas (specimens

2 and 3 presented at Figs. 2.5(b) and (c), respectively). Furthermore intense agglomeration is observed, mainly in the advancing side. The presence of formed agglomerates near the heat affected zone after the application of one and two passes (specimens 2, 5, 6, 7, 8), can mainly be attributed to the left-handed screw pin, which directed the material downwards at the center and then upwards near the heat affected zone [33]. In fact, the application of the third pass of the same direction (specimen 4 – Fig. 2.5(d)) improves the distribution, in comparison to the two-pass experiments, as only a small area consisting of agglomerated particles can be observed in the upper area of the retreating side. The weld nugget of specimen 4 is the best formed weld nugget compared to all the other specimens.

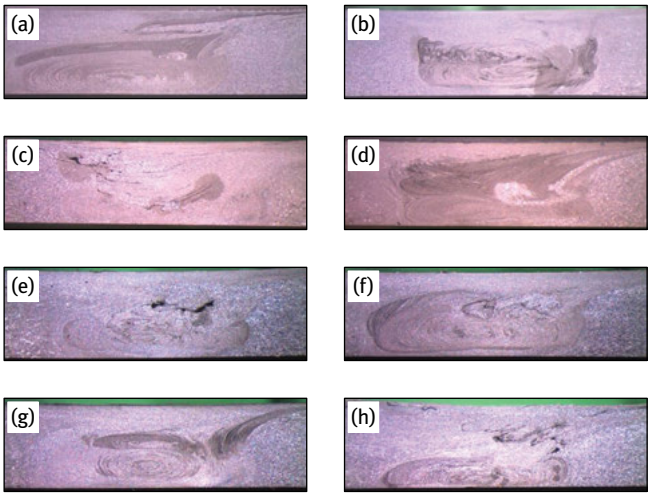

Fig. 2.5: Optical stereoscopy macrographs of the cross sections of the specimens after etching. Test: (a) 1, (b) 2, (c) 3, (d) 4, (e) 5, (f) 6, (g) 7, (h) 8.

After the observation of the macrographs for all the specimens, it is concluded that specimen 4 presents the most uniform macrostructural morphology, and taking into account the absence of defects, it comprises the optimum weld with nanoparticles; therefore it was further studied, as shown in the next paragraphs.

In Fig. 2.6 the macrostructure of the weld nugget of the specimen without reinforcement is presented for comparison purposes. The absence of defects, a large flow arm, and an onion ring structure can be observed. The microstructure of the weld nugget is presented in Fig. 2.6(b). Good material mixing is observed in both micrographs and the weld nugget (WN) microstructure characterized by small and equiaxial grains with a grain size of ~13 μm.

The reduction of the grain size of the weld without reinforcement in the WN, compared to that of the untreated base metals (5083: 26 μm and 6082: 40 μm), is a result

of the dynamic recrystallization which, according to the literature [34, 35], took place during FSW.

By comparing Figs. 2.5(d) and 2.6(a) it can be concluded that the material mixing appears to be better in Fig. 2.5(d) (note that the carbon nanotubes appear as dark areas under the optical microscope). That is expected because of the higher number of passes.

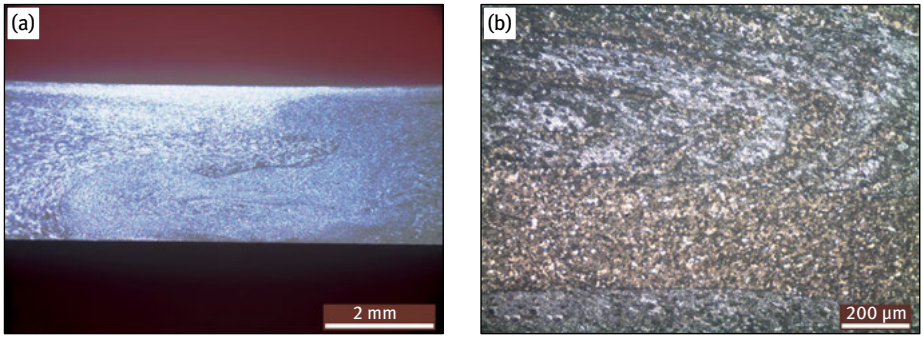

Fig. 2.6: (a) Optical macrograph of specimen 5; (b) optical micrograph of the weld nugget.

2.3.1.2 Microstructural study

In Fig. 2.7 areas of the weld nugget of specimen 4 are observed by means of optical microscopy. In Fig. 2.7(a) the lower half of the weld nugget, which is poor in CNTs, is depicted. It is observed that both the AA6082 and AA5083 are mechanically mixed into the metal matrix. In Figs. 2.7(b) and (c) the upper half of the weld nugget, which is rich in carbon nanotubes, is observed. It is also observed that the CNTs are arranged in bands into the aforementioned metal matrix. Also, some agglomeration can be noted, depicted with arrows in Figs. 2.7(b), (d) and will be further analysed with the assistance of scanning electron microscopy and energy dispersive spectroscopy. In Fig. 2.7(d) the CNT bands (dark areas) are shown in higher magnification.

Finally, the weld nugget consisted of equiaxial grains with an average grain size of ~6 µm. The smaller grain size that is observed in this specimen in comparison to the one of the specimen without CNTs is, according to the literature, a result of the pinning effect [27, 28] that CNTs have had in this region, thus impeding grain growth.

In Fig. 2.8 secondary electron SEM images of areas of the weld nugget are presented. In Fig. 2.8(a) the particle poor region of the lower half of the weld nugget is presented. The mixing of the two aluminum alloys is without pores or defects. In Fig. 2.8(b) the aforementioned CNT bands are presented. In Figs. 2.8(c) and (d) clusters formed by agglomerated CNTs are observed.

In Fig. 2.9 a backscatter electron SEM image of the CNT bands of Fig. 2.8(b) as well as the EDS graphs of the two distinctive areas (CNTs and metal matrix) are presented. In the metal matrix, no carbon content was measured, thus confirming the arrange-

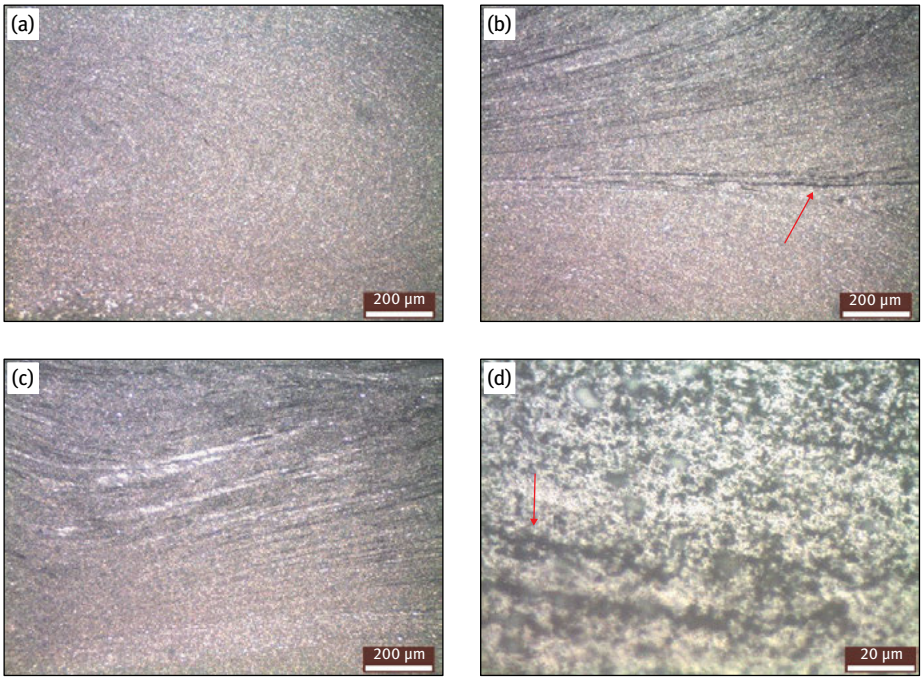

Fig. 2.7: Optical micrographs of several areas of the weld nugget of the specimen 4 (a,b,c) 100× magnification, (d) 1000× magnification.

ments of CNTs in specific bands. The measured magnesium is an alloying element of both the AA6082 and AA5083.

In Fig. 2.10 a backscatter electron SEM image of the CNT cluster of Fig. 2.8(c) as well as the EDS graphs of the distinctive areas (CNTs and metal matrix) are presented. The agglomeration of CNTs in specific areas that was observed by the optical and secondary electron SEM images is supported by the fact that a high amount of carbon is measured in the aforementioned cluster.

It should be mentioned that the chemical composition of the elements arising from of the EDS analysis is not listed, because carbon is a low atomic weight element and the results present a large rate of error.

2.3.1.3 Microhardness study

The microhardness mean average of the base metal AA6082-T6 was ~105 HV0.3, while this of the AA5083-H111 was ~80 HV0.3 (used as reference values). As observed in Fig. 2.11, the microhardness of the optimum weld with nanoparticles was higher compared to this of AA5083-H111, for two different distances from the surface. Nevertheless lower microhardness values were observed at 1 mm from the surface, especially in the

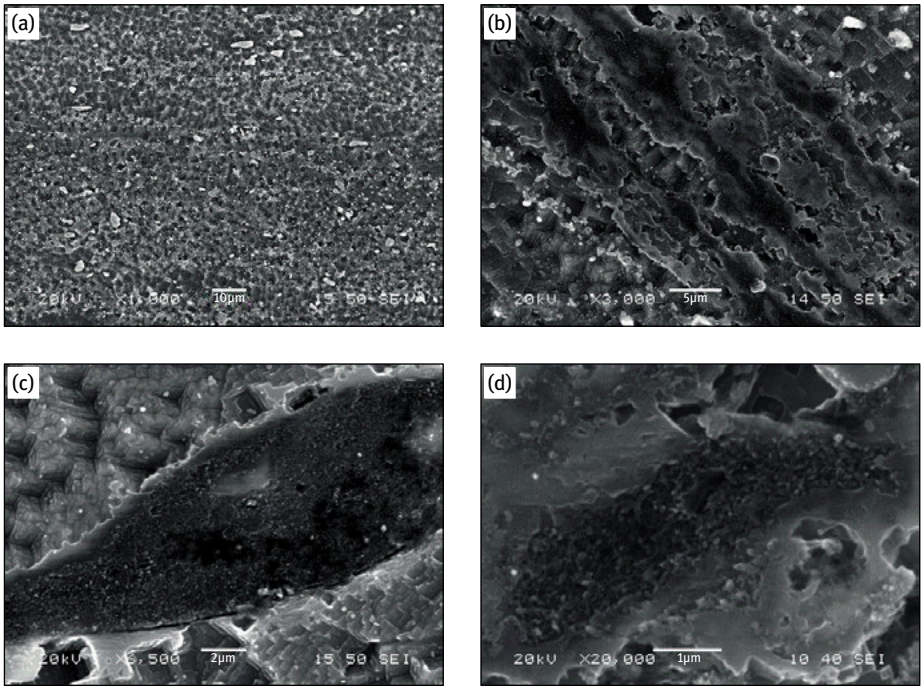

Fig. 2.8: Secondary electron SEM micrographs of several areas of the weld nugget of specimen 4: (a) 1000× magnification; (b) 3000× magnification, (c) 6500× magnification; (d) 20000× magnification.

retreating side, because of the flow arm of the specimen which had larger grains than the weld nugget and was not as rich in particles. In the other welding zones (thermo-mechanically affected zone, heat affected zone) the microhardness distribution was almost the same at all distances from the shoulder surface with the exception of the 6082 HAZ, which extends further as we get closer to the surface due to the annealing effect that takes place.

As shown in Fig. 2.12, the microhardness distribution of the weld without the addition of nanoparticles at a distance of 2 mm from the surface presented lower values (an average 70 HV0.3) in the weld nugget compared to these of the specimen with CNTs at the same distance from the surface. This is a consequence of the fact that, according to the Hall–Petch relation, the hardness increases as grain size decreases [28], and in fact it was observed that the composite weld nugget consisted of smaller grains than the weld nugget without reinforcement. The lowest values were observed in the heat affected zone, at the side of AA6082-T6 (~54 HV0.3) due to the dissolution of the strengthening precipitates, as referred in the literature [36].

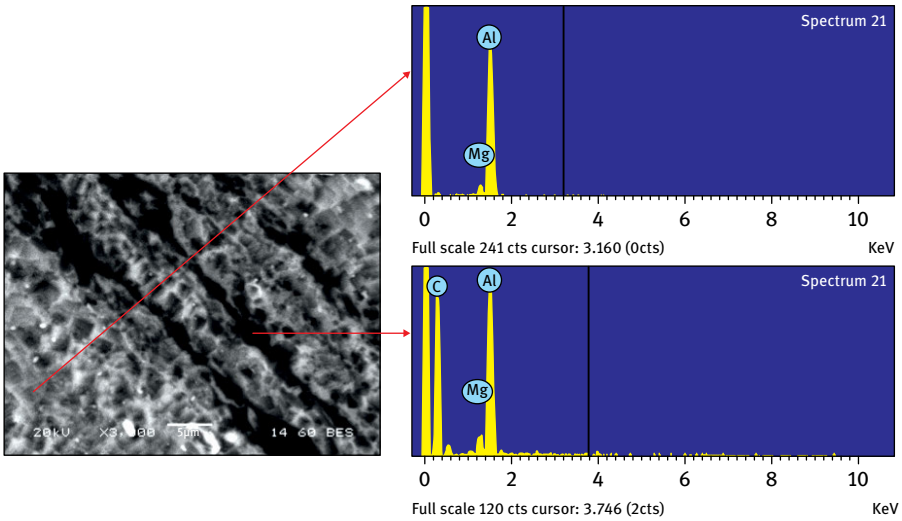

Fig. 2.9: Backscatter SEM micrograph and the EDS graphs of the areas shown with arrows.

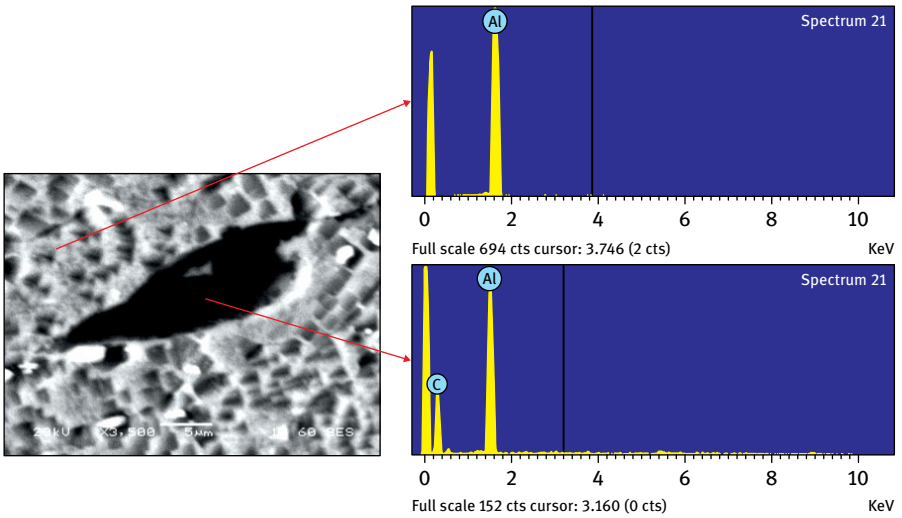

Fig. 2.10: Backscatter SEM micrograph and the EDS graphs of the areas shown with arrows.

2.3.1.4 Tensile tests

The mechanical properties of the created welds are determined via several metallurgical mechanisms (dissolution and precipitation of secondary phases, dynamic recrystallization) as well as the material flow during FSP. Three tensile specimens were created using the welding conditions of specimen 4. The representative stress-strain curves for that specimen, as well as for the one without reinforcing particle addition,

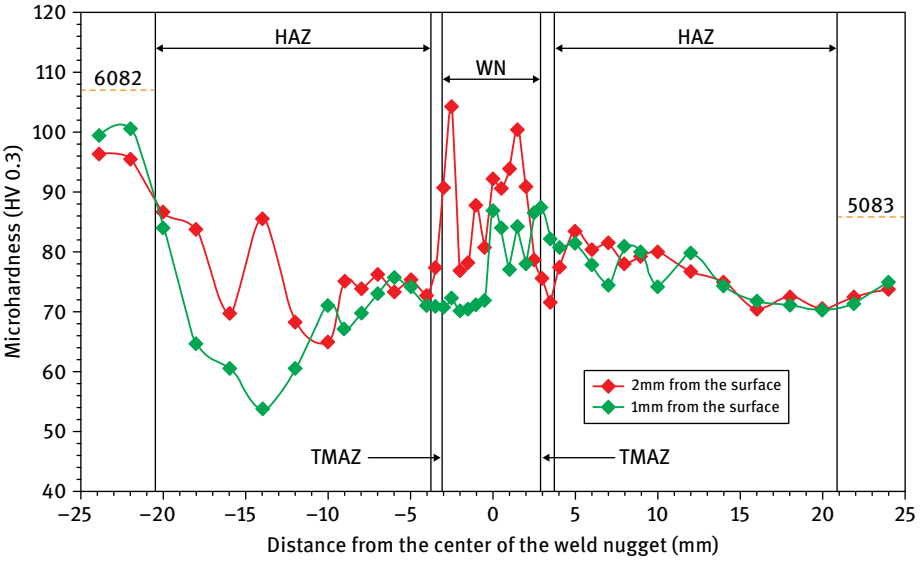

Fig. 2.11: Microhardness distribution of the weld with the addition of CNTs. The transverse lines referred to the limits of the zones for the case of hardness distribution realized at 2 mm under the surface.

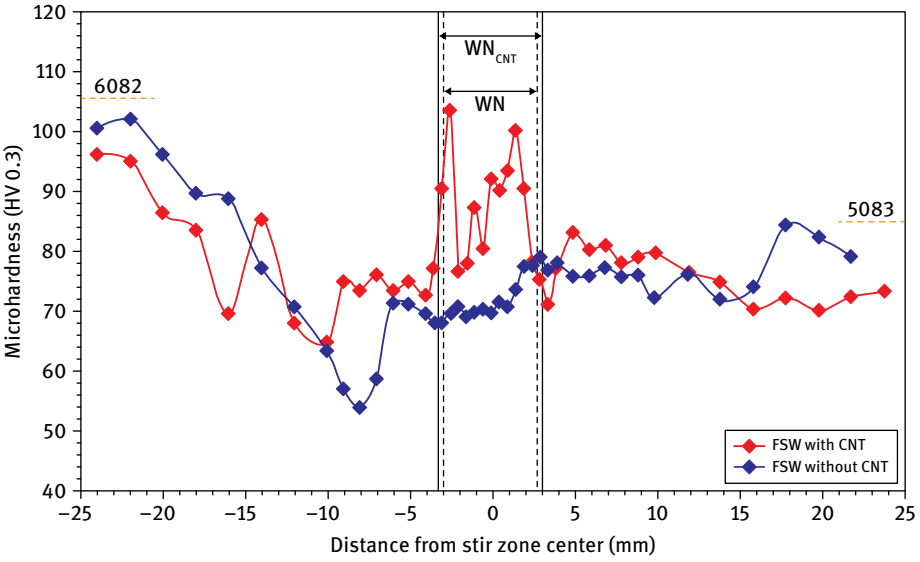

Fig. 2.12: Microhardness distribution (2 mm under the surface) of the welds, with and without CNTs.

are presented in Fig. 2.13. Table 2.4 shows the average values for the elastic modulus, yield stress, ultimate tensile strength (UTS), and percentage of elongation. The values of all the magnitudes dropped with nanoparticle addition. That is because all the specimens failed in the weld nugget, probably due to the fact that the CNTs get tangled during the stirring action of the tool resulting in severe agglomeration, as confirmed by the SEM micrographs and the EDS analysis. On the other hand, the unreinforced weld failed in the HAZ. Failure took place exactly at the location of the minimum hardness value that is in the HAZ of 6082 aluminum alloy.

Tab. 2.4: Mechanical properties (average values of three tests for each case) of the welds, with and without the addition of CNTs.

Specimen	Elastic modulus (GPa)	Yield stress (MPa)	UTS (MPa)	Elongation (%)
with CNTs	70 ± 0.05	128 ± 2.8	155 ± 2	0,95 ± 0.1
without CNTs	65 ± 0.1	140 ± 3.6	193 ± 2	3 ± 0.05

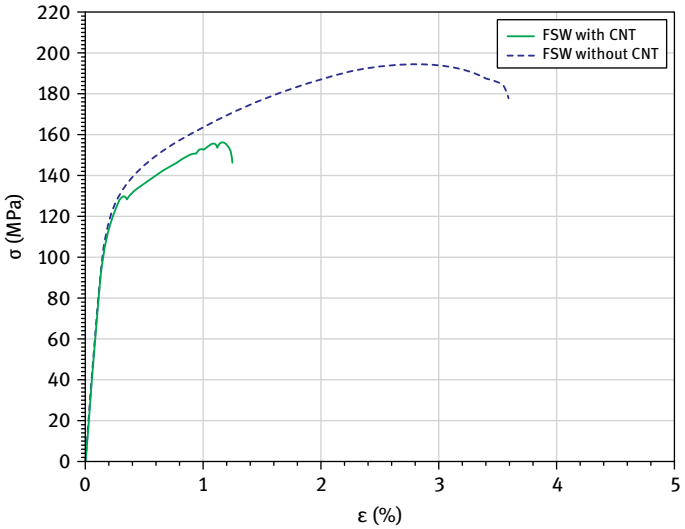

Fig. 2.13: Stress-strain curves for the welds with and without CNT reinforcement.

2.3.1.5 Fractography

The fracture surface of the weld of specimen 4 is presented in Fig. 2.14. It is situated at the WN. Although an overall brittle fracture morphology can be observed (Fig. 2.14(a,b,d)), there are some small areas that are characterized by the presence of small dimples, indicative of ductile fracture (Fig. 2.14(c)). The large dark colored cavities that are presented in Fig. 2.14(a) and (b) may be CNT clusters. These may act as sites that trigger the fracture.

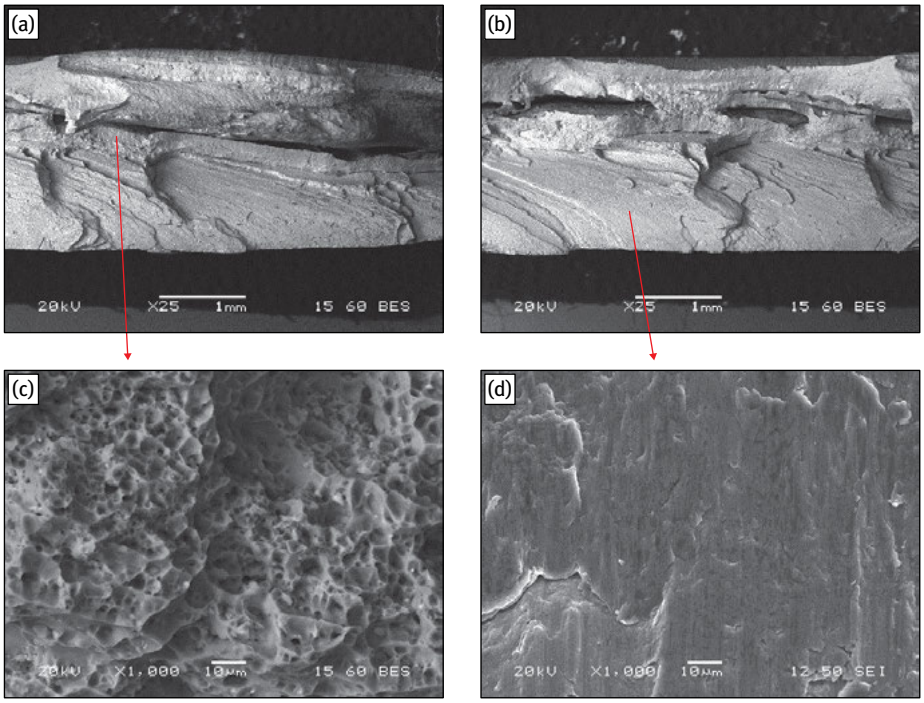

Fig. 2.14: Backscatter electron SEM micrographs of the fracture plane at the WN of the specimen 4 (c, d) Further magnification of the areas shown with arrows.

2.3.1.6 Mechanical properties measured by nanoindentation

Basic theory

Nanoindentation tests involve the contact of an indenter with a material surface and its penetration due to a specified load or depth. According to the Oliver and Pharr (O&P) method, the nanoindentation hardness (nanohardness (H_{nano}) hereafter) can be determined as a function of the final penetration depth of indent by [37]:

$$H = \frac{P_{max}}{A(h_c)}, \tag{2.2}$$

where P_{max} is the maximum applied load measured at the maximum depth of penetration (h_{max}), $A(h_c)$ is the projected contact area between the indenter and the specimen. For a Berkovich indenter $A(h_c)$ can be expressed as a function of the contact indentation depth h_c as

$$A(h_c) = 24,5h_c^2 + a_1h_c + a_{1/2}h_c^{1/2} + \cdots + a_{1/16}h_c^{1/16}. \tag{2.3}$$

The contact indentation depth, h_c, can be determined from the following equation:

$$h_c = h_{max} - \varepsilon\frac{P_{max}}{S}, \tag{2.4}$$

where ε is an indenter geometry constant equal to 0.75, for Berkovich indenter, S is the contact stiffness which can be determined as the initial slope of the unloading curve at the maximum penetration depth, i.e.

$$S = \left(\frac{dP}{dh}\right)_{h=h_{\max}}. \tag{2.5}$$

Based on Sneddon's [38] elastic contact theory, the reduced elastic modulus, E_r, is given by the following expression:

$$E_r = \frac{S}{2\beta}\sqrt{\frac{\pi}{A\,(h_c)}}, \tag{2.6}$$

where β is a constant that depends on the geometry of the indenter. For the Berkovich indenter, β is equal to 1.167 [38, 39]. The Elastic modulus of the specimen, E, can be calculated as follows:

$$\frac{1}{E_r} = \frac{1-\nu^2}{E} + \frac{1-\nu_i^2}{E_i}, \tag{2.7}$$

where v, E are the Poisson ratio and the elastic modulus of the specimen, respectively, and v_i, E_i are the Poisson ration and elastic modulus of the indenter, respectively (for a diamond indenter, E_i is 1140 GPa and ν_i is 0.07).

Nanohardness and elastic modulus distribution

Nanoindentation tests were performed in order to study the deformation mechanism of the composite (AA5083-H111/AA6082-T6 with CNTs) in the weld nugget and to measure the elastic modulus and nanohardness values of the different weld areas. Measurements were performed across the weld zone 2 mm under the shoulder surface and perpendicular to the middle of the weld nugget, at the cross-section of the welds.

The mean average of nanohardness (H_{nano}) distribution across the weld was calculated to be lower than that of the parent materials, mainly at the side of AA6082-T6 parent material. Decreased values were observed in the HAZ, at the side where AA6082-T6 was located, due to the dissolution of the strengthening precipitates, as discussed in the literature [36]. However, the values were found to increase in the WN because of the presence of CNTs, but they were still found to be lower than, if not equal to, the nanohardness of AA5083-H111 parent material (Fig. 2.15).

The overall micro- and nanohardness distributions (Figs. 2.11 and 2.15) across the weld showed almost the same trend: hardness reduction from the BM, starting from the HAZ, reaching a local minimum at the HAZ from the side of AA6082-T6 and a rise to higher values in the SZ. However, comparing the two distributions (Figs. 2.11 and 2.15) in the weld nugget, the hardness results were significantly different in the weld nugget, taking into account the hardness values of parent materials as reference points. More precisely, the microhardness values were found to be slightly higher (8 %) than the microhardness values of the AA5083-H111 parent material, whereas the nanohardness

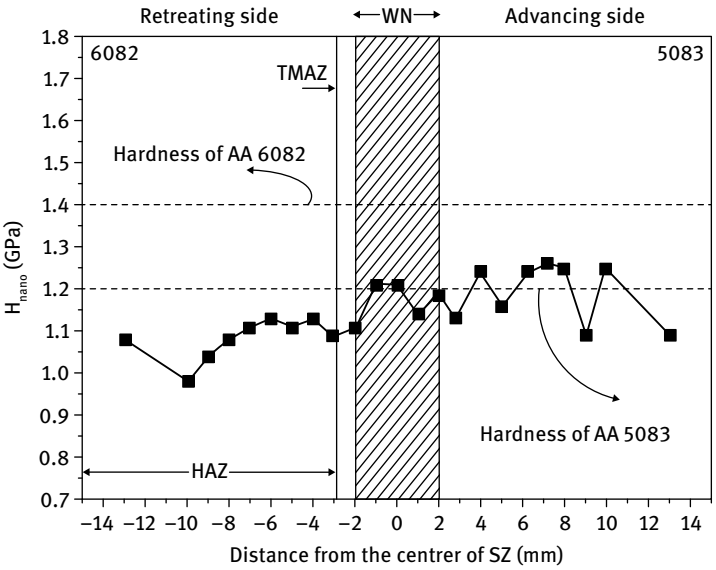

Fig. 2.15: Nanohardness distribution of the weld with the addition of CNTs obtained from nanoindentation experiments at 400 nm maximum penetration depth (2 mm under the surface).

values were found to be lower than or equal to the nanohardness values of the AA5083-H111 parent material.

This divergent behavior can be attributed to the size of the probed volume during indentation. During microhardness testing, the volume of the deformed plastic region is sufficiently large (the diameter of the residual impression is ~85 μm), as compared to the grain size, and the deformation is influenced by both the grain boundaries and the presence of reinforcing particles. On the other hand, the plastic zone during nanoindentation, which is related to the nanohardness values, is much smaller (the diameter of the residual impression is ~1.5 μm). Details and discussion of the volumes of plastic and elastic deformation under contact indentation loading have already been presented elsewhere [40]. In order to reveal the reinforcing mechanisms and the testing method's dependence on the hardness values, it is necessary to establish the relations between the micro- and nanohardness for both particle reinforced and unreinforced joints. Further investigation should be conducted in order to elucidate this phenomenon, which is beyond the scope of this chapter.

Also, it is critical to explain that the probed volume for the elastically deformed region is not the same as that of the plastically deformed region. The size of the elastically deformed region is larger than that of the plastically deformed region. This is also supported from the results presented in Fig. 2.16 and discussed below. It is depicted in Fig. 2.16 that the welding process results in lower elastic modulus values in the side of 6082 HAZ. However, the values were found to increase in the WN because of the presence of CNTs. The mean average elastic modulus, measured with tensile tests, of

both base metals was 71.7 GPa. The reference lines illustrated in Fig. 2.16 correspond to the elastic moduli, measured by tensile tests, of the specimens with and without CNTs. It is evidenced that the addition of CNTs results in higher elastic modulus (the elastic modulus increased up to 15 %) in the SZ, equal in the advancing side and lower in the HAZ from the retreating side, compared to the elastic moduli of the parent materials.

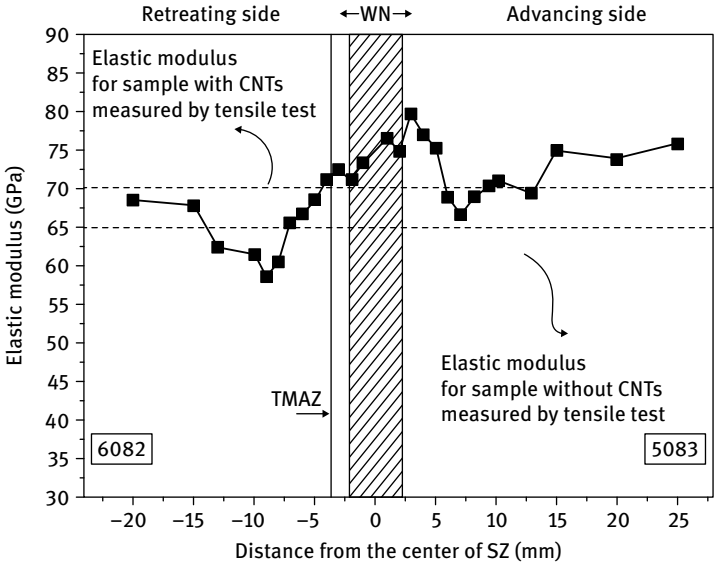

Fig. 2.16: Elastic modulus distribution of the weld with the addition of CNTs obtained from nanoindentation experiments at 400 nm maximum penetration depth (2 mm under the surface).

2.3.2 Second series of experiments

All the specimens of the first series of experiments failed in the weld nugget, suggesting that the chosen conditions could possibly be improved. As a result the authors proceeded to use the Taguchi method in order to further optimize the welding parameters of the first series of experiments.

The most significant process parameters of FSP are the following:

(1) rotational speed of the tool (rpm);
(2) welding speed or transverse speed (mm/min);
(3) number of processing passes;
(4) tool geometry: (a) pin profile, (b) tool shoulder diameter, D (mm), (c) pin diameter, d (mm), (d) D/d ratio of tool, (e) pin length (mm), (f) tool inclination angle (°).

Taguchi addresses quality in two main areas: offline and online quality control. The most important difference between a classical experimental design and a Taguchi-

method-based robust design technique is that the former tends to focus solely on the aspect of the quality characteristic while the latter takes into consideration the minimization of the variance of the characteristic of interest. Although the Taguchi method has drawn much criticism due to several major limitations, it has been able to effectively solve single response problems.

In the second series of experiments the same FSW parameters as in the first series were altered, namely the rotational speed, number of passes, and direction of passes whereas the transverse speed, tool tilt angle, and tool pin penetration depth were kept constant at 85 mm/min, 3 °, and 2.50 mm, respectively. The theoretical volume fraction of the carbon nanotubes in the weld nugget was also 13.8 % in every experiment. In total, 8 FSW joints of AA5083-H111 with AA6082-T6 were produced following the Taguchi scheme presented in Table 2.5. Throughout the Taguchi statistical analysis, only 24 (8x3) experiments for L8 orthogonal arrays are needed for microstructural observation and mechanical tests.

Tab. 2.5: Welding parameters of AA5083-H111 with AA6082-T6 with nanoparticle reinforcement.

N ° of specimen	Number of passes (mm)	Rotational speed (RPM)	Direction of passes
1	1	1500	+
2	2	1500	+–
3	3	750	+ – +
4	3	1180	+ – –
5	3	1500	+ + –
6	3	1500	+ + +
7	3	1180	+ – +
8	2	1500	++

In all the tests the + and – symbols denote that the AA5083-H111 is located at the advancing and the retreating sides, respectively. It should also be noted that, as in the first series of experiments, before the welding process the grooves were also covered by one FSP pass with a flat pinless tool 23 mm in diameter in order to prevent the CNT nanoparticles from being ejected out of the groove during FSW, using the same conditions of welding.

2.3.2.1 Macrostructural study

In Fig. 2.17 the optical macrographs of the Taguchi optimized experiments are presented. All the specimens present a large flow arm that appears light colored and is therefore characterized by a low CNT concentration. Also, by observing the micrographs it is concluded that increasing the machine's rotational speed to 1500 RPM improves the nanoparticle distribution in the weld nugget. Despite the second speci-

men's large flow arm, it presents the least agglomeration and appears to have the best microstructure of all the specimens, presenting the typical "onion ring" structure of friction stir welding. This will be further examined by means of optical and electronic microscopy, microhardness measurement, and tensile testing.

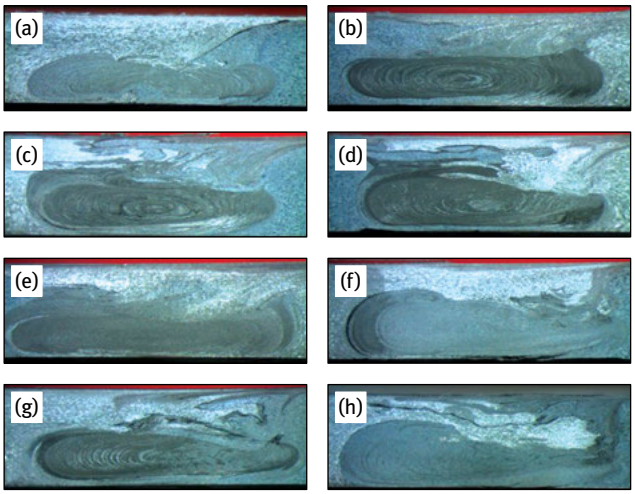

Fig. 2.17: Optical stereoscopy macrographs of the specimens after etching. Test: (a) 1, (b) 2, (c) 3, (d) 4, (e) 5, (f) 6, (g) 7, (h) 8.

2.3.2.2 Microstructural study

In Fig. 2.18 the microstructure of several areas of the weld nugget of specimen 2 can be observed by means of optical microscopy. The left side, right side, and center of the weld nugget of Fig. 2.17(b) are presented in Fig. 2.18(a,b), and (c), respectively. The weld nugget appears to be rich in CNTs and presents the typical onion ring structure, consisting of alternating bands with different amounts of nanotubes. That can also be observed in higher magnification in Fig. 2.18(d).

In Figs. 2.19(a) and (b), secondary electron SEM images of the center of the weld nugget are presented. The mixing of the two aluminum alloys is without pores or defects. The CNT agglomeration observed in the first series of experiments is absent, and the CNTs are indistinguishable in the metal matrix as a result of the homogeneous distribution that was achieved.

2.3.2.3 Microhardness study

In Fig. 2.20 the longitudinal microhardness distribution of specimen 2 at two different distances, 1 and 2 mm from the tool surface, is presented. The microhardness values in the weld nugget are lower in the first case because of the presence of the flow arm.

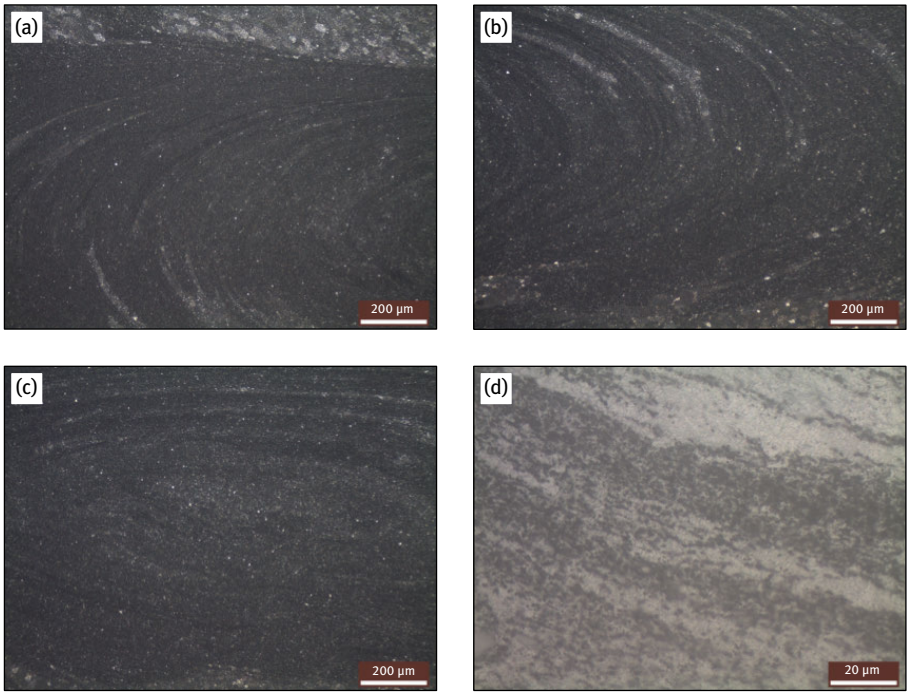

Fig. 2.18: Optical micrographs of several areas of the weld nugget of the specimen 2: (a) the left side of the wn, 100× magnification; (b) the right side of the wn, 100× magnification; (c) the center of the weld nugget, 100× magnification; (d) alternating bands, 1000× magnification.

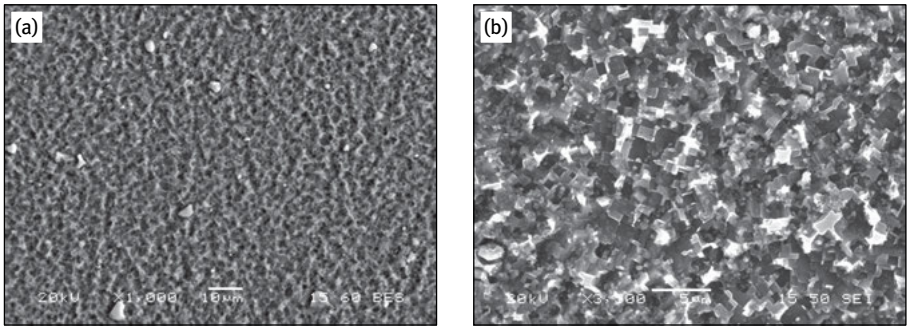

Fig. 2.19: Secondary electron SEM micrographs of (a) the center of the weld nugget, 1000× magnification, (b) the center of the weld nugget, 3500× magnification.

In the first set of experiments, they are also lower, ranging from 60 HV0.3 to 80 HV0.3, compared to the equivalent of specimen 4 of the first series of experiments, ranging from 70 HV0.3 to 90 HV0.3 (see Fig. 2.11), but they present a flatter graph with fewer low and high peaks. This is due to the more homogeneous nanotube distribution in the

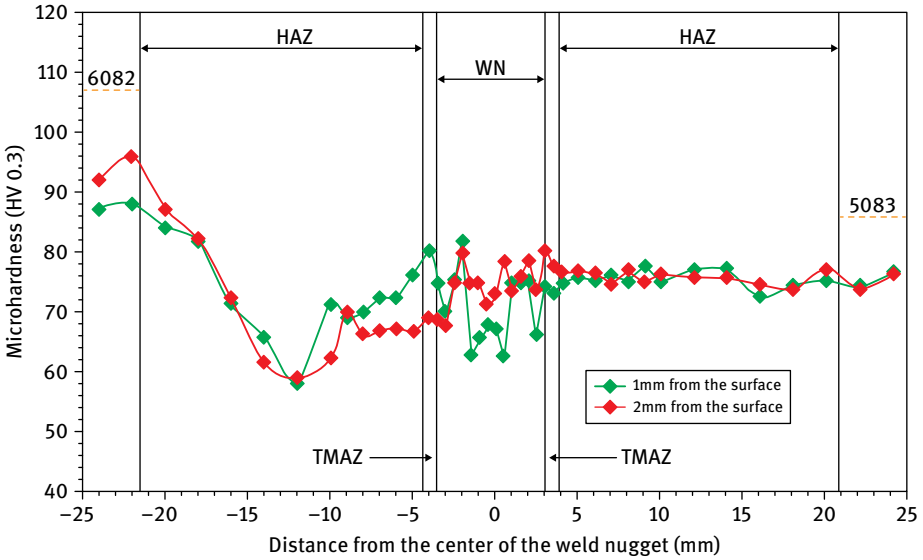

Fig. 2.20: Microhardness distribution of specimen 2 with the addition of CNTs. The transverse lines referred to the limits of the zones for the case of hardness distribution realized at 2 mm under the surface.

weld nugget, which can also be characterized by the absence of agglomeration, as mentioned in Section 2.3.2.2. In the other welding zones (TMAZ, HAZ), the microhardness distribution is in correlation with the corresponding ones of the first set of experiments.

In Fig. 2.21 the longitudinal microhardness distribution of specimen 2 is compared with the equivalent of the specimen without CNTs, both taken at 2 mm from the tool surface. The values of the reinforced specimen are slightly higher than the equivalent of the unreinforced one.

2.3.2.4 Tensile tests

As can be observed from Table 2.6 and Fig. 2.22, the average values for the ultimate tensile strength (UTS) and percentage of elongation are improved in comparison to the equivalent values of the first set of experiments (see Table 2.4 and Fig. 2.13). Despite that, they are still inferior compared to the equivalent of the unreinforced specimen, which failed in the heat affected zone. It should be noted that the reinforced specimens failed at the weld nugget as it can be observed in Section 3.2.5 as well. On the other hand, the values of the elastic modulus and the yield stress of the reinforced specimens are very close, and within the error limits, to the equivalent of the unreinforced ones. These results demonstrate that the carbon nanotube addition has a negative impact mainly on the plastic (and not in the elastic) behavior of the material. Further investigation should be conducted regarding this phenomenon.

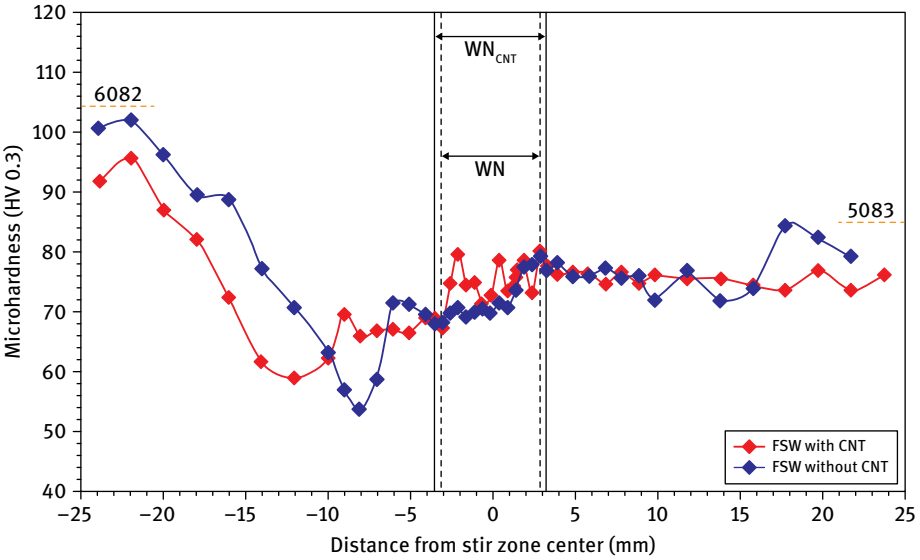

Fig. 2.21: Microhardness distribution (2 mm under the surface) of the welds, with and without CNTs.

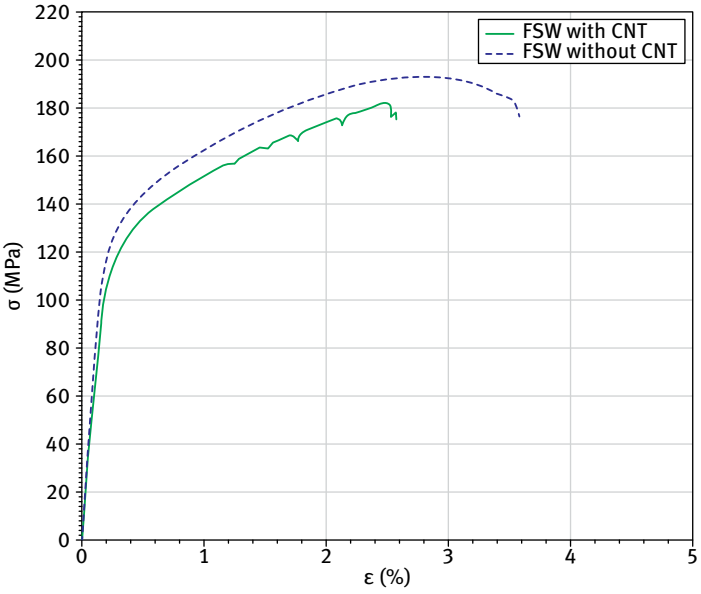

Fig. 2.22: Stress – strain curves for the welds with and without CNT reinforcement.

Tab. 2.6: Mechanical properties (average values of three tests for each case) of the welds, with and without the addition of CNTs.

Specimen	Elastic modulus (GPa)	Yield stress (MPa)	UTS (MPa)	Elongation (%)
With CNTs	70 ± 0.1	130 ± 6.43	177 ± 12	1,4 ± 0.64
Without CNTs	65 ± 0.1	140 ± 3.6	193 ± 2	3 ± 0.05

2.3.2.5 Fractography

The fracture surface of the weld of the specimen 2 is presented in Fig. 2.23. It is situated at the WN. Although it presents an overall brittle fracture morphology (Fig. 2.23(a,b,d)), there are some small areas that are characterized by the presence of small dimples, indicating ductile fracture (Fig. 2.23(c)). The brittle fracture morphology in combination to the fact that the specimens fractured at the weld nugget, indicates that the CNT addition lowered the ductility of the material in the weld nugget region.

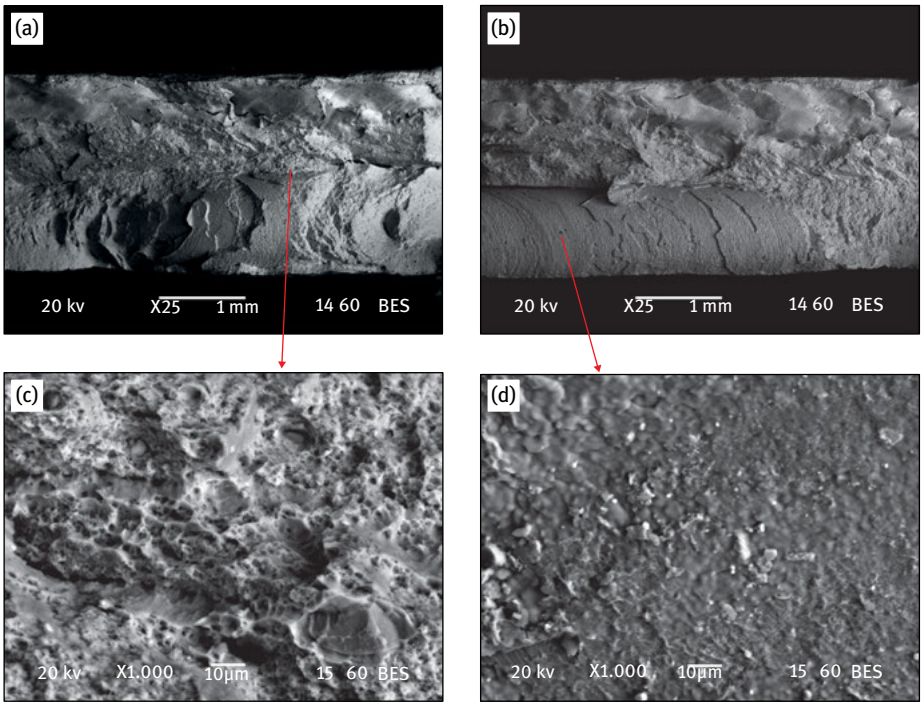

Fig. 2.23: (a, b) Backscatter electron SEM micrographs of the fracture plane at the WN of the specimen 2, (c, d) further magnification of the areas shown with arrows.

2.3.2.6 Mechanical properties measured by nanoindentation

In Fig. 2.24 the longitudinal nanohardness distribution of second specimen at 2 mm under the shoulder surface, at the cross-section of the weld, is presented. Nanohardness values were extracted from nanoindentation load-unload curves; the experimental set-up and method are presented above in Sections 3.1 and 3.2.5, respectively. The mean average of nanohardness (H_{nano}) distribution across the weld was found lower than this of the parent materials, mainly at the side of AA6082-T6 parent material. Decreased values were observed in the HAZ, at the side where AA6082-T6 was located, due to the dissolution of the strengthening precipitates, as referred in the literature [36]. However, the values were found to increase in the WN because of the presence of CNTs, but were still found to be lower than the nanohardness of AA5083-H111 parent material (Fig. 2.24) Comparing the nanohardness distributions of the first and second sets of experiment (Figs. 2.15 and 2.24) the same trend is observed. However, in the case of the second set of experiments the microhardness values were found to reach the microhardness values of the AA5083-H111 parent material, in the SZ, whereas the nanohardness values were appear to be lower than the nanohardness value of AA5083-H111 parent material.

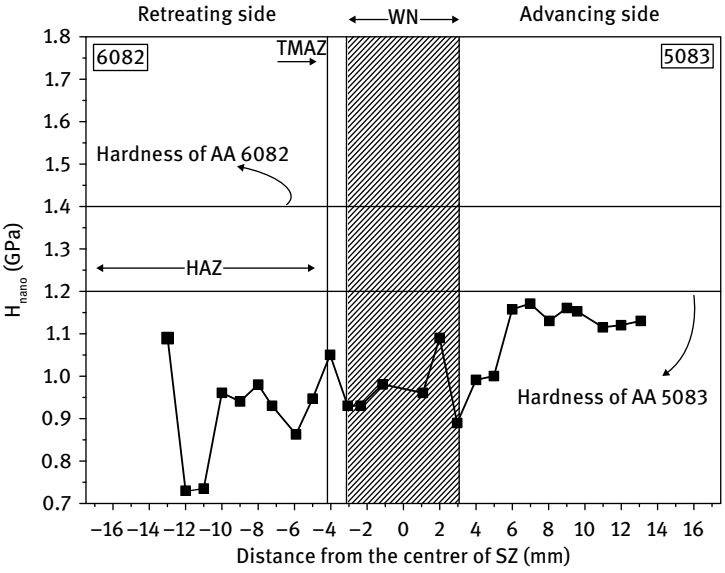

Fig. 2.24: Nanohardness distribution of the weld with the addition of CNTs obtained from nanoindentation experiments at 400 nm maximum penetration depth (2 mm under the surface).

Concerning the elastic modulus, local values measured by nanoindentation, are presented in Fig. 2.25. The welding process results in lower elastic modulus values at the side of 6082 HAZ. Comparing the elastic modulus distributions of the first and second

set of experiments (Figs. 2.16 and 2.25) the same trend is observed. In both cases: the values were found to increase in the WN up to 15 % compared to the elastic moduli of the parent materials (71,7 GPa) because of the presence of CNTs.

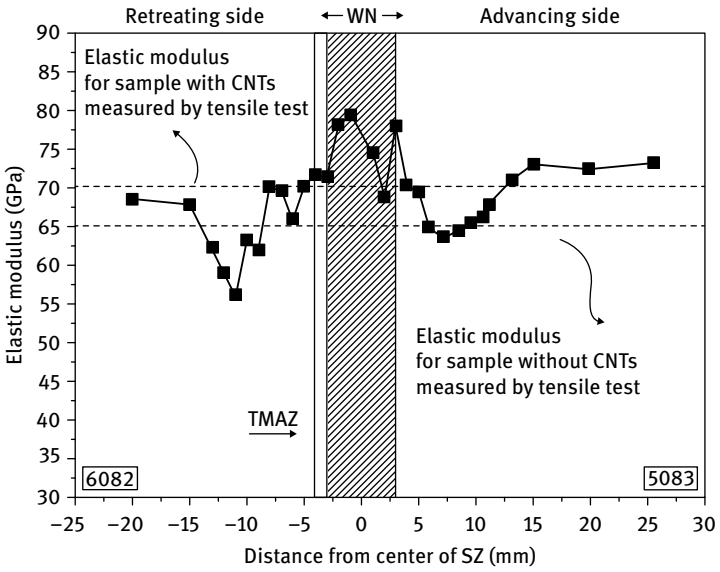

Fig. 2.25: Elastic modulus distribution of the weld with the addition of CNTs obtained from nanoindentation experiments at 400 nm maximum penetration depth (2 mm under the surface).

2.4 Conclusions

The aim of this work was to study the incorporation of carbon nanotubes in friction stir welding joints of the dissimilar aluminum alloys AA5083-H111 and AA6082-T6, as reinforcing fillers. This was accomplished by changing the tool rotational and travel speed as well as the number and the direction of FSW passes, which mainly affect the distribution of the nanoparticles in the weld nugget. Also, the present work focuses on the evaluation of the mechanical properties of the optimum joint by microhardness measurements as well as tensile and indentation methods.

- The best distribution of CNTs was achieved after the application of two passes of the opposite direction at 1500 RPM rotational speed. This led to the formation of a relatively uniform distribution of CNTs as shown from both optical and scanning electron microscopy.
- The hardness in the weld nugget in micro level was slightly improved (~7 %), whereas in nano level was slightly lower (~15 %) in comparison to the weld without reinforcing particles. This divergent behavior can be attributed to the

difference between the probed volume during microhardness measurement and nanoindentation.

- From the tensile tests, the elastic modulus and the yield stress of the reinforced specimens are very close, and within the error limits, to the equivalent of the unreinforced ones. Also the elastic modulus of the reinforced specimen (70 GPa) is similar to the equivalent of the parent materials (71.7 GPa for both the 5083-H111 as well as the 6082-T6). From the nanoindentation experiments, the elastic modulus of the weld nugget was found to increase up to 15 % compared to the elastic moduli of the parent materials because of the presence of CNTs. That shows a trend towards slight improvement of the elastic behavior of the stir zone of the material in nano level after the incorporation of CNTs.
- The ultimate tensile strength and the percentage of elongation could not be improved. The reinforced specimens failed in the weld nugget, while the unreinforced ones failed in the heat affected zone. This can be attributed to the geometry of the CNTs. The length of the CNTs (10 μm) is very large compared to their diameters (50 nm). This fact combined with their very high strength and the stirring action of the tool results in the formation of agglomerates. Consequently, the dispersion of CNTs in the metal matrix has a negative impact in the plastic behavior of the material, however this should be further investigated.

Acknowledgment

This research was supported by the EU FP7 Project "Enhancing structural efficiency through novel dissimilar material joining techniques" (SAFEJOINT) under Grant Agreement No. 310498. Financial support for author D. A. Dragatogiannis through a PhD scholarship granted by Research Committee of the National Technical University of Athens (NTUA) is gratefully acknowledged.

References

[1] Hashim J, Looney L, Hashmi MSJ. 1999. Metal matrix composites: production by the stir casting method, *J. Mater. Process Tech.* **92–93**, 1–7.

[2] Sukumaran K, Ravikumar KK, Pillai SGK, Rajan TPD, Ravi M, Pillai RM, et al. 2008. Studies on squeeze casting of Al 2124 alloy and 2124-10 % SiCp metal matrix composite, *Mat. Sci. Eng. A* **490**, 235–241.

[3] Scudino S, Liu G, Prashanth KG, Bartusch B, Surreddi KB, Murty BS, et al. 2009. Mechanical properties of Al-based metal matrix composites reinforced with Zr-based glassy particles produced by powder metallurgy, *Acta Mater***57**, 2029–2039.

[4] Pantelis D, Tissandier A, Manolatos P, Ponthiaux P. 1995. Formation of wear resistant Al-SiC surface composite by laser melt-particle injection process, *Mater. Sci. Tech.* **11**, 299–303.

[5] Dawes CJ, Thomas WM. 1996. Friction stir process welds aluminum alloys, *Weld. J.* **75**(3), 41–45.

[6] Mishra RS, Ma ZY. 2005. Friction stir welding and processing, *Mat. Sci. Eng. R.* **50**(1–2), 1–78.
[7] Jonckheere C, de Meester B, Denquin A, Simar A. 2013. Torque, temperature and hardening precipitation evolution in dissimilar friction stir welds between 6061-T6 and 2014-T6 aluminum alloys, *J. Mate.r Process Tech.* **213**(6), 826–837.
[8] Amancio-Filho ST, Sheikhi S, dos Santos JF, Bolfarini C. 2008. Preliminary study on the microstructure and mechanical properties of dissimilar friction stir welds in aircraft aluminum alloys 2024-T351 and 6056-T4, *J. Mater. Process Tech.* **206**(1–3), 132–142.
[9] Steuwer A, Peel MJ, Withers PJ. 2006. Dissimilar friction stir welds in AA5083–AA6082: The effect of process parameters on residual stress, *Mat. Sci. Eng. A* **441**(1–2), 187–196.
[10] Tanaka T, Morishige T, Hirata T. 2009. Comprehensive analysis of joint strength for dissimilar friction stir welds of mild steel to aluminum alloys, *Scripta Mater.* **61**(7), 756–759.
[11] Murr LE, Flores RD, Flores OV, McClure JC, Liu G, Brown D. 1998. Friction-stir welding: microstructural characterization, *Mater. Res. Innov.* **1**(4), 211–223.
[12] Murr LE, Li Y, Flores RD, Trillo EA, McClure JC. 1998. Intercalation vortices and related microstructural features in the friction stir welding of dissimilar metals, *Mater. Res. Innov.* **2**, 150–163.
[13] Cavaliere P, Nobile R, Panella FW, Squillance A. 2006. Mechanical and microstructural behavior of 2024-7075 aluminum alloy sheets joined by friction stir welding, *Int. J. Mach. Tool Manu.* **46**, 588–594.
[14] Kurt A, Uygur I, Cete E. 2011. Surface modification of aluminum by friction stir processing, *J. Mater. Process Tech.* **211**(3), 313–317.
[15] Uzun H. 2007. Friction stir welding of SiC particulate reinforced AA2124 aluminum alloy matrix composite, *Mater. Design* **28**(5), 1440–1446.
[16] Feng AH, Xiao BL, Ma ZY. 2008. Effect of microstructural evolution on mechanical properties of friction stir welded AA2009/SiCp composite, *Compos. Sci. Technol.* **68**(9), 2141–2148.
[17] Wang W, Shi QY, Liu P, Li HK, Li T. 2009. A novel way to produce bulk SiCp reinforced aluminum metal matrix composites by friction stir processing. *J Mater Process Tech* **209**(4), 2099–2103.
[18] Dolatkhah A, Golbabaei P, Besharati Givi MK, Molaiekiya F. 2012. Investigating effects of process parameters on microstructural and mechanical properties of Al5052/SiC metal matrix composite fabricated via friction stir processing, *Mater. Design* **37**, 458–464.
[19] Lee IS, Hsu CJ, Chen CF, Ho NJ, Kao PW. 2011. Particle-reinforced aluminum matrix composites produced from powder mixtures via friction stir processing, *Compos. Sci. Technol.* **71**(5), 693–698.
[20] Wang W, Shi Q, Liu P, Li H, Li T. 2009. A novel way to produce bulk SiCp reinforced aluminum metal matrix composites by friction stir processing, *J Mater Process Tech.* **209**(4), 2099–2103.
[21] Shafiei-Zarghani A, Kashani-Bozorg SF, Zarei-Hanzaki A. 2009. Microstructures and mechanical properties of Al/Al2O3 surface nano-composite layer produced by friction stir processing, *Mat. Sci. Eng. A* **500**(1–2), 84–91.
[22] Sathiskumar R, Murugan N, Dinaharan I, Vijay SJ. 2013. Characterization of boron carbide particulate reinforced in situ copper surface composites synthesized using friction stir processing, Mater. Charact. **84**, 16–27.
[23] Mostafapour Asl A, Khandani ST. 2013. Role of hybrid ratio in microstructural, mechanical and sliding wear properties of the Al5083/Graphitep/Al2O3p a surface hybrid nanocomposite fabricated via friction stir processing method, *Mat. Sci. Eng. A* **559**, 549–557.
[24] Qiang L, Liming K, Fencheng L, Chunping H, Li X. 213. Microstructure and mechanical property of multi-walled carbon nanotubes reinforced aluminum matrix composites fabricated by friction stir processing, Mater. Design **45**, 343–348.

[25] Lim DK, Shibayanagi T, Gerlich AP. 2009. Synthesis of multi-walled CNT reinforced aluminum alloy composite via friction stir processing, *Mat. Sci. Eng. A* **507**, 194–199.
[26] Sun YF, Fujii H. 2011. The effect of SiC particles on the microstructure and mechanical properties of friction stir welded pure copper joints, *Mat. Sci. Eng. A* **528**(16–17), 5470–5475.
[27] Ahn B-W, Choi D-H, Kim Y-H, Jung S-B. 2012. Fabrication of SiCp/AA5083 composite via friction stir welding, *T. Nonferr. Metal Soc.* **22**(3), 634–638.
[28] Bahrami M, Dehghani K, Kazem Besharati Givi M. 2014. A novel approach to develop aluminum matrix nano-composite employing friction stir welding technique, *Mater. Design* **53**, 217–225.
[29] Bahrami M, Kazem Besharati Givi M, Dehghani K, Parvin N. 2014. On the role of pin geometry in microstructure and mechanical properties of AA7075/SiC nano-composite fabricated by friction stir welding technique, *Mater Design* **53**, 519–527.
[30] Pantelis D, Karakizis P, Daniolos N, Charitidis K, Koumoulos E, Dragatogiannis D. 2015. Dissimilar friction stir welding of AA5083 with AA6082 reinforced with SiC particles, *Mater. Manuf. Process*, accepted manuscript.
[31] Charitidis C, Dragatogiannis D, Koumoulos E, Kartsonakis I. 2012. Residual stress and deformation mechanism of friction stir welded aluminum alloys by nanoindentation, *Mat. Sci. Eng. A* **540**, 226–234.
[32] Avettand-Fènoël MN, Simar A, Shabadi R, Taillard R, de Meester B. 2014. Characterization of Oxide Dispersion Strengthened Copper Based Materials Developed by Friction Stir Processing, *Mater. Design* **60**, 343–357.
[33] Ji SD, Shi QY, Zhang LG, Zou AL, Gao SS, Zan LV. 2012. Numerical simulation of material flow behavior of friction stir welding influenced by rotational tool geometry, *Comp. Mater. Sci.* **63**, 218–226.
[34] McNelley TR, Swaminathan TR, Su JQ. 2008. Recrystallization mechanisms during friction stir welding/processing of aluminum alloys, *Scripta Mater.* **58**(5), 349–354.
[35] Humphreys FJ, Hatherly M. 2004. *Recrystallization and related annealing phenomena*, 2nd ed., Oxford, UK, Elsevier.
[36] Moreira PMGP, Santo sT, Tavares SMO, Richter-Trummer V, Vilaça P, de Castro PMST. 2009. Mechanical and metallurgical characterization of friction stir welding joints of AA6061-T6 with AA6082-T6, *Mater. Design* **30**, 180–187.
[37] Oliver W, Pharr G. 1992. An improved technique for determining hardness and elastic modulus using load and displacement sensing indentation experiments, *J. Mater. Res.* **7**(06), 1564–1583.
[38] Sneddon I. 1948. Boussinesq's problem for a rigid cone, *Proc. Cambridge Philos. Soc.* **44**, 492–507.
[39] King RB. 1987. Elastic Analysis of Some Punch Problems for a Layered Medium, *Int. J. Solids Structures* **23**, 1657–1664.
[40] Hangen UD, Stauffer DD, Syed Asif SA. 2014. Resolution limits of nanoindentation testing, in A. Tiwari (ed.), *Nanomechanical Analysis of High Performance Materials*, Springer.

M.F. Montemor

3 Corrosion issues in joining lightweight materials: A review of the latest achievements

Abstract: Multimaterials assemblies and, in particular, assemblies made of lightweight components are of utmost relevance in many technical applications. These assemblies include multimetal, metal-polymer, metal-adhesive, and metal-composites combinations, among others. Presently, the transportation sector is looking for lighter materials that allow for reducing fuel consumption and the environmental footprint. Aluminum and magnesium alloys, as well as composites and polymers, are considered strategic for such purposes, and their joining in metal-metal or hybrid assemblies has been explored to develop lightweight components. These multimaterial assemblies are often exposed to aggressive environments in which moisture and aggressive species are present. Under these conditions corrosion phenomena are a major source of material failures. Depending on the nature of the metals and nonmetals and of the joining process, the mechanism and extent of corrosion can vary significantly. Thus, it is essential to understand the impact of corrosion in joined materials and to know which counter-measures can be adopted to mitigate corrosion events in the system of concern.

This chapter aims at reviewing the latest results of studies focused in corrosion issues in the joining of lightweight materials. It describes the most common corrosion phenomena observed in joined materials, and it emphasizes corrosion issues in assemblies that combine different metals and that combine metals with nonmetals. Moreover, it overviews the state-of-the-art in corrosion protection strategies that can be applied and, finally, it overlooks the future trends.

3.1 Introduction

Joining is a technological process, which places together different materials to form a single unit. The goal is to create a product displaying properties and performance unattainable in the individual materials. Joining technology is based in three main processes: mechanical joining that makes use of mechanical forces, adhesive bonding that is based on chemical forces, and welding, resulting from physical forces.

Mechanical joining relies on mechanical forces to join distinct materials. Normally this process does not involve chemical reactions or atomic interactions. Adhesive bonding makes use of foreign materials which promote the bonding between the distinct materials that need to be put in place. This additional material is the adhesive. Welding makes use of a combination of heat and, when required, pressure and can be classified as fusion or nonfusion type.

Joining of dissimilar materials is of extreme relevance in many applications. The process requires suitable matches concerning the chemical, physical, and mechanical properties between the materials placed together. When these properties do not have a closer match, the process can be completed by using joining agents such as adhesives or rubbers. In all the joining routines an interface is formed and its presence creates areas susceptible to corrosion.

Ideally, the joining processes should not affect the mechanical properties of the materials involved and should not create physical discontinuities, chemical modifications, or microstructural changes in the materials being joined. Regrettably, despite many advances, the reality is that the joining methods do adversely affect the local properties of the materials. When metallic materials are concerned, these changes may affect the electrochemical activity of the metals and, in the presence of moisture and aggressive agents, corrosion activity becomes a major problem. Various corrosion phenomena can be observed, depending upon the nature of the joined materials and of the joint, composition of the environment and presence of mechanical stresses.

Presently, two of the most important lightweight metals are aluminum alloys and magnesium alloys. The electrochemical behavior of these materials is very distinct, as is its corrosion susceptibility. Research on corrosion issues in joining lightweight materials has been evolving very fast, and the most recent trends are overviewed in this chapter.

3.2 General aspects of corrosion in joints

Aluminum and magnesium alloys present a very favorable weight-to-strength ratio which allows decreasing the weight of the components. Joined assemblies may include different aluminum alloys, different magnesium alloys, steel combined with magnesium alloys, steel combined with aluminum alloys, and composites combined either with aluminum alloys or magnesium alloys. Since both magnesium and aluminum alloys are very susceptible to corrosion, it is important to characterize the possible corrosion mechanisms that may arise when these materials are considered. Some of the most relevant features related to the corrosion processes commonly found in aluminum and magnesium alloys are summarized below.

The corrosion activity of magnesium alloys is governed by some well-known key steps: (i) magnesium (or its alloys) are typically covered by a protective surface oxide/hydroxide; (ii) In the presence of oxygen and moisture, the oxide film is not protective enough, magnesium dissolves, and the process is accompanied by intense hydrogen release; (iii) magnesium is characterized by a negative free-corrosion potential, and even more negative pitting potential in aggressive solutions such as NaCl, making it very susceptible to localized corrosion attack. The high reactivity of magnesium and the low protectiveness of the oxide layer are responsible for the low resistance to localized corrosion attack. The lateral and in-depth spread of the corrosion process

leads to undermining and falling off of parts of the attacked material. In Mg alloys, the local differences in composition and microstructure also promote local galvanic corrosion cells which spread, leading to identical phenomena. Addition of some alloying elements such as aluminum, zirconium, or rare-earths can improve the corrosion resistance of magnesium alloys. Depending on the composition and microstructure of the magnesium alloys, the corrosion processes can be slowed down and some particularities may arise in what concerns the corrosion-governing mechanisms.

Aluminum and its alloys are characterized by the presence of a stable and highly protective thin oxide film that keeps the material in a passive state in many environments. However, this oxide film always presents some defects and flaws which create fragile areas that can be attacked in the presence of aggressive ions (e.g. chlorides). The local dissolution of the protective aluminum layer originates a pitting attack. The diameter and the depth of the pitting depends on the alloy composition, the local pH, and presence of aggressive species. Aluminum and its alloys are very susceptible to pitting corrosion in near neutral pH, which is found in many environments. The pitting process is typically characterized by two stages: (1) pitting onset, which involves adsorption and attack of the oxide layer by chloride ions. Eventually during this stage the oxide may repassivate and the pitting process does not enters the second stage; (2) pit growth, characterized by intense aluminum (or alloying elements) dissolution and precipitation of corrosion products such as $Al(OH)_3$,

In Al alloys, the presence of alloying elements (such as Mg, Mn, Cu, Fe, Si, Li, …) induces the formation of a multiplicity of intermetallic particles, of distinct composition, and different electrochemical behavior, compared to the pure Al matrix. The presence of redox-active intermetallic creates preferential sites for localized corrosion onset. In general, corrosion of Al and Al alloys is a localized process. Other forms of corrosion in aluminum alloys include transgranular dissolution (the corrosion affects the various metallurgical features, and it is not selective), intergranular corrosion (the corrosion propagates in preferential paths), stress-induced corrosion, galvanic corrosion, and exfoliation corrosion.

The corrosion processes which may occur in the individual Mg and Al alloys depend on several variables, and are extremely complex. Therefore, its joining is a challenge with regard to corrosion issues. In addition to the specificities of each single material there is need to consider the joining area that may be considered as a "new" material, bringing additional peculiarities and eventually new forms of corrosion.

The joining of two metals or a metal and a composite is characterized by the presence of a joint that places together the two individual parts. When two dissimilar metals are placed into contact there is formation of a galvanic cell. In the presence of aggressive electrolytes, galvanic cells induce dissolution of the less noble metal (or phase) in the assembly. This form of corrosion is known as galvanic corrosion. On the other hand some joining process creates local changes, including modification of microstructures and formation of new phases that may form microgalvanic corrosion cells at the microstructural level.

The presence of stress (even if residual) on and around the joint may, additionally provoke stress corrosion cracking phenomena. This form of corrosion requires the presence of stress, a corrosive media, and a corrosion-susceptible microstructure. Corrosion normally starts at the points of stress concentration, leading to nucleation of cracks. When the cracks develop, there is formation of an anodic tip, and the corrosion process propagates by branching. The presence of stress in high strength materials may promote hydrogen embrittlement and hydrogen-induced cracking.

Joints and welded areas are quite susceptible to pitting corrosion. Pitting corrosion always starts in defects or "weak points" arising from microstructural features existing in a passive layer. The pit works like an anode, and it is supported by a larger cathodic area. The corrosion process inside the pitting is accompanied by strong acidification, and in the presence of chloride ions an autocatalytic process may develop, resulting in catastrophic failure of the material.

Crevice corrosion is also a phenomenon which can be observed in joined parts. The joining process may create defects, microfissures, or occluded zones that can result in the formation of crevices in which localized concentration cells are formed. Due to fast consumption of oxygen, the crevice becomes anodic and the surrounding metal cathodic. The process may involve strong acidifications, and the effect can be catastrophic in the presence of aggressive ions such as chlorides.

The differences in the chemical composition of the metals in the joined assembly can also be sensitive to high temperature-induced corrosion. The different chemical compositions across the interfaces and the microstructural changes can result in selective oxidation when the assembly is exposed to a high-temperature environment. Thus, the interfacial zone is very susceptible to high-temperature corrosion phenomena.

Corrosion effects on joints can be minimized by cleaning the surfaces to be joined, applying the proper materials (fillers and adhesives), and by applying suitable pre- and post-joining treatments. Galvanic corrosion effects can be minimized by selecting appropriate fasteners and materials which are chemically and electrochemically compatible. It can also be prevented by adjusting the weld metal in such a way that it can provide cathodic protection of the base metal which is more susceptible to galvanic dissolution. Corrosion prevention can also be achieved by applying coatings or surface finishers.

3.3 Corrosion in lightweight metallic joints

The transportation industry, mainly the automotive industry and aeronautics, is one of the most dynamic sectors with regard to envisaging of new lightweight material assemblies. The main target is to decrease the vehicle weight, reducing fuel consumption and CO_2 emission, while optimizing the vehicle design and its overall performance. Presently, steel, aluminum, magnesium, and composites are the most often consid-

ered materials for these targets. These materials require a variety of joining technologies, which have been evolving and optimized. However, corrosion phenomena are still a major concern, and intense research activity has been carried out in this specific field.

3.3.1 Steel and lightweight metals

N. Le Bozec at al. [1] studied the corrosion behavior of various automotive joined assemblies using standard corrosion tests, such as the N-VDA test. The conventional steel materials tested included various carbon steel grades, hot dip galvanized steel, and electrogalvanized steel. Lightweight materials tested were the magnesium alloy AM 50 and various aluminum alloys. The joining techniques included adhesive joining with epoxy, clinching, spot welding, laser welding, and arc welding. The loss of mechanical properties was correlated to the extent of corrosion degradation. It was demonstrated that the depth of attack was greatly increased during exposure to the VDA test. The joint strength was evaluated, and it was found that clinching did not affect this parameter. On the other hand, adhesives showed increased loss of strength during the VDA test. The adhesives failed because of corrosion propagation at the interface metal-adhesive and the subsequently generated stresses. It was demonstrated that the assemblies made of steel and zinc-coated steel presented improved mechanical properties. In another work [2], the same authors demonstrated that the corrosion in joined materials, particularly in adhesive-bonded interfaces, was potentiated by the simultaneously application of fatigue loading during samples exposure to the cyclic tests. It was also observed that weld-bonded and spot-welded samples did not evidence failure during the combined fatigue-corrosion tests.

Automotive grade galvanized steel and the aluminum alloy 6016 were joined by the laser keyhole welding technique. The microstructure of the joints formed in the process was investigated in detail. The results showed the presence of a dendritic eutectic structure and the presence of equi-axis crystals at the centre of the welded area. The results also revealed an interfacial layer formed with galvanized steel, with thicknesses ranging from 1.5 to 13 μm [3]. This layer was composed of three distinct phases which were characterized by different mechanical properties.

The corrosion behavior of laser-beam joined steel and aluminum was investigated in salt spray tests. Hot dip galvanized steel and AA6016 were joined in the presence of two different fillers [4]. The results showed that the fusion zone was the one most susceptible to corrosion, and that the extent of corrosion damage was also dependent upon the cathodic response of the surrounding metal, namely steel. The welding process produced a Zn-rich runout area (Fig. 3.1(a)), which revealed itself to be the one most susceptible to corrosion. The Zn-Al microstructure in the run presented an anodic behavior and therefore was the first one to dissolve. The corrosion processes induced

internal tensions and formation of cracks which affected the durability of the assembly (Fig. 3.1(b)).

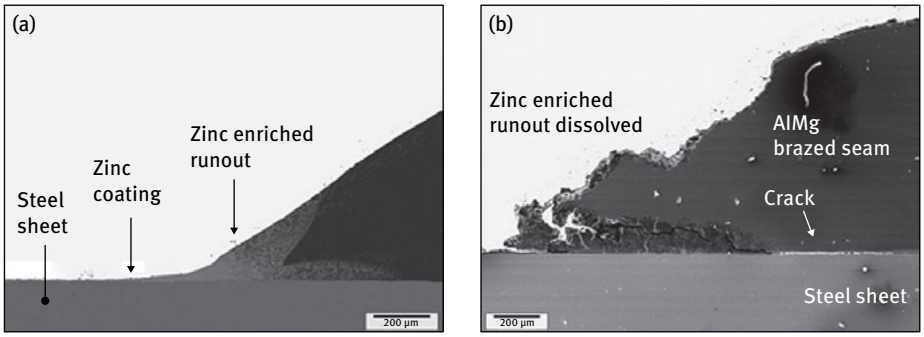

Fig. 3.1: Cross sections obtained by SEM on the aluminum based filler (AlMg6Mn) material joint: (a) Before corrosion test and (b) after 192 h in salt spray r. The zinc-enriched run out dissolves first forming a crevice between brazed seam and steel sheet. From [4]

Galvanized steel and aluminum are dissimilar materials, and their welding can be performed in different ways. Laser welding is a very promising method in many industrial applications. However, when these materials are joined, there are some risks, such as the formation of pores and of brittle intermetallics. Zinc possesses a boiling point much lower than that of aluminum and, consequently, iron and zinc vaporization may occur. The quality of the welded materials and the corrosion susceptibility depends upon the laser-processing parameters. This effect was investigated by H.-C. Chen et al. [5], who found that the corrosion resistance of the joined parts was improved when argon gas was used as shielding gas. However, the shear strength was improved by using N_2 gas. Laser joining of Al-plated steel and aluminum were investigated recently [6]. Different parameters such as the laser intensity and the addition of fillers were considered. The results showed that the addition of carbon and tungsten to the steel could reduce the formation of intermetallic particles.

Adhesive bonding has several advantages, and this technique is often used in the preparation of assemblies for automotive applications. Moreover, it can be easily applied over coated metals. When applied over coated metals, the properties of the coating affect the bond strength and must also be considered. Studies were performed using various coated samples. The results of lap-shear and butt-joint tests showed that failures were more prone to occur at the interface metal coating and inside the coating. The work demonstrated that softened adhesives were able to reduce peak stresses [7].

3.3.2 Lightweight metals

Mg and Al alloys are among the most strategic alloys for developing lighter materials for the automotive and aeronautic sectors.

Riveting, i.e. self-piercing riveting, is a plastic-joining process that can be applied to join thin metallic sheets. It does not require drilling and is a cold process. However, one of the major limitations to its widespread use in automotive and aeronautics has been the risk of localized corrosion damage. The cold forming processes may induce local stresses, which potentiate stress corrosion cracking. Other surface heterogeneities may result in the formation of micro-occluded areas and consequently crevice corrosion. AA 6082 was joined by this process, and its susceptibility to corrosion was investigated by L. Calabrese et al. [8]. The relation between the geometry, the mechanical resistance, and the corrosion behavior was evaluated. The riveting process induced local stress that increased the probability of crack formation and the corrosion susceptibility. The local corrosion activity was associated with crevice corrosion and pitting corrosion, and decreased the performance of the joined parts and the resistance of the assembly during the pull-off tests.

The corrosion behavior of welded Mg parts (Mg alloy AZ61A) has been carried out using various techniques such as friction stir welding (FSW). Given the high susceptibility of Mg alloys to chloride-induced corrosion, the effect of pH, chloride concentration, and immersion time was investigated in detail by A. Dhanapal et al. [9]. The results showed that the corrosion rates decreased in alkaline pH conditions and increased in more neutral/acidic pH ranges in the presence of chloride ions. The formation of a hydroxide layer over the welded joints created a resistive pathway that slowed down corrosion damage over time.

The FSW process results in the formation of different zones that present different susceptibility to corrosion. These zones are: (i) the base metal; (ii) the weld nugget; (iii) the heat-affected region; (iv) thermo- and mechanically-affected areas. The corrosion susceptibility of stir welded joints on AlMgSiCu alloys (6xxx series) as well as the microstructure and microhardness were investigated in detail by P. Dong et al. [10]. The work demonstrated that there was a correlation between microstructure and intergranular corrosion susceptibility. The fine precipitates resulted in higher hardness, and the coarser precipitates increased softening. Coarsening of the intergranular precipitates decreased the susceptibility to intergranular corrosion, but seemed to promote pitting corrosion in the zones affected by heating. The formation of microgalvanic cells occurred at the grain boundaries of the precipitates, which displayed either a more active or a more noble character, compared to the aluminum matrix. The corrosion resistance was increased in the areas showing more homogeneous microstructure [10].

The way corrosion develops in the different zones formed in the FSW process was investigated by several authors, producing some controversial statements. The nugget zones and the heat-affected zones have been identified as the most susceptible to cor-

rosion onset [11]. However, other work carried out on FSW AA7108 proposed that the thermomechanically affected zone was more susceptible to corrosion development [12]. The corrosion process was associated with intergranular dissolution due to the nonuniform distribution of $MgZn_2$ intermetallics across the affected zone.

The corrosion behavior of FSW welded joints was investigated in various alloys such as 2219-T87 plates. The thermomechanically affected zone revealed the presence of Al_2Cu intermetallics, and it was found that the welded areas exhibited identical environmentally-assisted cracking corrosion susceptibility. Moreover, the work reported that the joints seemed to be more resistant to corrosion then the unaffected zones. The effect was attributed to the coarsening of the Al_2Cu precipitates [13]. On the other hand, polarization curves and electrochemical impedance measurements obtained on FSW joint in AA 2024 panels revealed identical pitting tendency of the heat-affected zone and thermomechanically affected zones.

J. Kang el al. [14] also investigated the pitting susceptibility of FSW-joined AA2024-T3. The corrosion susceptibility was associated with the presence of Al-Cu-Fe-Mn-Si and Al-Cu-Mg intermetallic particles. The particles induced the dissolution of the adjacent aluminum matrix. The zones more susceptible to corrosion were the S-Phase (Al-Cu-Mg). The corrosion activity was influenced by the parameters used in the FSW process. For example it was demonstrated that the nugget zone was more susceptible to anodic dissolution under low rotation speeds, whereas the heat-affect zone became more susceptible to corrosion at higher speeds. The propagation of intergranular attack occurred at the grain boundaries as result of their sensitization. The nugget worked as cathode and enhanced cathodic reactivity that protected this area from corrosion [15].

The susceptibility to intergranular corrosion of the welded areas in AA2024 was investigated by Bousquet et al. [16]. The corrosion process was investigated in the various zones formed after FSW. Thus, in the bare alloy, corrosion of some grain boundaries was observed, and the corrosion process (mainly pitting corrosion) was attributed to the preferential dissolution of Cu-containing precipitates. On the heat-affected zones, the pitting corrosion activity was similar to that observed in the bare material. This was explained under consideration that the composition, size, distribution and density of the intermetallics were quite similar to those observed on the base alloy. However, when immersed in aggressive solutions, the potential gradients across the heat-treated zone induced galvanic dissolution, with the weld behaving anodically and the bare metal cathodically. Closer to the thermomechanical affected zone, the processes changed. Pitting attack in the coarser intermetallics was observed, but the intergranular corrosion attack became more pronounced with time. The most sensitive area was the one in the transition zone, between both affected zones. It was more susceptible to both pitting attack and intergranular corrosion [16].

The corrosion resistance of FSW in AA7449-T7951 joints could be improved by laser melting. Such effect was reported by Padovani et al. [17]. Without the laser treatment, the heat-affected zone revealed several pits, about 100 μm deep. The treatment with

the laser created a homogeneous layer, which dissolved the intermetallic particles within a solid solution. The corrosion damage at the nugget area was not significantly affected by the laser treatment; however in the heat-affected zones, the pits formed were not as deep as the ones observed in the untreated zone. The corrosion potential breakdown was assessed by d.c. potentiodynamic polarization using the micro capillary cell. The findings showed that the laser treatment practically did not affect that electrochemical parameter. The laser-treated zone exhibited lower open circuit potential values, which seemed responsible for some sacrificial cathodic protection, concentrating the corrosion in the laser affected zone, and hindering its propagation to the unaffected areas (Fig. 3.2). Corrosion propagation caused partial delamination of the treated zone, an effect that could be a serious drawback with regard to the laser melting treatment of welded zones.

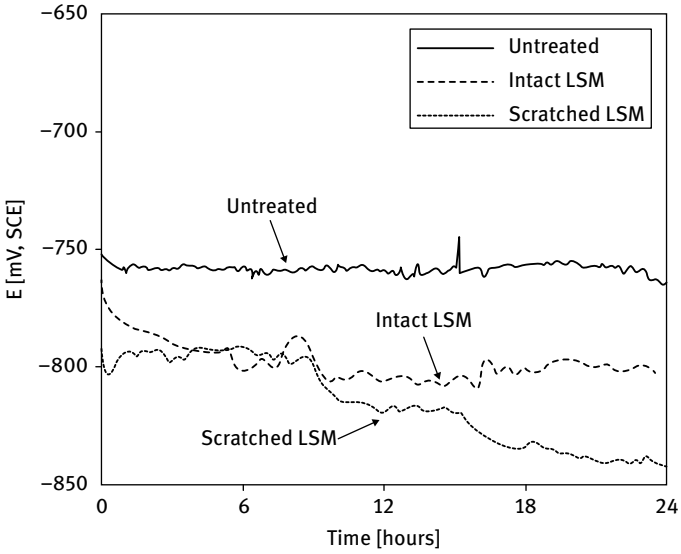

Fig. 3.2: Open circuit potential evolution of untreated, intact laser-treated and scratched laser-treated parent material specimens measured during immersion in 0.1 M NaCl. From [17].

Various surface treatments such as laser and shot peening were performed on FSW 7075 alloys to increase the resistance against stress corrosion cracking susceptibility. It is known that the weld zones are subjected to different stresses, which are more intense in the nugget zone, as demonstrated elsewhere [18]. The welded samples were immersed in 3.5 % NaCl solutions for 2 months. The peened samples did not reveal pitting corrosion or intergranular corrosion attack. The unpenned surfaces showed severe pitting attack, but this form of corrosion was avoided in the laser treated surface. For the tested period the effect of stress corrosion cracking was not evident.

Microstructure, impurities, presence of residual stress, formation of intermetallics, and corrosion onset are factors that determine the lifetime of joined components. These issues were investigated in FSW joints formed on the Al-Zn-Mg alloys used in aeronautic applications [19]. In the Al-Zn-Mg alloy the thermomechanically affected zone was richer in Fe and Si, containing intermetallics that are more cathodic then the surrounding Al matrix. This potential difference, which attained 400 mV, induced microgalvanic corrosion activity. Thus, the localized corrosion process propagated as intergranular corrosion, resulting in intergranular cracking. However, in the Al-Zn-Mg-0.10Sc-0.10Zr alloy, there was formation of secondary $Al_3Sc_xZr_{1-x}$ particles that promoted the formation of more protective layers, decreasing the anodic dissolution and therefore increasing the corrosion resistance of this alloy.

A correlation between the microstructure and the corrosion onset susceptibility on Al-Cu joints was recently reported [20]. The study revealed that the microstructure near the interface showed the presence of $CuAl_2$ intermetallic particles and the α-Al phase. In the transition zone it was possible to postulate the presence of a solid solution composed of Cu-Al-Zn. The Volta potential of the surface was studied by atomic force microscopy (AFM) coupled to scanning Kelvin probe force measurements (SKPFM). The measurements showed that the initiation of the corrosion processes (pitting) occurred on areas showing the largest differences in Volta potential. These are, for example, the interface of Cu particles and Al-rich phases. Some evidence of pitting was also found inside the Al-rich phase (in the vicinity of the intermetallic particles). On the other hand, the presence of both Al and Zn in the interfacial region could promote the formation of protective products in the transition zones, delaying the corrosion propagation at initial stages.

The galvanic corrosion effects on polished FSW joints formed on AZ31 Mg alloys and AA2024 were investigated by C. Liu et al. [21]. Water-based polishing routes created surfaces that were more prone to galvanic corrosion attack compared to water-free polishing solutions. The corrosion onset was mainly located on the AZ31 region adjacent to the AA2024, where the area anode to cathode was lower. The accumulation of porous corrosion products, mainly magnesium hydroxides, led a decrease of the mechanical properties. No relevant corrosion was observed on the base alloys.

3.3.3 Coatings to minimize corrosion in multimetal assemblies

The corrosion resistance of welded parts can be improved by the presence of coatings. A micro-arc oxidation coating was deposited over AA7075, and its corrosion resistance was assessed by electrochemical techniques. The results revealed that the presence of a Na_2SiO_3 coating could considerably improve the corrosion resistance of the welded parts [22].

A protective ceramic coating was produced by plasma electrolytic oxidation (PEO) on the friction stir welded joints of the magnesium alloy AZ31 B. This coating was

composed of an inner protective layer and an outer porous layer. It was demonstrated that the morphology of the PEO coating was not affected by the microstructure of the welded Mg alloy. The corrosion behavior was studied by means of electrochemical impedance spectroscopy and d.c. polarization on samples exposed to 3.5 wt.% NaCl. The results demonstrated that the heat-affected zone was more prone to corrosion, whereas the stir zone with a finer grain structure was more resistant. Overall, the presence of the PEO coating could protect the stir welded alloy AZ31 B [23]. The effect of grain size on identical alloys was investigated by J.R. Kish et al. by combining different electrochemical techniques, including localized electrochemical techniques. d.c. Potentiodynamic studies revealed identical anodic kinetics and some differences in the cathodic kinetics. The extent and kinetics of filiform corrosion was affected by the grain size. Thus, the initiation of the filament occurred in the coarser-grained areas. On the other hand, the grain size did not affect the kinetics of corrosion propagation from the bare metal (coarser grains) across the stir zones, where the grain was more refined [24].

Thermal sprayed coatings can also offer protection of joined aluminum and magnesium plates in a salt spray corrosion test. However failure was still observed after some time of exposure in the salt spray test [25].

Cold spraying could be used to deposit protective coatings over the FSW joints in AA alloys as proposed by Li et al. [26] The pure Al coating with thicknesses between 90 and 100 μm was adherent to the joined surfaces, free of cracks, and showed only little evidence of some outer pores. The presence of the coating contributed for increased hardness and offered corrosion protection of the joined surfaces. Samples without coating evidenced serious exfoliation and pitting corrosion, especially in the thermomechanically affected zone. The pits grew and deepened with time and became interconnected, leading to intergranular corrosion paths that finally resulted in exfoliation of the material. However this process was absent on the coated samples. Although corrosion was also observed in the Al coating, the process was not severe. Thus, in the coated samples, corrosion started in the interfaces of the deposited particles. Then corrosion caused a decrease of the coating thickness, but the joints were protected. It can be inferred that, if properly designed and applied, coatings may significantly delay the corrosion attack in joints.

3.4 Corrosion in metal-nonmetal joints

The advantages of using metallic and nonmetallic materials, combining properties unattainable by using any of the single materials, can be achieved by joining dissimilar materials in a hybrid assembly. These hybrid combinations are foreseen for applications requiring the decrease of the weight of the components and, presently, are used in a wide array of technical applications as structural components. The durability of these structures is very much impacted by the durability of the interfaces within

the hybrid assembly. The challenge of placing together distinct materials like metals, ceramics, composites, plastics, and polymers that display different chemical, physical, and mechanical properties has not been solved yet, and many solutions are being proposed. Corrosion is once more a major source of failure.

Fiber-reinforced composites (FRP), because of their stiffness, decreased weight mechanical properties, and corrosion resistance, are used in several engineering applications. The joint between metals and FRPs is sensitive to failure, and the main causes of failure that have been identified include corrosion, delamination and/or debonding, tensile failure, crack development, and bearing. Since most of the reinforced composites contain carbon fibers and other conductive fillers, when in contact with the metal there is an increased tendency for galvanic corrosion. The process can be accelerated by the presence of moisture and oxygen and aggressive species such as chloride ions. Due to the more noble character, normally the composite works as a cathode where oxygen reduction takes place. On the other hand, the metallic side acts as an anode, and the metal dissolves. The mitigation of these detrimental events requires profound development of new joining materials, such as adhesives and rubbers, and improvement of the mechanical properties, adhesion behavior, and strategies to increase the corrosion resistance of the composites and metals.

E. Sarlin et al. [27] investigated the adhesion performance of rubber joined stainless steel parts and glass fiber reinforced composites. This assembly aimed at combining the good mechanical properties and the high corrosion resistance of steel with the flexibility and good adhesion of rubber and decreased weight of the composite part. Transmission electron microscopy experiments showed that close and high quality contact was obtained in the joined parts. Although neither corrosion issues nor parts durability were assessed, the use of rubbers demonstrated increased adhesion in the bonded surfaces. It was also shown that none of the rubbers used was degraded. The resistance against environmental ageing effects (hot, hot/moisture, and moisture) was also investigated by FTIR and TGA in the same type of materials [28]. After exposure to the testing environments, samples showed good adhesion, and the performance of the material suggested that the behavior was independent of the surface treatment of the steel prior to joining. This route suggests that corrosion impact can be minimized.

Nanotechnology and nanomaterials have been contributing to advances in the materials properties, and this has been considered to improve the corrosion resistance of joined parts. For example conductive carbon fillers, such as carbon nanotubes, present good conductivity, thermal and electronic properties in addition to increased mechanical resistance and have been explored as additives to the epoxy matrix of the composites. Even in small amounts, the addition of carbon nanotubes to the matrix may have an important benefit on several properties. Carbon nanotubes also possess an increased interfacial surface area that enhances the mechanical behavior of the composite or of adhesives used in joints. Therefore there is an increased interest in understanding the corrosion behavior of joints when carbon nanotubes are used as fillers. Concerning corrosion related processes the following issues have been ad-

dressed: (i) Does the addition of carbon nanotubes to FRPs increase the susceptibility to galvanic corrosion between the modified composite and the metallic alloy? (ii) Does the presence of carbon nanotubes delay the ingress of aggressive electrolyte to corrosion-susceptible areas? (iii) Do carbon nanotubes contribute to enhanced adhesion and reduction of delamination effects in adhesive joints? Various studies have addressed these issues. For example, R. Ireland et al. [29] demonstrated that the addition of conductive fillers to the composite material promoted the formation of galvanic cells when the composite was placed into contact with the metallic part. Adhesives modified with carbon nanotubes were applied on the AA 2024 and the galvanic corrosion effects were studied in detail [30]. The work demonstrated that the presence of carbon could retard (and in some cases inhibit) electrolyte uptake through the interface. The effect was explained, under consideration that the presence of nanotubes limited microcracking and water bonding. The extent of the galvanic coupling effect was dependent upon the percolation threshold of nanotubes in the modified epoxy-based matrix. It was also found that the addition of nanotubes to the adhesive decreased the corrosion current densities and also slightly nobler potential values. One of the most important effects of the presence of nanotubes was related to adhesion enhancement; however, the effect was more pronounced when the alloy was previously anodized [30].

The addition of carbon nanotubes to metallic composites such as Mg-based composites has been reported as a possible strategy to improve mechanical properties of the material. However, in this case, the carbon filler was nobler then the magnesium alloy, and galvanic corrosion susceptibility was increased. This can be minimized by adding Al to the Mg-nanotubes composite. In this case the resulting composite (nanotubes containing alloy) should present increased corrosion resistance. This effect was observed for AZ61 composites modified with carbon nanotubes [31]. It was possible to prepare a material in which the aluminum atoms, in solid solution, coated the carbon nanoparticles. This preferential distribution resulted in a decrease of the galvanic coupling effect, thus reducing the corrosion susceptibility of the Mg matrix, and retarding the corrosion effects of this material compared to magnesium composites.

The galvanic corrosion effects between the AA7075 and glass fiber reinforced composites (GFRP) obtained from an epoxy matrix modified with carbon nanotubes were investigated in samples exposed to different environments characterized by high humidity and/or the presence of NaCl. The two materials were placed into direct contact and the ratio composite to aluminum alloy was also investigated. Electrochemical measurements confirmed that the presence of carbon nanotubes increased the galvanic corrosion effects. The galvanic corrosion mechanism was investigated in detail in galvanic couples made of a carbon fiber reinforced epoxy matrix and *two different aluminum alloys (AA 7075 and AA1050)*. The corrosion mechanism was detailed in the presence of NaCl solutions with and without adding copper sulphates [32]. The corrosion processes was examined by d.c. potentiodynamic polarization. The results revealed very interesting findings: (i) the cathodic current was mainly originated in exposed fibers; (ii) the presence of copper led to a significant increase of the cathodic

current density due to Cu precipitation over the exposed fibers; (iii) the galvanic current density was higher for the AA1050 compared with the AA7075. This behavior was justified by the presence of an increased density of cathodic areas in the AA7075 compared with tree AA1050.

The galvanic corrosion of rivet joints in a CFRP-aluminum alloy (Aw 6060) joint was examined in the presence of chloride ions by M. Mandel et al. [33, 34]. The corrosion studies were carried out by exposing the material to a 5 % NaCl solution and revealed that anodic activity occurred in the metallic side, in direct contact with the GFRP. Potentiodynamic polarization measurements showed the presence of a passive and a transpassive region. The pitting potential was determined as well as the critical potential difference for pitting corrosion that was approximately 100 mV. The electrochemical studies were combined by numerical simulations in which various aspects such as joint geometry were considered. The results showed that the zone sensitive to pitting attack was extended for 1.35 cm over the aluminum alloy. The pitting density decreased as the distance from the joint was increased. A cyclic VDA test [34] allowed identification of three stages of pitting corrosion development: in the first stage the pitting process was initiated at the aluminum alloy, being characterized by little pit volume change; in the second stage there was a significant pit growth; in the last stage the pitting growth was inhibited by the accumulation of corrosion products.

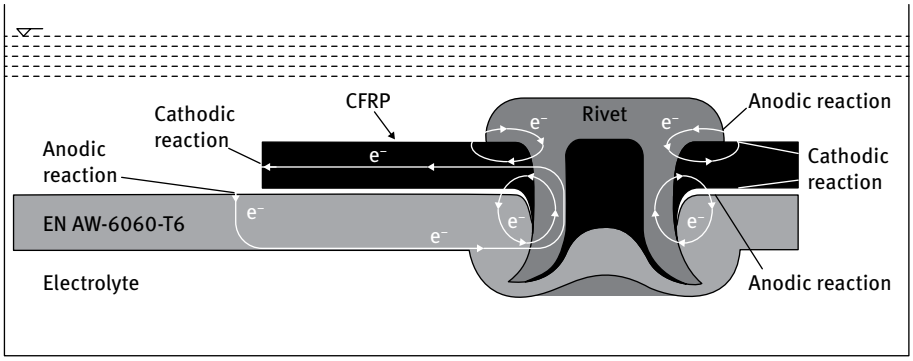

Fig. 3.3: Schematic view of a section in which the corrosion susceptible areas are marked. This is a rivet joint between an aluminum alloy (EN AW-6060-T8) and the GFRP component. Adapted from [33].

3.4.1 Coatings to minimize corrosion in hybrid assemblies

Despite the relevance of new coatings for protection of joints for metallic and nonmetallic materials, there are still very few works focusing on this specific issue. The galvanic effects between the GFRP and the metallic parts can be reduced by the use of corrosion inhibitors and/or coatings. This protective route was recently proposed in [35]. This work investigated the cooperative behavior of two different corrosion in-

hibitors: cerium nitrate, a well-known cathodic inhibitor, and benzotriazole known as an anodic/film-forming inhibitor. Both inhibitors were stored in ion exchange clays: layered double hydroxides (LDHs) and bentonites. LDHs are anion exchangers, being able to deliver an interleaved ion while capturing chlorides and hydroxyl ions; bentonites are cation exchangers and capture metallic ions. The modified pigments were added into an epoxy coating that was used to protect the GFRP-AA 2024 assembly. The coating was artificially damaged, and the corrosion inhibition processes was monitored using the scanning vibrating electrode technique (SVET). The results showed the cooperative inhibition mechanism of cerium ions, released from the bentonites and BTA released from the LDH particles. The bentonites were able to exchange the entrapped cerium cations with Al or Cu cations formed during the anodic dissolution of the S-phase present in the AA2024. The released cerium ions reacted with the hydroxyl ions formed during the cathodic reaction, leading to the deposition of an insoluble layer of cerium hydroxides that blocked the cathodic sites formed on the galvanic couple. This layer inhibited the cathodic reaction of oxygen reduction, and the overall corrosion process was hindered. On the other hand, BTA was released by exchanging with chlorides (thus, chlorides were trapped, while the inhibitor was released) and/or hydroxyl ions, forming an adsorbed layer on the surface of the aluminum alloy [35]. The corrosion protection effect of coatings modified with ion exchange pigments loaded with cooperative inhibitors was demonstrated for the first time, thus delivering a concept that can be used to protect several metallic couples either on hybrid joints or in multimetal joints.

Plasma electrolytic oxidation (PEO) coatings were investigated as possible routes for the protection of galvanic couples and Ti and Al alloys [36]. The results demonstrated that the galvanic effects were substantially reduced when the PEO coating was deposited over the Al alloy. The beneficial effect was not so evidenced for Ti alloys, because both the uncoated and coated Ti alloys revealed increased resistance against galvanic corrosion.

Similarly to what has been observed for metal-metal joints, the presence of coatings in metal-nonmetallic assemblies can be envisaged as a route to minimize the corrosion susceptibility.

3.5 Future trends

Presently, the search for lightweight structures, characterized by improved mechanical properties, is one of the top priorities in many industries, such as the automotive and aeronautical industries. Metal-metal assemblies and the joining of metals with very distinct properties such as steel and Al alloys or Mg and aluminum alloys are critical and will evolve in the near future. These materials, because of their electrochemical behavior, are very susceptible to multiple corrosion problems. On the other hand, the joining technologies also create interfaces that are very susceptible to the

onset of corrosion and that create all the conditions for the onset of galvanic corrosion. For example, friction stir welding (FSW) creates zones with different levels of stress and microstructures that increase the probability of corrosion-related problems. Thus, post treatments, coatings, and other surface treatments become critical for minimizing the problem.

The use of laser joining able to produce stable interfaces, including chemical (or ionic) bonding between nonmetallic and metallic components is another promising route to tailor interfaces with improved behavior. The possibility of tailoring the properties of the joined materials by optimizing various laser welding parameters contributes to the overcoming of corrosion-related issues in laser-joined parts.

Glue bonding is another form of joining that is considered, because it can be used to join any kind of materials, especially very dissimilar ones. It allows for the reduction of local corrosion effects, but there are still several disadvantages, such as fast ageing, mechanical strength, and reduced stiffness.

Hybrid assemblies, joining metallic alloys and nonmetal composites, present a real challenge. When they are directly jointed, there is an increased risk of galvanic corrosion failure. Therefore, it is essential to design transition zones that can minimize the corrosion susceptibility while ensuring mechanical integrity and strong adhesion. Different transition zones must be studied. These include rubbers, polymers, adhesives, and coatings. Moreover, there is a need of material manipulation at the nanoscale level to minimize microcracking and microgalvanic effects. In this area the controlled addition of fillers, such as carbon nanotubes, and metallic or composite laminates, may play a critical role.

New adhesives, including adhesives modified with corrosion inhibitors either freely dispersed or encapsulated, for symmetric and dissymmetric joined materials can be a solution to overcome some localized corrosion effects. The introduction of nanofillers in these additives, targeted to increase mechanical properties, adhesion, and corrosion resistance are a step forward in advanced joining strategies. Certainly these advanced interfaces can place together many distinct materials, combining the best properties of the individual materials in a composite component.

Delamination and galvanic corrosion effects are major issues to be overcome in order to deliver new materials with improved properties for critical components in many sectors. For these purposes coatings and corrosion inhibitors are strategic routes. However, very little is known in this field, and new advances are urgent. Such new protection strategies will pave the way for a widespread use of these materials and for its reliability in structurally high-risk components. These will certainly be explored in the future.

There is undoubtedly a need for new multimetal combinations, either symmetric or dissymmetric. However, in parallel, the joining technologies must be optimized to overcome the multiple gaps related to corrosion performance. It is clear that all these advances need a concerted interdisciplinary effort by material science, chemistry, nanomaterials, and engineering to find more advanced solutions which can min-

imize the impact of corrosion in joined materials, while contributing for increased reliability of joined materials and its widespread application.

Acknowledgement

Fundação para a Ciência e Tecnologia (FCT) for funding under the contract UID/QUI/00100/2013

References

[1] Le Bozec N, LeGac A, Thierry D. 2012. Corrosion performance and mechanical properties of joined automotive materials, *Materials and Corrosion* **63**, 408–4015.
[2] LeBozec N, Thierry D. 2014. A new device for simultaneous corrosion fatigue testing of joined materials in accelerated corrosion tests, *Materials and Corrosion*, doi:10.1002/maco.201407984.
[3] Zhang MJ, Chen GY, Zhang Y, Wu KR. 2013. Research on microstructure and mechanical properties of laser keyhole welding–brazing of automotive galvanized steel to aluminum alloy, *Materials and Design* **45**, 24–30.
[4] Wloka J, Laukant H, Glatzel U, Virtanen S. 2007. Corrosion properties of laser beam joints of aluminum with zinc-coated steel, *Corrosion Science* **49**, 4243–4258.
[5] Chen HC, Pinkerton AJ, Li L, Liu Z, Mistry AT. 2011. Gap-free fibre laser welding of Zn-coated steel on Al alloy for light-weight automotive applications, *Materials and Design* **32**, 495–504.
[6] Bergmann JP, Stambke M, Schmidt S. 2013. Influence of aluminum coating and diffusion affecting additives on dissimilar laser joining of steel and aluminum, *Physics Procedia* **41**, 190–198.
[7] Schiel M, Kreling S, Fischer F, Dilger K. 2015. Behavior of adhesively bonded coated steel fo automotive applications under impact loads, *International Journal of Adhesion & Adhesives* **56**, 32–40.
[8] Calabrese L, Bonaccorsi L, Proverbio E, Di Bella G, Borsellino C. 2013. Durability on alternate immersion test of self-piercing riveting aluminum joint, *Materials and Design* **46**, 849–856.
[9] Dhanapal A, Rajendra Boopathy S, Balasubramanian V. 2012. Influence of pH value, chloride ion concentration and immersion time on corrosion rate of friction stir welded AZ61A magnesium alloy weldments, *Journal of Alloys and Compounds* **523**, 49–60.
[10] Dong P, Sun D, Wang B, Zhang Y, Li H. 2014. Microstructure, microhardness and corrosion susceptibility of friction stir welded AlMgSiCu alloy, *Materials and Design* **54**, 760–765.
[11] Proton V, Alexis J, Andrieu E, Delfosse J, Lafont MC, Blanc C. 2013. Characterisation and understanding of the corrosion behaviour of the nugget in a 2050 aluminum alloy friction stir welding joint, *Corros. Sci.* **73**, 130–142.
[12] Wadeson DA, Zhou X, Thompson GE, Skeldon P, Djapic Oosterkamp L, Scamans G. 2006. Corrosion behaviour of friction stir welded, *Corros. Sci.* **48**, 887–897.
[13] Paglia CE, Buchheit RG. 2006. Microstructure, microchemistry and environmental cracking susceptibility of friction stir welded 2219-T87, *Mater. Sci. Eng. A* **429**, 107–114.
[14] Kang J, Fu RD, Luan GH, Dong CL, He M. 2010. In-situ investigation on the pitting corrosion behaviour of friction stir welded joint of AA2024-T3 aluminum alloy, *Corros. Sci.* **52**, 620–626.

[15] Jariyaboon M, Davenport AJ, Ambat R, Connolly BJ, Williams SW, Price DA. 2007. The effect of welding parameters on the corrosion behaviour of friction stir welded AA2024-T351, *Corros. Sci.* **49**, 877–909.
[16] Bousquet E, Poulon-Quintin A, Puiggali M, Devos O, Touzet M. 2011. Relationship between microstructure, microhardness and corrosion sensitivity of an AA 2024-T3 friction stir welded joint, *Corros. Sci.* **53**, 3026–3034.
[17] Padovani C, Davenport AJ, Connolly BJ, Williams SW, Siggs E, Groso A, Stampanoni M. 2011. Corrosion protection of AA7449-T7951 friction stir welds by laser surface melting with an Excimer laser, *Corros. Sci.* **53**, 3956–3969.
[18] Hatamleh O, Singh PM, Garmestani H. 2009. Corrosion susceptibility of peened friction stir welded 7075 aluminum alloy joints, *Corrosion Science* **51**, 135–143.
[19] Deng Y, Ye R, Xu G, Yang J, Pan Q, Peng B, Cao X, Duan Y, Wang Y, Lu L, Yin Z. 2015. Corrosion behaviour and mechanism of new aerospace Al–Zn–Mg alloy friction stir welded joints and the effects of secondary $Al_3Sc_xZr_{1-X}$ nanoparticles, *Corrosion Science* **90**, 359–374.
[20] S.-Moghaddam M, Parvizi R, Davoodi A, Haddad-Sabzevar M, Imani A. 2014. Estabilishing a correlation between interfacial microstructures and corrosion initiation sites in Al/Cu joints by SEM-EDS and AFM-SKPFM, *Corrosion Science* **79**, 148–158.
[21] Liu C, Chen DL, Bhole S, Cao X, Jahazi M. 2009. Polishing-assisted galvanic corrosion in the dissimilar friction stir welded joint of AZ31 magnesium alloy to 2024 aluminum, *Materials Characterization* **60**, 370–376.
[22] Yang Y, Zhou L. *Journal of Materials Science & Technology*, doi:10.1016/j.jmst.2014.07.017.
[23] Chen T, Xue W, Li Y, Liu X, Du J. 2014. Corrosion behavior of friction stir welded AZ31B magnesium alloy with plasma electrolytic oxidation coating formed in silicate electrolyte, *Materials Chemistry and Physics* **144**, 462–469.
[24] Kish JR, Williams G, McDermid JR, Thuss JM, Glover CF. 2014. Resistance of Friction Stir Welded Mg Alloy AZ31B Joints, *J. Electrochem. Soc.* **161**(9), C405–C411.
[25] Wielage B, Mucklich S, Grund T. 2007. Corrosion behaviour of soldered joints of magnesium alloys and dissimilar materials, *Microchim. Acta* **156**, 151–157.
[26] Li WY, Jiang RR, Huang CJ, Zhang ZH, Feng Y. 2015. Effect of cold sprayed Al coating on mechanical property and corrosion behavior of friction stir welded AA2024-T351 joint, *Materials and Design* **65**, 757–761.
[27] Sarlin E, Heinonen E, Vuorinen J, Vipola M, Lepisto T. 2014. Adhesion properties of novel corrosion resistant hybrid structures, *International Journal of Adhesion & Adhesives* **49**, 51–57.
[28] Sarlin E, Hoikkanen E, Frisk Vuorinen L J, Vipola M, Lepisto T. 2014. Ageing of corrosion resistant steel/rubber/composite hybrid structures, *International Journal of Adhesion & Adhesives* **49**, 26–32.
[29] Ireland R, Arronche L, Saponara VL. 2012. Electrochemical investigation of galvanic corrosion between aluminum 7075 and glass fiber/epoxy composites modified with carbon nanotubes, *Composites: Part B* **43**, 183–194.
[30] Gkikas G, Sioulas D, Lekatou A, Barkoula NM, Paipetis AS, 2012. Enhanced bonded aircraft repair using nano-modified adhesives, *Materials and Design* **41**, 394–402.
[31] Funatsu K, Fukuda H, Takei R, Umeda J, Kondoh K. 2013. Quantitative evaluation of initial galvanic corrosion behavior of CNTs reinforced Mg–Al alloy, *Advanced Powder Technology* **24**, 833–837.
[32] Liu Z, Curioni M, Jamshidi P, Walker A, Prengnell P, Thompson GE, Skeldon P. 2014. Electrochemical characteristics of a carbon fibre composite and the associated galvanic effects with aluminum alloys, *Applied Surface Science* **314**, 233–240.

[33] Mandel Kruger M L. 2013. Determination of pitting sensitivity of the aluminum alloy EN AW-6060-T6 in a carbon-fibre reinforced plastic/aluminum rivet joint by finite element simulation of the galvanic corrosion process, *Corrosion Science* **73**, 172–180

[34] Mandel and Krüger M L. 2014. Long-term corrosion behaviour of EN AW-6060-T6 in an aluminum/carbon-fibre reinforced polymer self-piercing rivet joint, *Mat.-wiss. u. Werkstofftech.* **9999**: n/a. doi:10.1002/mawe.201400352.

[35] Serdechnova M, Kallip S, Ferreira MGS, Zheludkevich ML. 2014. Active self-healing coating for galvanically coupled multi-material assemblies, *Electrochemistry Communications* **41**, 51–54.

[36] Peng Z, Nie X. 2013 Galvanic corrosion property of contacts between carbon fiber cloth materials and typical metal alloys in an aggressive environment, *Surface and Coatings Technology* **215**, 85–89.

Mikhail L. Zheludkevich, Silvar Kallip, and Maria Serdechnova

4 Protection of multimaterial assemblies

Abstract: The light-weight design calls for broader utilization of multimaterial mixes (M^3) in different engineering structures, especially in the transportation area. Together with joining technologies for hybrid structures, the optimization of the life cycle of such systems is an issue of prime importance. Multimaterial structures are often prone to faster degradation under service conditions because of galvanically forced electrochemical corrosion. The protection technologies traditionally used for single-material structures are not always applicable for multimaterial design because of compatibility issues and a stronger thermodynamic driving force for degradation. In this chapter different strategies for protection of multimaterials structures are briefly overviewed. The main focus is on new alternative protection systems based on combination of synergistic inhibiting mixtures introduced into protective coatings. A road map which can be followed in order to create an efficient active protection coating for hybrid structures is suggested.

4.1 Demands on light weight engineering and associated issues

Nowadays the complex design of modern engineering structures frequently includes various different materials in the same system. Metals and alloys are still among most used construction materials for different applications. However, the modern concepts of light design call for new solutions, especially for the transport industries. The strategies of the "light car" and "green aircraft" promoted in Europe are based on a desirable significant weight reduction of future vehicles, aiming at the lower fuel consumption and consequently also the reduction of carbon dioxide emission.

The lightweight design concept is grounded on usage of alternative materials with comparable mechanical properties and lower weight. Thus Mg alloys, Al alloys, Ti alloys, high-strength steels, and carbon fibre reinforced plastics (CFRP) are considered by automotive and especially by aeronautical manufacturers for different primary and secondary structural parts [1]. However, the combination of several different materials in the same structure raises many challenges, such as the need for new forming and joining technologies as well as surface protection processes. Among the most critical issues is the galvanic incompatibility of different conductive materials in the same assembly. Formation of galvanic coupling between the dissimilar materials can cause an unpredictable and rapid corrosion degradation of more active material. For instance, if CFRP and Al alloy are in electrical contact, the dissolution of Al alloy will occur when exposed to corrosive environment [2–4]. However, this phenomenon is inconsistent with the objective of increasing maintenance intervals and optimized life cycle.

Galvanic corrosion is an issue of great concern in both the automotive and aerospace industries. One of the ways to estimate the importance of this problem is to use simulation approaches in order to define the most critical galvanic combinations, structure designs, and exploitation conditions. The fundamentals of galvanic corrosion are generally quite well understood. However, the difference between scientific research and the performance of real system in real conditions can be notable. On the other hand, reliable simulations can also contribute to proper design of protection schemes for various scenarios appearing in multimaterials structures.

There were several attempts to model the galvanic corrosion processes in aircraft-relevant aluminum+CFRP galvanic couples. Palani et al. have tried to develop a model which can adequately describe the galvanic corrosion processes in thin electrolyte conditions that could occur in the upper part of an aircraft fuselage [5]. The numerical model was based on solving the electroneutrality equation with a three-dimensional boundary/finite element bethod. This approach can be applied to different hybrid structures relevant for aircraft frames. Specific variations in the environmental condition can be considered, including different aggressiveness of electrolytes and different thicknesses of electrolyte film. The use of multimaterial mixes is becoming increasingly important in automotive body design. There are several relevant combinations which can lead to serious galvanic corrosion issues. The Al+CFRP galvanic couple discussed above and all the respective corrosion issues are also relevant for automotive structures.

One of the attractive materials to be integrated within the car body is magnesium because of its low density and consequently its high weight-saving potential. However, the galvanically induced corrosion of magnesium alloys is a primary concern in this case. Of all the structural metals, magnesium has the most active galvanic potential and suffers serious galvanic corrosion when coupled with a different metal or CFRP. Jia et al. have used a similar boundary element method (BEM) simulation approach to model the galvanic corrosion of magnesium alloy AZ91D coupled to a steel fastener [6]. The total corrosion rate of the Mg part was composed by two additive components consisting of galvanic corrosion and self-corrosion. The experimental measurements were performed in order to validate the model and demonstrate good agreement between the experiment and BEM model. The model has predicted a similar distribution of the current density for AZ91D+steel galvanic couple: a maximum at the interface with quickly decrease to zero within 1 to 2 cm from the interface, as shown in Fig. 4.1.

The obtained results clearly demonstrate that utilization of steel fasteners can be critical when joining the Mg alloys. AA6xxx fasteners, for example, cause significantly lower galvanic corrosion of Mg during salt spray tests [7]. An important factor in this case is a significantly lower difference of galvanic potentials between the fastener and Mg structure. Galvanic coating of steel with more active metallic layers can be also used in order to reduce the galvanic couple in the case when steel fasteners or bolts are not avoidable [8]. Zn-based Sn+Zn metallic coatings [9] have reasonable galvanic

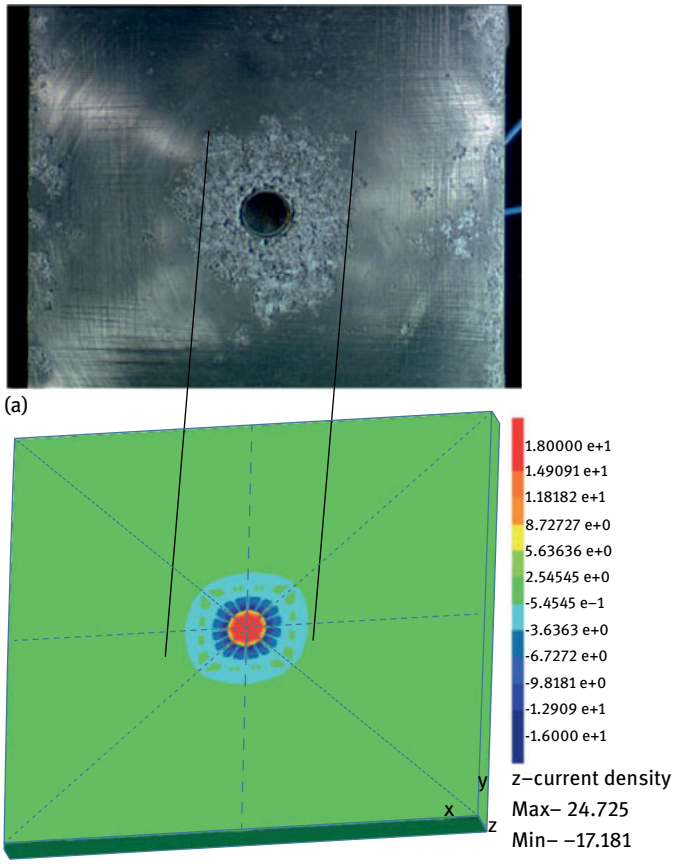

Fig. 4.1: Comparison of the galvanic corrosion area for BEM model and the immersion test for 10 mm diameter steel cathode: (a) experimental immersion test; (b) the BEM model [6].

compatibility with Mg alloys when exposed to salt-containing electrolytes. The application of additional polymer coatings to the fastener (or bolt) surface can also be considered as a potential approach [10].

Different joining technologies can be applied for hybrid structures including above mentioned mechanical fastening, adhesive bonding, laser-beam welding, and friction stir joining [11].

One joining approach is the laser weld brazing (LWB) which can be used to galvanize steel with aluminum components by the use of either zinc- or aluminum-based filler alloys [12]. This laser-based joining technology has a shorter processing time, good adaptability, and a good weight reduction/cost ratio in serial production when compared to adhesives and rivets for steel-aluminum mixed structures. However, the corrosion of used filler material can be significantly accelerated by galvanic coupling

with respective substrates causing accelerated degradation of the brazed seam. Moreover, long-term galvanic effects are possible in a good conductive medium.

The testing of multimaterial assemblies in order to understand their susceptibility to galvanically induced corrosion attack is another important challenge. The standard electrochemical methods or accelerated corrosion tests are not always applicable. For example, the interpretation of electrochemical impedance spectroscopy results obtained on galvanically coupled multimaterial samples is not straight forward, since the contribution from both substrates are difficult to separate. Moreover, the linearity requirement is not always achieved because of the remarkable galvanic currents passing between the anode and the cathode. The test samples for accelerated corrosion tests should be also designed in a different way when compared to the single-material samples. One of the test sample geometry for brazed steel+Al sample is demonstrated in Fig. 4.2.

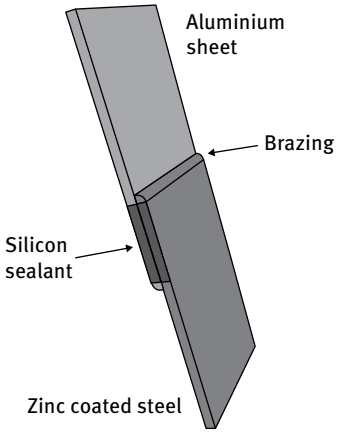

Fig. 4.2: Arrangement of brazed multi-material specimen for salt spray test, adopted from [12].

It is important to notice that the type of joining method and the sealing of the joint can drastically influence the results in accelerated corrosion tests, since only relatively thin films are present on the surface during the test. Thus the geometry of the joint or its positioning in the chamber will influence the liquid film formed and its conductivity, which is decisive for galvanic coupling. The geometrical factors such as distance between the cathode and anode, cathode/anode area ratio, the thickness of the electrolyte film, and the shapes of the electrodes are important [13]. Moreover, several galvanic couples can be present in the same structure, e.g. several steel fasters for one magnesium part. There can be an interaction/superimposition of the currents resulting from each galvanic couple. One of the ways to test the galvanically coupled materials and understand the geometrical effects on the local galvanic currents is to use multielectrode assemblies with numerous electrodes, which can be coupled and

decoupled on demand. A multielectrode arrangement to study the Mg+Fe galvanic couple is demonstrated in Fig. 4.3.

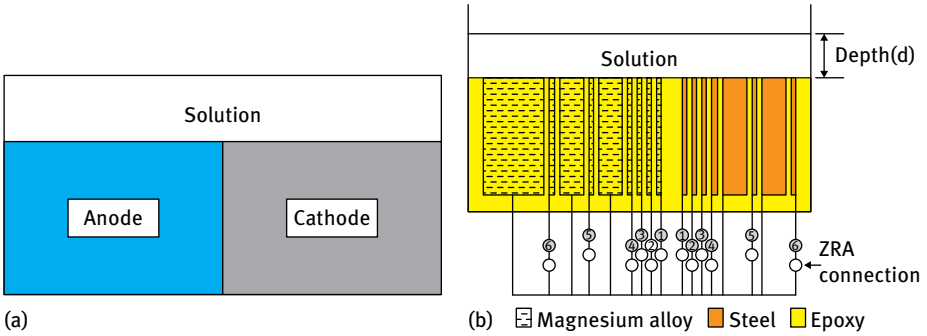

Fig. 4.3: (a) Schematic of idealised one-dimension galvanic couple. (b) Section through multielectrode Mg–steel galvanic corrosion assembly (GCA), adopted from [13].

The multimaterial approach also multiplies the amount of the required testing time, especially when new corrosion inhibitor systems are to be developed. Therefore the systematic high-throughput concept has been considered [14] by Taylor et al. The multielectrode arrays of identical AA2024-T3 pairs were immersed in numerous separated reaction cells, and a potentiodynamic analysis qA performed for estimation of polarization resistance. A large amount of different corrosion inhibitor solutions were tested simultaneously. More recently Mol et al. [15] has proposed a multielectrode assembly which contains several different materials in the same epoxy mount and could be immersed in the same testing solution for simultaneous potentiodynamic analysis (Fig. 4.4).

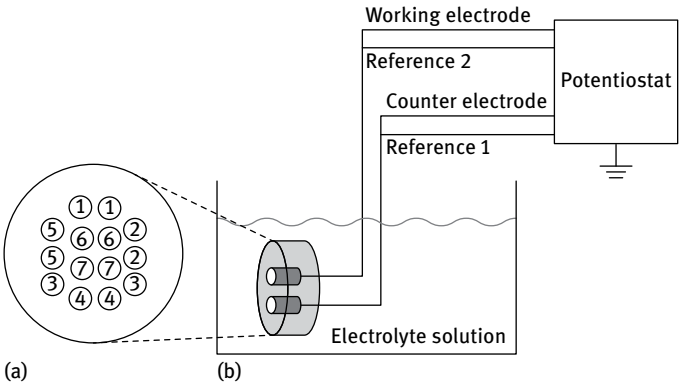

Fig. 4.4: Face view of multielectrode assembly showing the layout of wire specimens (a) and schematic of experimental setup for an individual electrode pair [15].

Although the DC-polarization technique is destructive for the electrode surfaces, and additionally due to the electrochemical excitation, cross-contamination of different materials in the test cell may also occur. Therefore a noninvasive localized measurement technique SVET (scanning vibrating electrode technique) has been considered as a high-throughput electrochemical method for simultaneous corrosion inhibitor screening for multimaterial applications. It measures the localized corrosion-related ionic currents and allows observation of the distribution and evolution concurrently for both anodic and cathodic processes. Also the conditions during the SVET operation are close to an undisturbed environment, as the natural corrosion process is not influenced by any applied polarization. Historically the SVET method was initially applied in the life sciences [16–19], and only later introduced in corrosion research [20–22]. SVET has also been coupled with a wire beam electrode (WBE) by Battocchi et al. (Fig. 4.5) [23]. The designed model cell contains eight Al and one Cu electrodes, which are electrically connected and could therefore emulate the galvanic situation on AA2024-T3 surface (Fig. 4.5). In Fig. 4.6 the ionic current distribution on this electrode is presented. It can be seen how the localized cathode on Cu and anodes at Al electrode were formed.

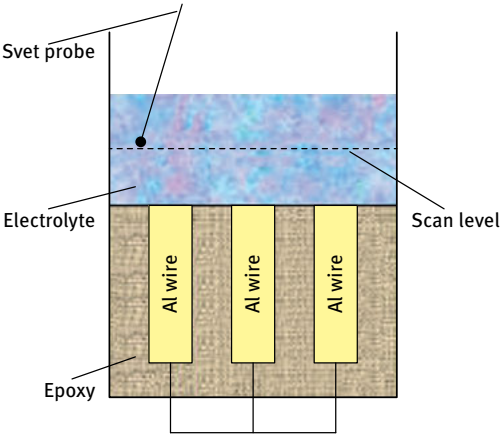

Fig. 4.5: SVET measurement set-up, adopted from [23].

Reproducing the film electrolyte conditions over galvanically coupled materials is an even more challenging task, especially when a controllable film thickness is required. Recently Hack et al. patented a method and device which allow precise control of the electrolyte film thickness [24]. The arrangement of the respective test sample and the testing setup are shown in Fig. 4.7. The formation of a uniform thin film is based on the theory of Nusselt for falling film-wise condensation on a vertical flat plate. In general, the condensation of the electrolyte mist begins at the top and moves downward with the force of gravity, creating a laminar flow. The tested substrates are connected

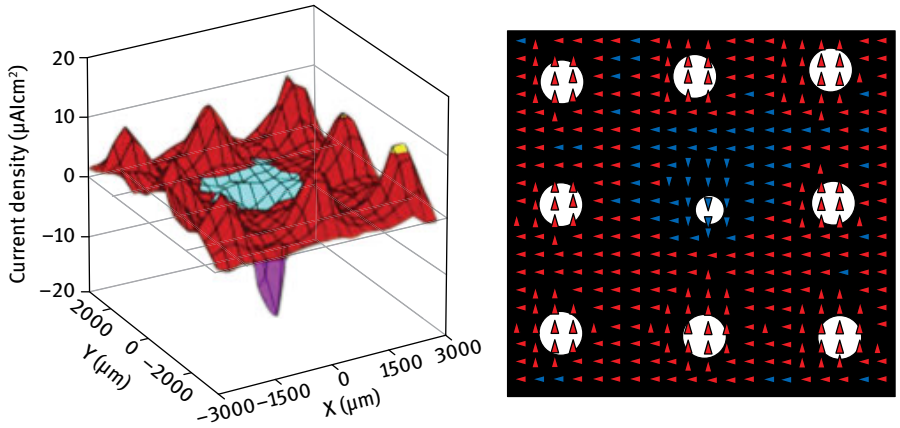

Fig. 4.6: Current density map (*left*) and optical micrograph with current density vectors (*right*) of 8Al–1Cu WBE after 1h of immersion in 0.35 wt.% $(NH_4)_2SO_4$ + 0.05 wt.% NaCl solution, adopted from [23].

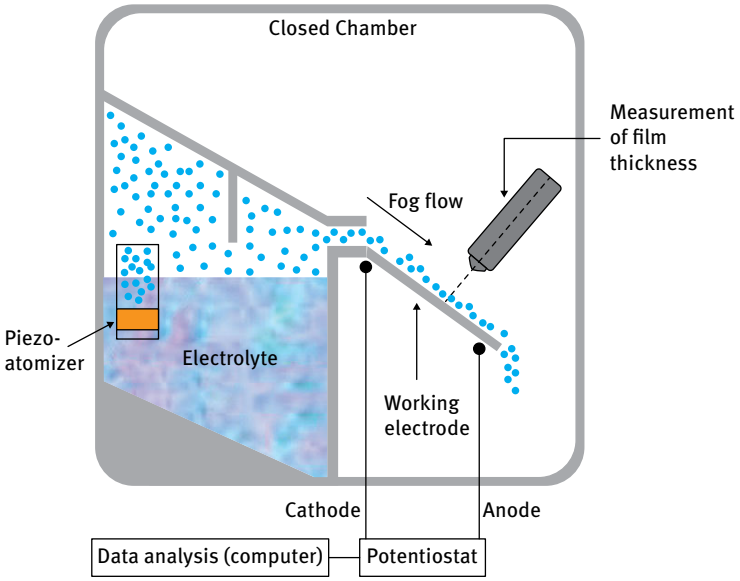

Fig. 4.7: Schema of the setup used for thin film tests of multimaterials assemblies, adopted from [11].

as electrodes to the ZRA, which allows in situ measurement of the galvanic current passing between the cathode and the anode [11]. In this way, different material combinations can be tested under condensing conditions, which are relevant for many applications of hybrid structures.

The understanding of the galvanic corrosion issues for a specific combination of materials, relevant geometries, and conditions is an important starting point for the proper design of multimaterial structures. Moreover, the knowledge of these issues creates a basis for the further development of protection strategies. The main ways used for protection of multimaterial structures are briefly overviewed in the next section, with particular focus on novel active protection approaches.

4.2 Approaches to mitigate corrosion issues in multimaterial systems

4.2.1 Passive protection

The galvanic corrosion occurs only in the case where three important conditions are met: (1) a significant difference of the galvanic potentials of joined materials, (2) electrical contact between the dissimilar materials, and (3) the presence of electrolytes in simultaneous contact with both materials. The main passive protection methods for hybrid structures are based on strategies which try to eliminate one of these factors from the equation.

The first logical approach to prevent the galvanic corrosion issues is to avoid the electrical contact between the dissimilar materials in a hybrid structure. Most of the joining methods create a direct contact between the materials, allowing electrons to pass easily. However, the use of adhesive bonding can eliminate the electrical contacts. In this situation the acceleration of corrosion processes due to the galvanic coupling can be avoided. In most of the structural applications the pure adhesive bonding is rarely applied, especially in the aeronautics industry. Instead, hybrid joints are preferred which combine the adhesive bonding with additional mechanical fastening. In this case electrical contact is created, and the galvanic corrosion issue arises again. In the case of aeronautical applications, one more obstacle in adhesive bonding may occur as the electrical contact between all structural parts of aircrafts is desired in order to avoid the problems of static discharging and lightning strikes.

Another possibility is to reduce the difference of the galvanic potentials between the materials used in design. This possibility is often impossible, since selection of the materials is defined by the required mechanical properties, weight, thermal conductivity, etc. Therefore, flexibility in the choice of materials is often limited. In some situations the potential difference can achieve extreme values, as in the case of Fe+Mg or CFRP+Al multimaterial mixes. The difference in the galvanic potentials is the main driving force for accelerated corrosion. However, in the case of low electrolyte conductivity or very thin electrolyte layer, if dissimilar materials are positioned in the structure together, the potential drop can be significant. Thus the galvanic current can be drastically reduced. Use of insulating spacers in critical zones is not always possible. Therefore another metal with intermediate galvanic potential is often introduced as

a spacer between the noble and active components. In the case of aeronautical structures Ti is often used for a transition between CFRP and Al alloys. In the case of automotive structures, Al alloy spacers can be applied between of Mg alloy and steel components, in order to avoid a sharp change of galvanic potential. Fig. 4.8 demonstrates the design of the hinge connection to the Mg part of a car door. The aluminum alloy is introduced between the steel and Mg parts in order to reduce the local potential difference.

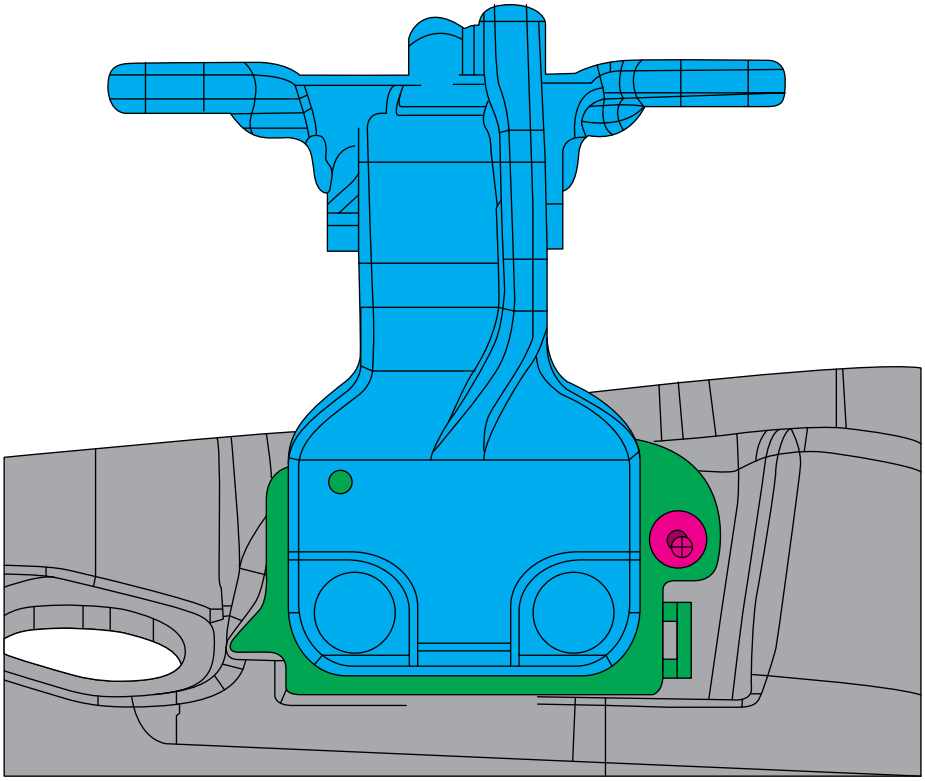

Fig. 4.8: Attachment of the steel hinge to the Mg inner part via an aluminum plate [25].

Application of sealants and barrier coatings is one of the main strategies utilized in protection of dissimilar joints against galvanic corrosion. In both automotive and aeronautical structures the critical zones are often sealed with polymer sealants, which prevent the direct contact of moisture with both dissimilar parts. The strategy functions well in areas where only a very thin electrolyte film can be formed on the surface. The sealing is also very important to protect the occluded zones susceptible to the accumulation of electrolytes. However, the sealing of the joint area is not sufficient in the situation where hybrid structures are used in immersed conditions, such

as the bottom internal part of an aircraft fuselage, where a significant amount of liquid can be accumulated during operation. The application of the protective coatings can be considered to be an ultimate solution. The coating creates a physical barrier between the electrolyte and substrate. Thus no corrosion can occur as long as there is no failure of this ideal barrier. The problem is that different coating systems and various often incompatible technologies are applied for different substrates, with the first complications already arising at the cleaning/pretreatment stage. Conditions suitable, for example, for aluminum alloys can be too harsh for magnesium-based materials. Therefore, pretreatments or even some coating layers can be applied before the joining and the final coating is done over the joined and partially precoated components. An example of such process suggested for the Mg+Al rear door of a Volkswagen car is demonstrated in Fig. 4.9.

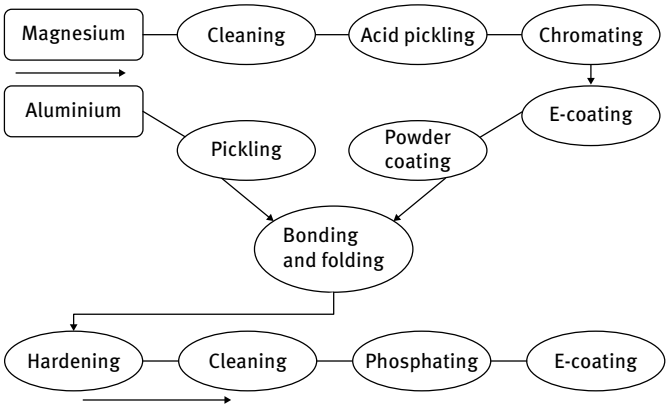

Fig. 4.9: Schematic representation of the coating process for Al+Mg hybrid structure, adopted from [26].

The magnesium panels are first degreased and rinsed. At the second step about 20–30 µm of the casting crust is removed by acidic etching. Then the surface is rinsed, chromate, and dried. All the chemicals are applied using the spray process. The eCoat is applied in the next step and cured for 15 min at 180 °C. Finally, a powder coating is applied and baked at 200 °C for 10 to 15 min.

The surface of aluminum panels is standardized by acidic pickling. Hybrid bodies are then formed and bonded. In the next processing step, the hybrid body is put through the eCoat in the steps of degreasing, phosphatization, eCoat application, and baking at 180 °C for 14 min. Only the aluminum sheet in the process absorbs the eCoat, while the magnesium panel is electrically insulated by the coating powder [26]. As one can see the total process is significantly more complicated than the one used for a conventional car body. This fact leads to unfavorable cost aspects, especially for mass production cars. The ideal scenario would be the application of the same surface treat-

ment process for the entire multimaterial car body composed of different steels, Al alloys, Mg alloys, and reinforced composites. Recent developments have focused on surface treatment technologies which can be applied for multimaterial substrates. For example, tuning the electrolyte composition and the electrical parameters of plasma electrolytic oxidation allows the formation of anodic coatings on Al (AA7075) and Mg (ZE41) substrates. Microdischarges were sustained on both metals for the optimized conditions, and coatings were produced with thicknesses reasonably similar to those of the coating on metals treated individually [27].

The important issue is that even when an "ideal" coating is applied to the hybrid structure, with time the barrier can be disrupted during use and certain defects may appear. A rapid degradation reinforced by galvanic coupling can then occur in the coating defect. Fig. 4.10 demonstrates a coated Mg alloy sample galvanically coupled to uncoated steel. One can clearly observe an intensive paint delamination and corrosion of Mg substrate underneath. Thus, even a well-coated multimaterial assembly can quickly begin to degrade when defects appear in the protective coatings. Moreover, the corrosion process can be of a very localized nature and lead to unpredictable failure of the respective part.

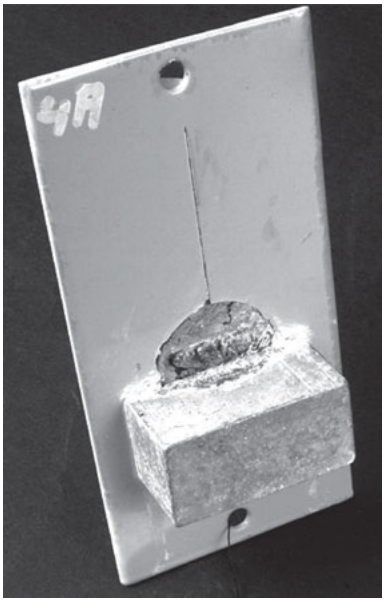

Fig. 4.10: Coated Mg alloy coupled to steel after 30 cycles according to the Volkswagen testing regulation PV 1210 [26].

4.2.2 Active protective coatings with corrosion inhibitors

The introduction of active inhibiting compounds to the protection system is a promising approach which can add active protection to the passive protection methods reviewed above. Corrosion inhibitors can be introduced in hybrid structures incorporated in coatings, sealants, or structural adhesives. In the two last cases the inhibitor is placed as near as possible to critical places such as confined environments and multimaterial joints. In the case of aeronautical applications a chromate conversion layer and chromated primer provide very effective corrosion inhibition ability for Al alloy structures [28, 29]. However, present regulations impose restrictions on the use of chromates, and therefore new solutions are needed. Thus, the search for effective anticorrosion coatings containing self-healing active species which could replace chromates has been very much in the forefront [30–33].

The corrosion inhibitor can be introduced directly to the coating, but in that case it must be compatible with the coating matrix, and it should be able to reach the active surface in order to suppress corrosion. In the case of sol-gel and silane-based coatings several successful systems have been discussed [33–35]. There are even some specific cases recognized where the coating barrier properties have been improved with the introduction of inhibitors. However, there is always a risk of the uncontrollable leakage of the inhibitor from the coating and loss of its long term effectiveness [36]. Moreover, usually the stability and barrier properties of coatings will be significantly decreased due to the unwanted interaction of corrosion inhibitors and coating formulations [37]. Application of highly soluble inhibitors can also give rise to issues around strong osmotic blistering [38].

In order to diminish these negative effects, entrapping the corrosion inhibitor in nanocontainers has been suggested. This approach can protect the coating formation during the paint application process from the destructive influence of corrosion inhibitors. Later these nanocarriers, if they have specially designed functional properties, can release corrosion inhibitors *on demand*. The container release function can be triggered in various ways to react to different corrosion relevant stimulus (pH, chlorides, stress, mechanical damage, or UV light) [37, 39–41]. Recently several works appeared suggesting various possibilities for selecting and designing containers for corrosion inhibitors, for example oxide nanoparticles [34], β-cyclodextrin fillers, plasmapolymer shells [42], cellular nanocontainers (diatomaceous earth, zeolite, or carbon-based) [43], and ion (anion [44] and cation [45]) exchangers. Another promising possibility is to prepare nanoreservoirs with “smart” storage/release properties, using the polyelectrolyte layer by layer (LbL) assembled shells, which change the permeability depending on the pH and ionic strength [37]. The layered double hydroxides and mesoporous nanoparticles have also proven to be promising candidates for the encapsulation of different corrosion inhibitors [46, 47].

The situation is even more complicated and demanding in the case of multimaterial substrates, where galvanic activities beneath the coating could be suspected. One

possible option to deal with this is the incorporation of different functional nanocontainers for each of the substrate materials, which is also more thoroughly discussed in the present chapter, for instance one nanocontainer system dedicated to the suppression of a cathodic reaction and another one for an anodic site. The synergistic effect of encapsuled corrosion inhibitors is also desired [48]. Different inhibitors used together can confer efficient inhibition at different conditions, one working at anodic (acidic) conditions, and another at a cathode, where high pH levels are expected. This approach is especially relevant in the case of coatings for multimaterial structures where a clear separation between cathodic and anodic sites happens due to galvanic effects. Using several inhibitors in the same system opens opportunities for cooperative actions between them resulting in synergistic inhibition effect. This can allow significant reduction of the minimal critical inhibitor concentration needed to ensure suppression of corrosion processes in defects. Only a small number of papers have been published recently which focus on this aspect. The best synergistic combinations of corrosion inhibitors are yet to be found. There are two main possibilities of how to implement this strategy in coatings: to use a low-soluble complex pigment composed of two inhibiting constituents (cerium dibutylphosphate ($Ce(dbp)_3$) [49], praseodymium diphenylphosphate ($Pr(dpp)_3$) [50], rare earth + mercaptoacetate [51], cerium cinnamate [52], cerium molybdate [53, 54]); to introduce two inhibitors in the same coating system separately in an encapsulated form (double doped zeolites [55], LDH-BTA + Bentonite-Ce [48]).

The next part of the chapter concerns special example of the successful development of an active protective coating for galvanically coupled multimaterial systems. Different important steps are shown in order to suggest a road map which can be followed for specific hybrid structures.

Step 1: Exploring synergistic mixtures of corrosion inhibitors

Galvanic corrosion is generally a very challenging phenomenon for corrosion inhibitors as the thermodynamic driving force to corrode can be very high [56]. Therefore a majority of the current inhibitor systems are mostly only able to efficiently protect single material structures. In the case of aeronautical grade Al alloys several intermetallic phases such as the widely investigated Al-Cu-Mg second phase behave like a galvanic systems at the microlevel [57, 58] and for this particular case several highly efficient solutions were developed. The usage of chromates [28, 29] for aluminum alloys has been an efficient and robust solution, but also the selection of other, more environmentally friendly and less toxic potential candidates is large [59]. However, when the Al alloy is coupled with more noble conductive material like CFRP, advanced synergistic corrosion inhibitor mixtures are desired.

Recently the synergistic behavior of two known corrosion inhibitors, 1,2,3-benzotriazole (BTA) and Cerium (III) nitrate ($Ce(NO_3)_3$), has been demonstrated to be

a suitable active protective combination for an Fe + Zn galvanic couple in a chloride medium [60].

BTA is among the efficient corrosion inhibitors for different metals, especially for copper and its alloys, and has have been well known for more than sixty years [61]. Mostly it acts as a mixed-type inhibitor through physical and chemical adsorption as well as different Cu-BTA complex formation mechanisms providing its predominant effect on inhibition of anodic corrosion reaction [62]. One possible structure of adsorption BTA adsorption layer on Cu surface is described in Fig. 4.11.

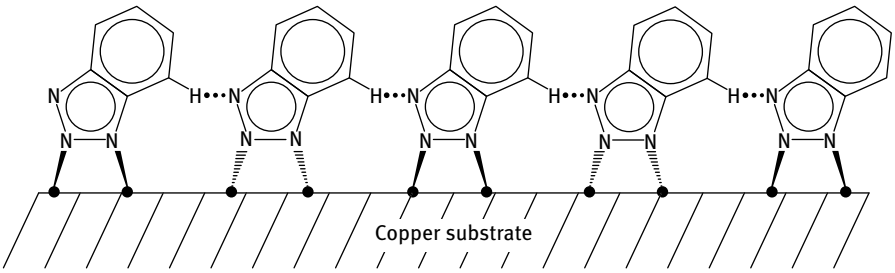

Fig. 4.11: Schematic presentation of chemisorbed layer formed by 1,2,3-benzotriazole adopted from [63].

It is also known that BTA can form protective coatings with Zn [64–66] and Fe [67]. In some circumstances it has been found that BTA can cooperate synergistically with other chemical species like benzylamine [68] and sodium dodecylsulphate (SDS) [69]. The synergism with iodide anions was also recently reported [70]. It is based on the coadsorption of I^- and BTA, which somewhat improves the complex formation with Cu or Fe [67]. However, all these findings about BTA and synergistic cooperation was discussed for suppression of single material corrosion, while the above mentioned combination with $Ce(NO_3)_3$ has been especially designed for galvanic corrosion. The cerium cations (Ce^{3+}) are known as cathodic inhibitors. Similarly to some other rare earth metal (La^{3+}, Y^{3+}) cations they form blocking hydroxide precipitates (reaction 3) due to local pH increase at cathodic sites (reactions 1 and 2) [71–75].

$$O_2 + 2H_2O + 4e^- \rightarrow 4OH^- \tag{4.1}$$

$$2H_2O + 2e^- \rightarrow 2OH^- + H_2 \tag{4.2}$$

$$Ce^{3+}\,(aq) + OH^-\,(aq) \rightarrow Ce(OH)_3\,(s). \tag{4.3}$$

The further oxidation of $Ce(OH)_3$(s) leads to the formation of CeO_2 according to the reaction (2). This compound is also insoluble and prevents the contact of the surface with the aggressive environment [75]:

$$4Ce(OH)_3 + O_2 \rightarrow 4CeO_2 + 6H_2O. \tag{4.4}$$

However, the inhibition efficiency in this case also depends significantly on the intensity of cathodic corrosion reaction, as the forming deposits may possess different structures and composition, which can change the corrosion blocking barrier properties.

The driving idea to combine BTA with cerium nitrate for Zn+Fe galvanic couple has been to find one suitable inhibitor for anodic and another for cathodic reactions.

Experimental approach for evaluation of the synergistic effect

The localized technique SVET coupled with a multielectrode cell has been also applied for corrosion inhibitor screening simultaneously for different single materials [76], but the great advantage of this approach is the possibility to adequately and systematically observe the galvanic corrosion activities when the model electrode with the selected galvanic couples is immersed in different corrosion inhibitor testing solutions or mixtures (Fig. 4.12).

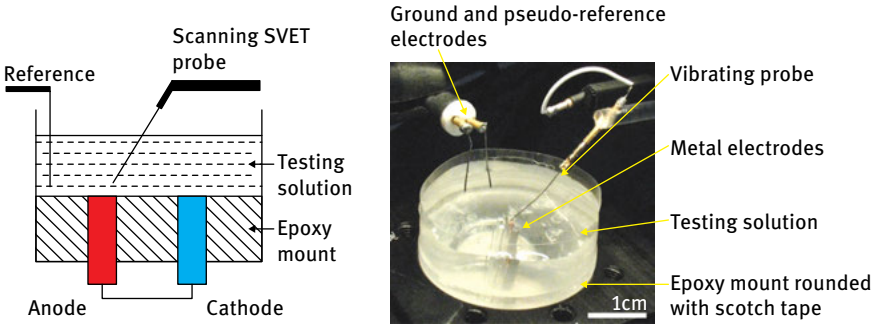

Fig. 4.12: SVET setup for inhibitor testing on galvanic model system.

Using the above described experimental set-up, a screening of corrosion inhibitors was performed for the aeronautically relevant CFRP+Al galvanic couple. The results for two different corrosion inhibitors, which were discussed also above in the context of Zn+Fe galvanic system are: 1,2,3-benzoriazole (BTA) and cerium (III) nitrate were presented in Fig. 4.13. The micrograph of the test-cell and SVET measured corrosion current density maps were all taken after 3 h of immersion in the selected corrosion inhibitor environment. The results clearly demonstrate that the addition of 5mM $Ce(NO_3)_3$ inhibitor in 0.05 M NaCl electrolyte slightly decreases the cathodic and anodic corrosion activities in comparison to the reference NaCl solution (Fig. 4.13(d)). With the 1,2,3-benzotriazole the process was even somewhat accelerated. However, the combination of these two inhibitors leads to significantly more efficient corrosion suppression on Al+CFRP couple. Only some hardly detectable electrochemical ionic currents can be seen in Fig. 4.13(e).

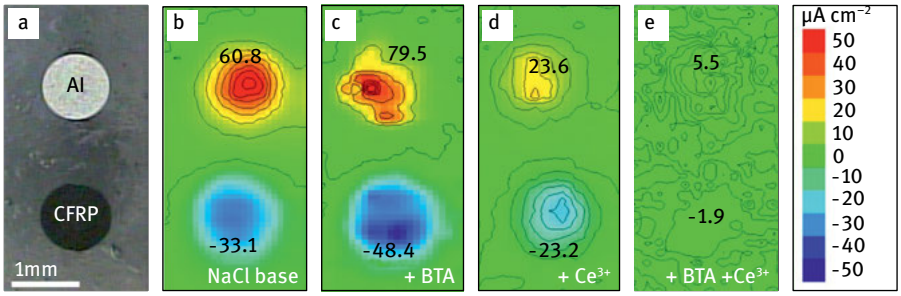

Fig. 4.13: Microphotograph of Al-CFRP galvanic test cell (a), SVET maps taken after 3 h of immersion in different inhibitor solutions with Al and CFRP electrodes electrically coupled in 0.05M NaCl (b), and with addition of inhibitor 5 mM BTA (c), 5 mM $Ce(NO_3)_3$ (d), and the combination of inhibitors 2.5 mM BTA + 2.5 mM $Ce(NO_3)_3$ (e) [48].

With more detailed analysis some additional information about the inhibitor efficiency and functioning kinetics can be also achieved. In Fig. 4.14 the same series of experiments as in Fig. 4.13 is described. The evolution of maximal anodic and cathodic ionic current densities (detected by SVET) is shown. It can be seen that both the anodic and cathodic currents in BTA+Ce^{3+} containing 0.05M NaCl testing medium decrease rapidly during the first hour of immersion and also stay very close to zero during further testing. However, the same inhibitors alone are unable to stop the galvanic corrosion on an Al+CFRP couple.

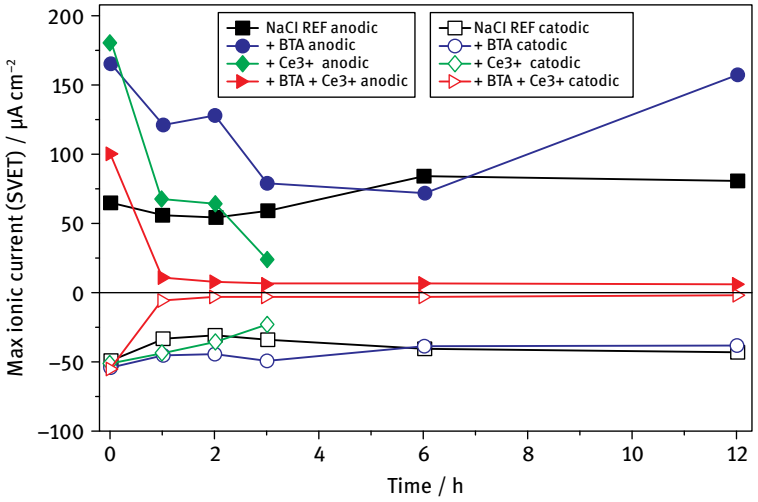

Fig. 4.14: Evolution of anodic and cathodic maximal ionic currents for different corrosion inhibitor systems on Al+CFRP galvanic couple.

Calculation of corrosion inhibition parameters from SVET values

Based on the experimental results several characteristic parameters can be calculated. SVET as a localized technique has been historically mostly applied for qualitative analysis of ionic currents, but with careful experimental set-up and experimental design the qualitative information will be also available. Moreover, especially for studies of galvanic corrosion model systems there are many advantages over the classical electrochemical corrosion rate estimation methods [48, 60, 76, 77].

Maximal anodic and cathodic currents

The SVET measured localised ionic current density values can be an adequate reading of corrosion at a selected measurement location point. Since the results can be presented as three-dimensional spatial localized current maps, the maximal and minimal values over the map usually can point very well to the most active zones. Therefore the maximal anodic ($I_{\max\ AN}$) and maximal cathodic ($I_{\max\ CAT}$) current density values are the first and simplest indicators for the characterisation of corrosion activity at a selected sample.

In the case of a galvanic couple, when the single material corrosion separately from galvanic system does not take place, usually tese values are strictly allocated to the cathode and anode in the reaction cell. Therefore a good characteristic for the whole galvanic couple could be the summarized maximal ionic current density (I_{sum}), which is the sum of the absolute values of cathodic and anodic maxima:

$$\mathrm{I_{sum}} = |\ \mathrm{I_{max\ CAT}}\ | + |\ \mathrm{I_{max\ CAT}}\ |. \tag{4.5}$$

Integrated ionic currents

An advanced approach is the integration of SVET measured ionic currents. As with the scanning of a SVET probe, the ionic current measurement is not continuous, and the map is presented as a raster of current density values the integration of these values presumes the initial differentiation to the real allocated surface area related to each data-point. For a characterization of a galvanic couple the integration of the absolute values will again be the best solution, as it counts both the anodic and cathodic currents for the same system:

$$I_{\text{int}} = \sum_{n=1}^{N} |i_n| \cdot S_n, \tag{4.6}$$

where $|i_n|$ is the absolute value of the SVET current density measured at point n (at a certain distance from the surface (usually 100–200 µm)), S_n is the surface area (cm^2) corresponding to a single measurement point, and N is the total number of data points included in the calculation.

Inhibition efficiency (*IE*)

The parameter for estimating the inhibition efficiency can be found as

$$IE = \frac{CR_0 - CR_{\text{inh}}}{CR_0}, \tag{4.7}$$

where CR_0 is the corrosion rate in the noninhibited medium and CR_{inh} is the corrosion rate in the presence of inhibitor. In the case of the SVET data the I_{sum} and I_{int} are proportional to the corrosion rate.

Synergistic parameter (*S*)

The parameter that numerically expresses the synergistic effect of two corrosion inhibitors can be found as suggested by Aramaki and Hackerman [78]:

$$S = \frac{1 - IE_{1+2}}{1 - IE_{12}}, \tag{4.8}$$

where:

$$IE_{1+2} = (IE_1 + IE_2) - (IE_1 \cdot IE_2). \tag{4.9}$$

The parameters IE_1, IE_2 and IE_{12} are the calculated inhibition efficiencies for inhibitors 1, 2, and the mixture of 1 and 2, respectively. The values $S > 1$ indicate the synergistic behavior of a selected inhibitor combination, while $S = 1$ refers simply to the additive effect of inhibitors, and $S < 1$ is the case with antagonistic behavior of selected inhibitors.

Calculation results for selected corrosion inhibitor mixtures

For an Al+CFRP galvanic system the inhibition efficiencies (*IE*) and synergistic parameter (*S*) were calculated on the basis of the sums of maximal (I_{sum}) and integrated (I^{int}) ionic currents, as presented in Table 4.1. The difference between the two calculation approaches can be noticed, while the parameters S (8.48) and S^{int} (2.77) are slightly varied. However, as the values are clearly higher than unity (S >1) in both cases, the evidence of the synergistic cooperation of Ce^{3+} and BTA on an Al+CFRP couple in NaCl corrosive media is proved.

Calculations based on maximal SVET detected signal can be overestimated due to the unevenly distributed corrosion activities on the surface, which can result in multiple current maxima, as was noticed also in Fig. 4.13(c). It shows that the comparison of parameters from these two approaches could also give some additional information about the grade of corrosion localization (possible pitting activities, for example), because in that case the multiple peak maxima can result in proportionally lower input parameters for calculation, while the integrated current values are obviously closer to the real situation.

An important factor to be taken into account when finding the synergistic inhibiting mixtures is the concentration ratio between the components. The identification

Tab. 4.1: Calculated inhibition efficiencies (*IE*) and synergistic parameter (*S*) for Al+CFRP galvanic couple using maximal (I_{sum}, *IE*, *S*) and integrated (I^{int}, IE^{int}, S^{int}) ionic current values [48]

Al+CFRP						
Solution	**I_{sum}/μA cm^{-2}**	**IE**	**S**	**I^{int}/mA cm^{-2}**	**IE^{int}**	**S^{int}**
Base solution NaCl	93.8	–		15.1	–	
+ BTA	127.9	– 0.36	8.48	12.1	0.197	2.77
+ $Ce(NO_3)_3$	46.8	0.50		5.78	0.617	
+ $Ce(NO_3)_3$+ BTA	7.5	0.92		1.67	0.889	

of inhibitor synergy and the characterization of many variables that affect inhibitor performance (e.g., concentration, pH, T, etc.) cannot be predicted and must be determined experimentally. The influence of concentration on the synergistic effect of two inhibitors can even lead to the situation when an antagonism is observed, as demonstrated below (Fig. 4.15).

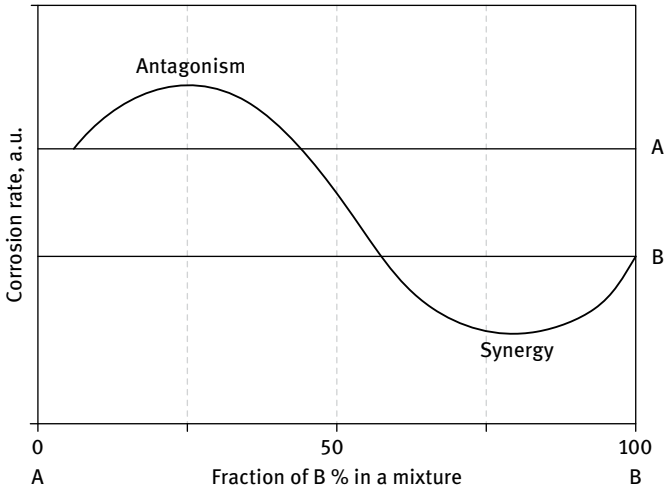

Fig. 4.15: Schematics representation of metal corrosion rate versus composition of a binary inhibitor system (A:B) at a fixed pH (adapted from [14]).

Step 2. Encapsulation of corrosion inhibitors

After the efficient corrosion inhibitors or synergistic mixtures of inhibiting compounds are found, the next important step is the introduction of the inhibitors into the real protective system. The direct addition of inhibitors in polymer formulations often leads to adverse effects, as mentioned above [79, 80]. Moreover, the release of inhibitors in such cases is hard to control, which can be critical for synergistic mixtures since an unfavorable concentration ratio between two components can be achieved. The

synergism can become an antagonism in such a situation. This is the stage when the application of nanomaterials can be a way to offer a solution. The encapsulation of corrosion inhibitors in the form of nanocontainers can reduce the adverse effects on polymer matrix and ensure a controllable release on demand. In this particular example two types of functional nanocontainers were selected: layered double hydroxide (LDH) and bentonite as functional cationic and anionic ion exchangers, respectively. These nanoclay-based containers could confer a controllable delivery and functional release of inhibitors by appearance of corrosion related species like Cl^- or OH^- in the case of LDH [81, 82] and Me^{n+} for bentonite [45].

Layered double hydroxides

Layered double hydroxides are known as hydrotalcite-like anion exchangers [81, 82]. This compound is formed with a layer-by-layer structure. Between two positively charged layers of metallic cations/hydroxides there are negatively charged layers of anions. Using the LDH capability for anionic exchange of some corrosion inhibitors, like 2-mercaptobenzothialzole (MBT) or BTA, it could be incorporated into the structure in anionic form (Fig. 4.16).

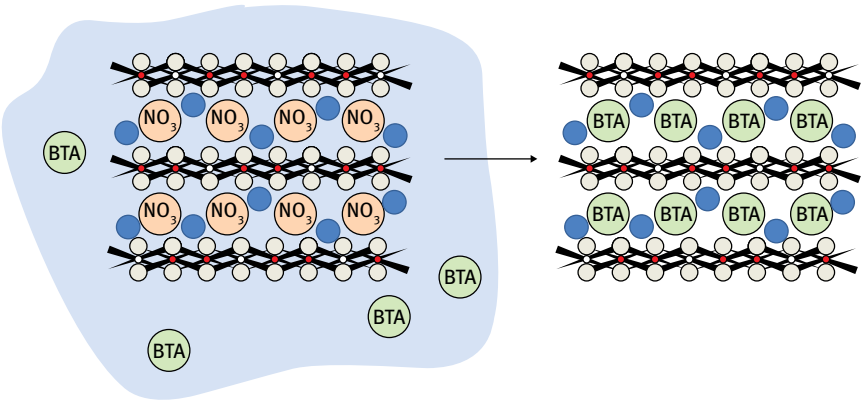

Fig. 4.16: The intercalation of the anticorrosion inhibitor (BTA) into the structure of LDH.

When LDH is loaded with inhibitors and inserted into a protective coating structure, it is supposed to be placed near a metallic surface. When corrosion of the substrate occurs the formation of hydroxides begins concurrently. Then the anion-exchange capability of LDH is used again, as previously intercalated inhibitors can be replaced with cathodically formed corrosion products (OH^-), or even by invading corrosion agent e.g. Cl^- (Fig. 4.17).

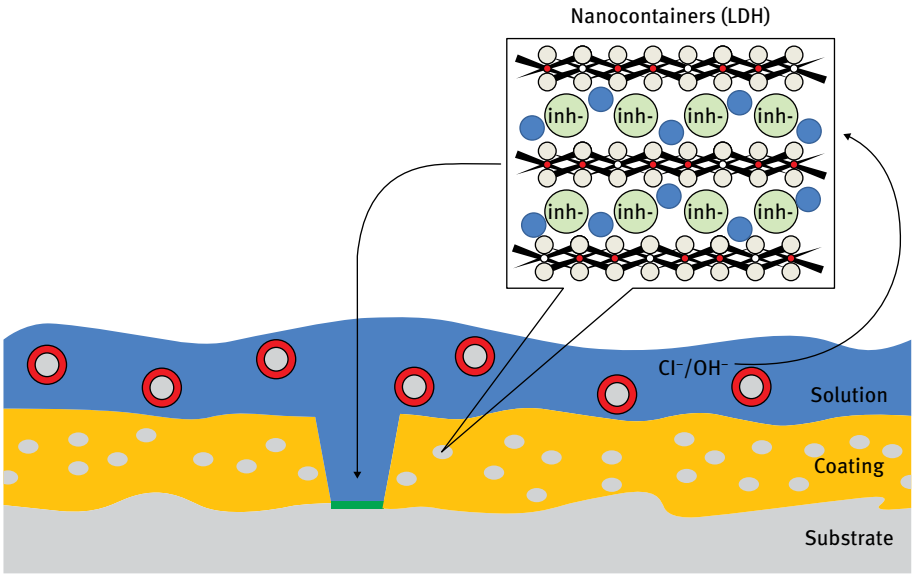

Fig. 4.17: Anion exchange reaction occurred with LDHs during corrosion protection mechanism in active self-healing coating [83].

This leads to the main advantages of LDH use: (1) the controlled release of the inhibitor, and (2) the absorption of chlorides, whose presence is critical for the corrosion processes.

Bentonite

Bentonite is a natural clay mineral that can be used as a cation exchanger. It consists of negatively charged alumosilicate sheets, between which the inhibiting cations can be intercalated [45] (Fig. 4.18).

The release of the initially incorporated Ce^{3+} inhibitor can be triggered by metal cations which are available in the locations of anodic corrosion process.

Step 3. Application of multifunctional coating

The next important stage is the introduction of encapsulated inhibitors into the polymer formulation. The dispersion of nanocontainers can be an issue. Bad dispensability can cause formation of agglomerates, which in turn negatively affects the barrier properties of the coating. In this particular example bicomponent epoxy resin [48] was used as a coating formulation. Fortunately the dispersion of the nanocontainers was reasonably good, and no further surface modification was needed. The obtained nanocontainer-containing polymer formulation can then be applied using different

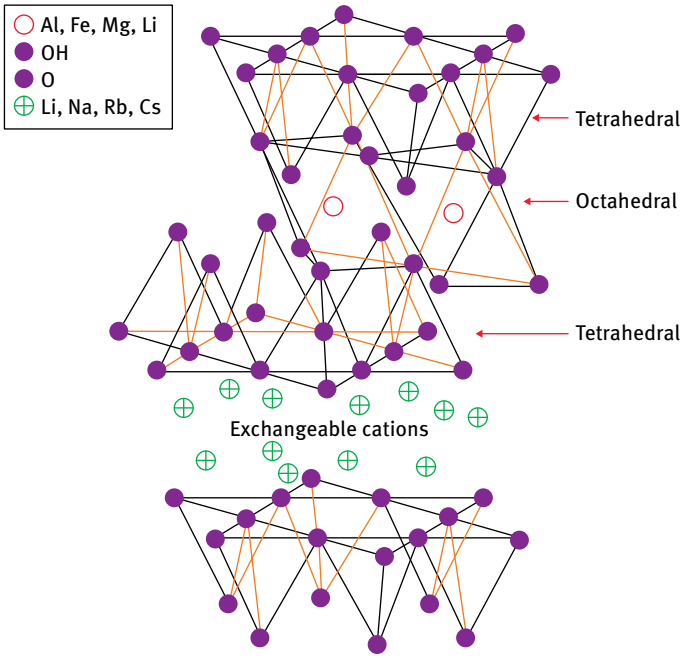

Fig. 4.18: Bentonite structure (adopted from [84]).

appropriate techniques in order to get a uniform nanocomposite coating. The formulation with 2 wt.% of nanocontainers was created. The coating to be tested was applied by a spiral bar coater with 40 µm wet coating thickness on top of a model galvanically connected Al+CFRP planar substrate [48].

Step 4. Verification of active protection

The active protection functionality has to be verified after the coating is developed for a specific multimaterial combination. One of the possibilities is to create artificial defects in the coating and observe the kinetics of corrosion processes in these local zones. The systematic localized corrosion monitoring approach with SVET has been applied to monitor corrosion protection properties of nanocontainers impregnated coating. The self-healing ability was tested at artificially induced needle defects, each located on both sides of an AA6061+CFRP galvanic couple (Fig. 4.19(a)). The area beyond the scan was isolated by wax to exclude any possibility of uncounted electrochemical activities, and the ionic current densities were monitored for up to 24 h of immersion in 0.05 M NaCl corrosive medium (Fig. 4.19).

The typical SVET maps obtained in the case of two coatings, the blank one (Fig. 4.19(c)) and the one containing a combination of nanocontainers (Fig. 4.19(d)) are presented. It can be seen that the anodic and cathodic activities are well defined

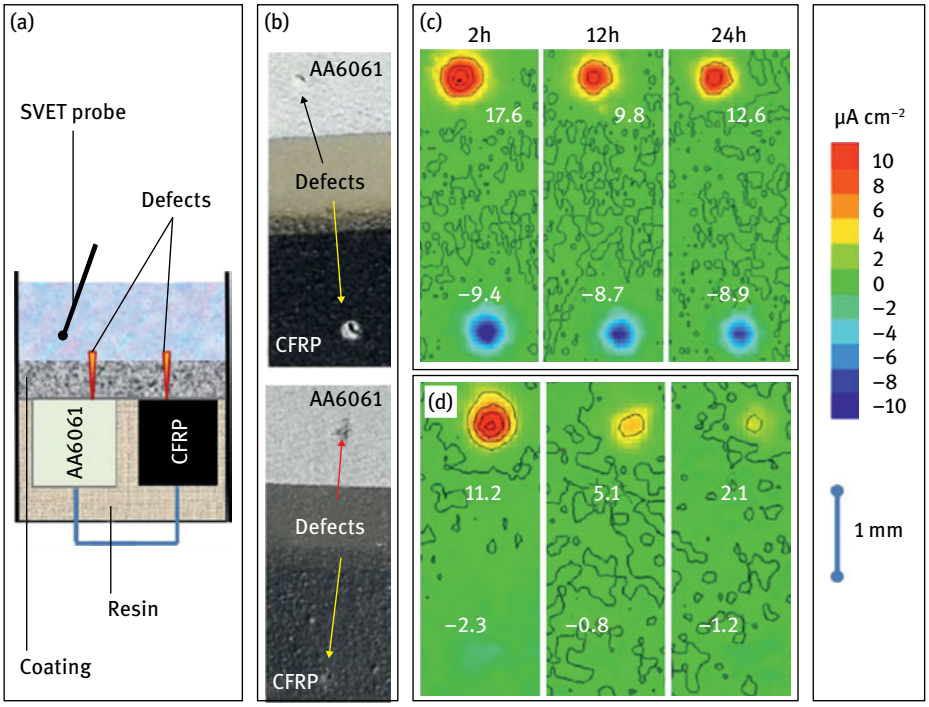

Fig. 4.19: Schema of AA6061+CFRP microelectrode setup (a), microphotographs of coated galvanic model-cell (b). The SVET maps for the sample with blank epoxy coating (c) and for the coating loaded with combination of nanocontainers (LDH-BTA + bentonite-Ce^{3+}) (d) obtained after 2 h, 12 h and 24 h of immersion in 0.05 M NaCl [48].

and located strictly at the artificial defect zones over AA6061 and CFRP, in both cases at the beginning of immersion. The blank system demonstrates relatively stable values of corrosion currents in the defects, while in contrast a well-defined self-healing effect is observed in the case of the nanocontainer impregnated coating. The activity at the defect zones significantly decreased with time.

The average stabilized values of the anodic and cathodic ionic current densities at the defect zones observed between 15 h and 24 h of immersion are presented in Table 4.2. The system doped with LDH-BTA nanocontainers shows somewhat lower activity than the blank coating, while the coating with Ce^{3+}-bentonite demonstrates even a slight increase of corrosion activity in the defect zones. The increase of activity can be related to a negative impact of the Ce-containing pigment on the barrier properties of the coating, which is a commonly observed phenomenon [34].

Additionally the coated AA6061+CFRP galvanic cells were inspected during their immersion in 0.5M NaCl in respect to the appearance of visible evidence of corrosion products or defects. In Table 4.2 the elapsed times without visible signs of corrosion (*no corrosion*) are also reported. It can be seen that the blank reference coating

Tab. 4.2: Time of immersion before appearance of visible corrosion defects (*No corrosion*) and SVET parameters (anodic (I_{AN}) and cathodic (I_{CAT})) for AA6061+CFRP model substrates with coating [48].

AA6061+CFRP with coating			
Sample	**No corrosion / h**	**I_{AN}/µA cm^{-2}**	**I_{CAT}/µA cm^{-2}**
Blank coating	12	12±1	– 8.9±0.5
+ **Mg(2)Al-BTA**	192	5.4±0.4	– 8.5±0.7
+ **Bentonite-Ce^{3+}**	48	14.7±1.3	– 9.8±0.7
+ **Mg(2)Al-BTA + Bentonite-Ce^{3+}**	408	2.1±0.2	– 1.1±0.1

rapidly degraded during the first 12 h, while the coating doped with the combination of nanocontainers demonstrated the highest corrosion resistance: 408 hours until visible deterioration. This also clearly exceeds the coatings doped with only BTA^- or Ce^{3+}-loaded nanocontainers, which showed corrosion signs already after 192 h and 48 h, respectively.

The observed self-healing effect can be clearly correlated to the synergistic inhibition effect of the mixture of cerium cations and benzotriazole released from bentonite and LDH, respectively.

4.3 Concluding remarks

The brief overview presented in this chapter demonstrates that galvanic compatibility is an issue which can significantly shorten the life of hybrid multimaterial structures and can lead to unexpected premature failures. The design of structures, the correct choice of joining methods, and the selection of proper materials can reduce the risk of galvanic corrosion. Currently many technological solutions in the directions discussed have been developed to cope with this issue. However, most of these solutions assume the additional application of different sealing or coating strategies in order to limit the interaction of joined materials with moisture and corrosion agents coming from the environment.

The coating technologies applied for single materials are being intensively transferred to the hybrid structures, although with many complications and important limitations. The compatibility of the surface treatment process developed for one material can be absolutely incompatible with another material in a hybrid structure. The new path is to develop new surface treatment processes which can be applicable to multimaterial substrates. This can drastically improve the economical perspectives for multimaterial designs, especially in the automotive industry. However, passive protection relying only on the barrier properties of sealants and coatings cannot be considered as a final reliable solution. Different types of defects can appear during exploitation leading to the degradation of barrier properties and unpredictable corrosion of joined structure in such zones.

The introduction of an active protection concept via the incorporation of "smart" nanocontainers into protective coatings or sealants seems to be a promising approach which allows control over the galvanic corrosion processes in multimaterial structures. The novel nanocomposite coatings can effectively respond to any change of environment or to the beginning of corrosion processes by the release of corrosion inhibitors on demand, supressing the corrosion activities. The same approaches based on active inhibitor-loaded nanocontainers can also be used in sealants and adhesives.

The development of such "smart" protective nanocoatings for multimaterial assemblies is a multistep process which should follow a certain procedure in order to achieve a desirable performance. At the first stage the mechanisms and the conditions associated with the galvanic corrosion processes in a specific assembly should be understood. Later the efficient corrosion inhibitors should be selected for each particular case. The minimal and maximal concentration of the inhibitors as well as potential synergistic combinations should be explored. The use of synergistic mixtures can ensure more efficient active protection even with lower inhibitor concentrations. The inhibitors in most cases have to be encapsulated. Usually the functional nanocontainers are preferable to microreservoirs, especially in the case of thin coatings where the distribution of such pigments can be critical. The integration of nanocontainers into the protective system is another challenge, and often some additional surface modifications of nanoadditives have to be performed in order to ensure good compatibility. After completing all of these steps, it is possible to have a powerful tool for the design of an active protective strategy for a multimaterial structure. The advantage of such an approach is that active elements can be combined in different ways in order to ensure a reliable protection for a wide range of material combinations. Ideally, one multicomponent active protection scheme can be applied for multimaterial structure such as a complex car body.

Acknowledgements

The European FP7 projects "PROAIR" (PIAPP-GA-2013-612415), "MUST" (NMP3-LA-2008-214261) as well as the projects PTDC/CTM/108446/2008, IF/00856/2013, and SFRH/BPD/64580/2009 (FCT, Portugal) are gratefully acknowledged.

References

[1] Airbus to start manufacturing parts for new A350 XWB in late '09. Eng. News Online. 11 Mai 2009.

[2] Lohner H, Fangmeier A. 2013. *Alloy Corrosion Modelling as Applied in the Aviation Industry in Aluminium Alloy Corrosion of Aircraft Structures: Modelling and Simulation,* Southampton, WIT Press, 13–21.

[3] Peng Z, 2013. Nie X. Galvanic corrosion property of contacts between carbon fiber cloth materials and typical metal alloys in an aggressive environment. Proc. 39th Int. Conf. Metall. Coat Thin Films ICMCTF ICMCTF 2012. Proc. 39th Int. Conf. Metall Coat Thin Films ICMCTF, 215, 85–89.
[4] Fovet Y, Pourreyron L, Gal JY. 2000. Corrosion by galvanic coupling between carbon fiber posts and different alloys, *Dent. Mater.* **16**(5)„ 364–3736.
[5] Palani S, Hack T, Peratta A, Adey R, Baynham J, Lohner H. Modeling Approach for Galvanic Corrosion Protection of Multimaterial Aircraft Structures. Available from: http://www.beasy.com/galvanic-corrosion/galvanic-corrosion-publications.html
[6] Jia JX, Atrens A, Song G, Muster TH. 2005. Simulation of galvanic corrosion of magnesium coupled to a steel fastener in NaCI solution, *Mater. Corros.* **56**(7), 468–74.
[7] Skar JI. 1999. Corrosion and corrosion prevention of magnesium alloys. *Mater. Corros.* **50**(1), 2–6.
[8] Blawert C, Hort N, Kainer KU. 2004. Automotive applications of magnesium and its alloys, *Trans. Indian Inst. Met.* **57**(4), 397–408.
[9] Skar JI, Albright D. 2002. Emerging trends in corrosion protection of magnesium die-castings from Essential readings in magnesium technology, John Wiley&Sons Inc., New Jersey, 585–592.
[10] Boese E, Göllner J, Heyn A, Strunz J, Baierl C, Schreckenberger H. 2001. Kontaktkorrosion einer Magnesiumlegierung mit beschichteten Bauteilen, *Mater. Corros.* **52**(4), 247–256.
[11] Palani S, Hack T, Deconinck J, Lohner H. 2014. Validation of predictive model for galvanic corrosion under thin electrolyte layers: An application to aluminum 2024-CFRP material combination, *Corros. Sci.* **78**, 89–100.
[12] Wloka J, Laukant H, Glatzel U, Virtanen S. 2007. Corrosion properties of laser beam joints of aluminum with zinc-coated steel, *Corros Sci.* **49**(11), 4243–4258.
[13] Jia JX, Song G, Atrens A. 2006. Influence of geometry on galvanic corrosion of AZ91D coupled to steel, *Corros. Sci.* **48**(8)„ 2133–2153.
[14] Chambers BD, Taylor SR, Kendig MW. 2005. Rapid Discovery of Corrosion Inhibitors and Synergistic Combinations Using High-Throughput Screening Methods. *Corrosion*, **61**(5), 480–488.
[15] Muster TH, Hughes AE, Furman SA, Harvey T, Sherman N, Hardin S, et al. 2009. A rapid screening multi-electrode method for the evaluation of corrosion inhibitors, *Electrochimica Acta* **54**(12), 3402–3411.
[16] Blüh O, Scott B. 1950. Vibrating probe electrometer for the measurement of bioelectric potentials, *Rev. Sci. Instrum.* **21**(10), 867–868.
[17] Jaffe LF, Nuccitelli R. 1974. An ultrasensitive vibrating probe for measuring steady extracellular currents, *J. Cell Biol.* **63**(2), 614–28.
[18] Scheffey C. 1988. Two approaches to construction of vibrating probes for electrical current measurement in solution, *Rev. Sci. Instrum.* **59**, 787–792.
[19] Somieski P, Nagel W. 1998. Localizing transepithelial conductive pathways using a vibrating voltage probe, *J. Exp. Biol.* **201**(17), 2489–8495.
[20] Isaacs HS, Kissel G. 1972. Surface preparation and pit propagation in stainless steels, J. Electrochem. Soc. **119**(12), 1628–1632.
[21] Isaacs HS. 1988. The measurement of the galvanic corrosion of soldered copper using the scanning vibrating electrode technique, *Corros. Sci.* **28**(6), 547–558.
[22] Ogle K, Baudu V, Garrigues L, Philippe X. 2000. Localized Electrochemical Methods Applied to Cut Edge Corrosion, *J. Electrochem. Soc.* **147**(10), 3654–3660.
[23] Battocchi D, He J, Bierwagen GP, Tallman DE. 2005. Emulation and study of the corrosion behavior of Al alloy 2024-T3 using a wire beam electrode (WBE) in conjunction with scanning vibrating electrode technique (SVET), *Corros. Sci.*, **47**(5), 1165–1176.

[24] Hack T, Palani S. 2013. Method And Device For Forming An Electrolyte Film On An Electrode Surface, US 20130280416 A1.
[25] Blawert C, Heitmamm V, Höche D, Kainer KU. 2010 Design of hybrid Mg/Al components for the automotive body – Preventing general and galvanic corrosion, Conf. Proc. IMA 67th Annual World Magnesium Conference, Hong Kong.
[26] Schreckenberger H, Papke M, Eisenberg S. 2000. The Magnesium Hatchback of the 3-Liter Car: Processing and Corrosion Protection, SAE Tech. Pap. 2000-01-1123.
[27] Baron-Wiecheć A, Curioni M, Arrabal R, Matykina E, Skeldon P, Thompson GE. 2013. Plasma electrolytic oxidation of coupled light metals, *Trans. IMF* **91**(2), 107–112.
[28] Koudelkova M, Augustynski J, Berthou H. 1977 On the Composition of the Passivating Films Formed on Aluminum in Chromate Solutions, *J. Electrochem. Soc.* **124**(8), 1165–1168.
[29] Brown GM, Shimizu K, Kobayashi K, Thompson GE, Wood GC. 1993. The development of chemical conversion coatings on aluminum, Adv. Corros. Prot. Proc. Int. Conf. Mark. 20th Anniv. UMIST *Corros. Prot. Cent.* **35**(1–4), 253–256.
[30] Kumara A, Stephenson LD, Murray JN. 2006. Self-healing coatings for steel, *Prog. Org. Coat.* **55**, 244–253.
[31] Sauvant-Moynot V, Gonzalez S, Kittel J. 2008. Self-healing coatings: An alternative route for anticorrosion protection, *Prog. Org. Coat.* **63**(3), 307–315.
[32] Jorcin J-B, Scheltjens G, Van Ingelgem Y, Tourwé E, Van Assche G, De Graeve I, et al. 2010. Investigation of the self-healing properties of shape memory polyurethane coatings with the 'odd random phase multisine' electrochemical impedance spectroscopy, IMPEDANCE. *Spectrosc. Transf. Funct.* **55**(21), 6195–6203.
[33] Trabelsi W, Cecilio P, Ferreira MGS, Montemor MF. 2005. Electrochemical assessment of the self-healing properties of Ce-doped silane solutions for the pre-treatment of galvanised steel substrates, *Prog. Org. Coat.* **54**(4), 276–284.
[34] Zheludkevich ML, Serra R, Montemor MF, Yasakau KA, Salvado IMM, Ferreira MGS. 2005. Nanostructured sol–gel coatings doped with cerium nitrate as pre-treatments for AA2024-T3: Corrosion protection performance, *Electrochimica Acta* **51**(2)„ 208–217.
[35] Rosero-Navarro NC, Pellice SA, Durán A, Aparicio M. 2008 Effects of Ce-containing sol–gel coatings reinforced with SiO2 nanoparticles on the protection of AA2024, *Corros. Sci.* **50**(5), 1283–1291.
[36] Palanivel V, Huang Y, van Ooij WJ. 2005. Effects of addition of corrosion inhibitors to silane films on the performance of AA2024-T3 in a 0.5 M NaCl solution, *Prog. Org. Coat.* **53**(2), 153–168.
[37] Shchukin DG, Zheludkevich ML, Yasakau KA, Lamaka SV, Ferreira MGS, Mohwald H. 2006. Layer-by-Layer Assembled Nanocontainers for Self-Healing Corrosion Protection, *Adv. Mater.* **18**(13), 1672–1678.
[38] Sinko J. 2001. Challenges of chromate inhibitor pigments replacement in organic coatings, *Prog. Org. Coat.* **42**(3–4)„ 267–282.
[39] Shchukin DG, Mohwald H. 2007. Self-repairing coatings containing active nanoreservoirs, *Small.* **3**(6), 926–943.
[40] White SR, Sottos NR, Geubelle PH, Moore JS, Kessler MR, Sriram SR. et al. 2001. Autonomic healing of polymer composites, *Nature* **409**(6822), 794–797.
[41] Snihirova D, Lamaka SV, Taryba MG, Salak AN, Kallip S, Zheludkevich ML, et al. 2010. Hydroxyapatite microparticles as feedback-active reservoirs of corrosion inhibitors, *ACS Appl. Mater. Interfaces* **2**(11), 3011–3022.
[42] Yang H, van Ooij W. 2003. Plasma Deposition of Polymeric Thin Films on Organic Corrosion-Inhibiting Paint Pigments: A Novel Method to Achieve Slow Release, *Plasmas Polym.* **8**(4), 297–323.
[43] Lammerschop O, Roth M. 2002 Silicate particles, Ger. Petent 10064638 A1.

[44] Buchheit RG, Guan H, Mahajanam S, Wong F. 2003. Active corrosion protection and corrosion sensing in chromate-free organic coatings, *Keyst.* **47**(3–4), 174–182.
[45] Bohm S, McMurray HN, Worsley DA, Powell SM. 2001. Novel environment friendly corrosion inhibitor pigments based on naturally occurring clay minerals, *Mater. Corros.* **52**(12), 896–903.
[46] Zheludkevich ML, Poznyak SK, Rodrigues LM, Raps D, Hack T, Dick LF, et al. 2010. Active protection coatings with layered double hydroxide nanocontainers of corrosion inhibitor, *Corros. Sci.* **52**(2), 602–611.
[47] Maia F, Tedim J, Lisenkov AD, Salak AN, Zheludkevich ML, Ferreira MGS. 2012. Silica nanocontainers for active corrosion protection, *Nanoscale* **4**(4), 1287–1298.
[48] Serdechnova M, Kallip S, Ferreira MGS, Zheludkevich ML. 2014. Active self-healing coating for galvanically coupled multi-material assemblies, *Electrochem. Commun.* **41**, 51–54.
[49] Forsyth M, Markley T, Ho D, Deacon GB, Junk P, Hinton B, et al. 2008. Inhibition of Corrosion on AA2024-T3 by New Environmentally Friendly Rare Earth Organophosphate Compounds, *Corrosion* **64**(3), 191–197.
[50] Markley TA, Hughes AE, Ang TC, Deacon GB, Junk P, Forsyth M. 2007. Synergistic corrosion inhibition in mixed rare-earth diphenyl phosphate systems, Electrochem. *Solid-State Lett.* **10**(12), C72–C75.
[51] Catubig R, Hughes AE, Cole IS, Hinton BRW, Forsyth M. 2014. The use of cerium and praseodymium mercaptoacetate as thiol-containing inhibitors for AA2024-T3, *Corros. Sci.* **81**, 45–53.
[52] Shi H, Han E-H, Liu F. 2011. Corrosion protection of aluminum alloy 2024-T3 in 0.05 M NaCl by cerium cinnamate, *Corros. Sci.* **53**(7), 2374–2384.
[53] Yasakau KA, Tedim J, Zheludkevich ML, Drumm R, Shem M, Wittmar M, et al. 2012. Cerium molybdate nanowires for active corrosion protection of aluminum alloys, *Corros. Sci.* **58**, 41–51.
[54] Yasakau KA, Kallip S, Zheludkevich ML, Ferreira MGS. 2013. Active corrosion protection of AA2024 by sol-gel coatings with cerium molybdate nanowires, *Electrochimica Acta* **112**, 236–246.
[55] Ferrer EL, Rollon AP, Mendoza HD, Lafont U, Garcia SJ. 2014. Double-doped zeolites for corrosion protection of aluminum alloys, *Microporous Mesoporous Mater.* **188**, 8–15.
[56] Roberge PR. 2000. *Handbook of Corrosion Engineering*, Martinsburg, McGraw-Hill.
[57] Yasakau KA, Zheludkevich ML, Lamaka SV, Ferreira MGS. 2006. Mechanism of corrosion inhibition of AA2024 by rare-earth compounds, *J. Phys. Chem. B.* **110**(11), 5515–5528.
[58] Serdechnova M, Volovitch P, Brisset F, Ogle K. 2014. On the cathodic dissolution of Al and Al alloys, *Electrochimica Acta* **124**, 9–16.
[59] Vargel C, Jacques M, Schmidt MP. 2004. Chapter B.5 – Protection Against Corrosion, in C. V. J. P. Schmidt (ed.), *Corrosion of Aluminium*, Amsterdam, Elsevier, 185–207.
[60] Kallip S, Bastos AC, Yasakau KA, Zheludkevich ML, Ferreira MGS. 2012. Synergistic corrosion inhibition on galvanically coupled metallic materials, Electrochem. Commun. **20**, 101–104.
[61] Finšgar M, Milošev I. 2010. Inhibition of copper corrosion by 1,2,3-benzotriazole: A review, *Corros. Sci.* **52**(9), 2737–2749.
[62] El-Taib Heakal F, Haruyama S. 1980. Impedance studies of the inhibitive effect of benzotriazole on the corrosion of copper in sodium chloride medium, *Corros. Sci.* **20**(7), 887–898.
[63] Fang B-S, Olson CG, Lynch DW. 1986. A photoemission study of benzotriazole on clean copper and cuprous oxide, *Surf. Sci.* **176**(3), 476–490.
[64] Leroy RL. 1978. Chelate Inhibitors for Zinc and Galvanized Products, *Corrosion* **34**(3), 98–110.
[65] Müller B, Imblo G. 1996. Heterocycles as corrosion inhibitors for zinc pigments in aqueous alkaline media, *Corros. Sci.* **38**(2), 293–300.

[66] Aramaki K. 2001. Effects of organic inhibitors on corrosion of zinc in an aerated 0.5 M NaCl solution, *Corros. Sci.* **43**(10), 1985–2000.
[67] Yao JL, Ren B, Huang ZF, Cao PG, Gu RA, Tian Z-Q. 2003. Extending surface Raman spectroscopy to transition metals for practical applications IV. A study on corrosion inhibition of benzotriazole on bare Fe electrodes, *Microsc. Nanoscopi.c Asp. Corros. Corros. Prot.* **48**(9), 1263–1271.
[68] Fleischmann M, Hill IR, Mengoli G, Musiani MM. 1983. The synergetic effect of benzylamine on the corrosion inhibition of copper by benzotriazole, *Electrochimica Acta* **28**(10), 1325–1333.
[69] Villamil RFV, Corio P, Agostinho SML, Rubim JC. 1999. Effect of sodium dodecylsulfate on copper corrosion in sulfuric acid media in the absence and presence of benzotriazole, *J. Electroanal. Chem.* **472**(2), 112–119.
[70] Wu YC, Zhang P, Pickering HW, Allara DL. 1993. Effect of KIf KIt oglleium dodecylsulfate on copper corrosion in sulfuric acid mediaSulfuric Acid Electrolytes, *J. Electrochem. Soc.* **140**(10), 2791–2800.
[71] Hinton BRW, Arnott DR, Ryan NE. 1984. The inhibition of aluminum alloy corrosion by cerous cations, *Met. Forum* **7**, 211–217.
[72] Wan J, Thompson GE, Ng TK, Lu KQ, Smith CJE. 1997. XANES Study of Ce and Mo Containing Conversion Coatings on Aluminium, *J. Phys. IV Fr.* **7**, 1181–1184.
[73] Aldykiewicz AJ, Davenport AJ, Isaacs HS. 1996. Studies of the Formation of Cerium-Rich Protective Films Using X-Ray Absorption Near-Edge Spectroscopy and Rotating Disk Electrode Methods, *J. Electrochem. Soc.* **143**(1), 147–154.
[74] Yasakau KA, Zheludkevich ML, Ferreira MGS. 2008. Lanthanide Salts as Corrosion Inhibitors for AA5083. Mechanism and Efficiency of Corrosion Inhibition, *J. Electrochem. Soc.* **155**(5), C169–C177.
[75] Davis JR. 1993 Aluminum and Aluminum Alloys, ASM International.
[76] Kallip S, Bastos AC, Zheludkevich ML, Ferreira MGS. 2010. A multi-electrode cell for high-throughput SVET screening of corrosion inhibitors, *Corros. Sci.* **52**(9), 3146–3149.
[77] Bastos AC, Zheludkevich ML, Ferreira MGS. 2008. A SVET investigation on the modification of zinc dust reactivity. Workshop, *Appl. Electrochem. Tech. Org. Coat.* **63**(3), 282–290.
[78] Aramaki Hackerman K N. 1969. Inhibition mechanism of medium-sized polymethyleneimine, *J. Electrochem. Soc.* **116**, 568.
[79] Zheludkevich ML, Tedim J, Ferreira MGS. 2010. “Smart” coatings for active corrosion protection based on multi-functional micro and nanocontainers, *Electrochem. Front. Glob. Environ. Energy* **82**, 314–323.
[80] Zheludkevich ML. 2008. Self-healing anticorrosion coatings, Self-Heal. Mater. Fundam. Des. Strateg. Appl., Weinheim, Wiley-VCH, 101–139.
[81] Poznyak SK, Tedim J, Rodrigues LM, Salak AN, Zheludkevich ML, Dick LF, et al. 2009. Novel Inorganic Host Layered Double Hydroxides Intercalated with Guest Organic Inhibitors for Anticorrosion Applications, *ACS Appl. Mater. Interfaces* **1**(10), 2353–2362.
[82] Williams G, McMurray HN. 2004. Inhibition of Filiform Corrosion on Polymer Coated AA2024-T3 by Hydrotalcite-Like Pigments Incorporating Organic Anions, *Electrochem. Solid-State Lett.* **7**(5), B13–B15.
[83] Vieira DEL. 2014. Active protective treatments for galvanically coupled AA2024 and CFRP, master’s thesis, Aveiro (Portugal).
[84] Beyer G. 2002. Nanocomposites: a new class of flame retardants for polymers, *Plast. Addit. Compd.* **4**, 22–8.

M. Konstantakopoulou, A. Deligianni, and G. Kotsikos

5 Failure of dissimilar material bonded joints

Abstract: Joining of materials in structural design has always been a challenge for engineers. Bolting and riveting has been used for many years, until the emergence of fusion welding which revolutionised construction in areas such as shipbuilding, automotive, infrastructure and consumer goods. Extensive research in the past 50 years has resulted in better understanding of the process and minimised the occurrence of failures associated with fusion welding such as, residual stress cracking, stress corrosion and corrosion fatigue cracking, localised reduction in mechanical properties due to microstructural changes (heat affected zone) etc. Bonding has been a technique that has been proposed as an alternative because it eliminates several of the problems associated with fusion welding. But, despite some applications it has not seen wide use. There is however a renewed interest in adhesively bonded joints, as designers look for ever more efficient structures which inevitably leads to the use and consequently joining of combinations of lightweight materials, often with fundamentally different mechanical and physical properties. This chapter provides a review of adhesively bonded joints and reports on improvements to bonded joint strength through the introduction of carbon nanotubes at the bond interface. Results from various workers in the field are reported as well as the findings of the authors in this area of research. It is obvious that there are several challenges that need to be addressed to further enhance the strength of bonded joints and worldwide research is currently underway to address those shortcomings and build confidence in the implementation of these new techniques.

5.1 Introduction

Hybrid structures consisting of two or more dissimilar materials with fundamentally different mechanical, thermal, and physical properties are increasingly making inroads in structural design, as it is the only way of pushing the boundaries in terms of lightweighting and functionality that would not be possible with structures made of a single material.

A fundamental aspect of this approach is the ability to join effectively such materials to achieve a smooth transfer of service loads from one material to the other. The joining of any two materials requires the presence of an “interface” that adheres strongly to both materials to be joined so as to transfer effectively the load between the two components. This “interface” can have many forms, depending on the physical properties of the materials to be joined. A “welded” joint is produced by input of heat to melt the material while simultaneously mixing in the molten material pool a third material in the form of wire (normally called “filler wire”) that provides the intermediate phase for joining of the two materials.

Due to the different chemical, mechanical, and thermal behaviors of materials in hybrid structures, joining presents challenges significantly different than those for similar materials.

Bonding, bolting, and riveting have traditionally been the methods used for joining dissimilar materials. Although all techniques have been used in the past, adhesive bonding is considered the most efficient method, because it is the most lightweight solution, it removes the stress raising effect of pins/rivets, it removes the possibility of loosening of the joint due to vibration or compressive creep (for some materials), and achieves a smooth transfer of stress from one material to the other. In addition, the composition and properties of the region adjacent to the interface must be tailored in such a way as to achieve an efficient and smooth transfer of stress without giving rise to zones with high peel or shear stresses. This chapter will therefore concentrate on the mechanical performance of adhesively bonded joints.

5.1.1 Adhesively bonded joints

"Adhesive bonding" was introduced into structural design approximately 70 years ago, starting with metal/wood bonding in aircraft (phenolic resin, UK) and metal/metal bonding (epoxy resin, Germany) in the early 1940s, which allowed more flexibility in structural lightweight design. In the late 1960s rubber-like, hyperelastic polyurethane adhesives were first used for bonding glass to steel structures in automotive applications. These types of adhesives recently became, in new and improved formulations, good candidates for FRP/metal structural bonding. To date there are several structural adhesive types tailored for specific applications. The list of those adhesives is exhaustive, and providing detailed information on those is beyond the scope of this chapter.

The use of adhesive fracture mechanics is one of the most common and useful type of analysing a single-lap joint, taking into consideration the main parameters that influence the failure mode, like the joint geometry and the properties of adherends and adhesives. One of the analytical models was first proposed by Volkersen in 1938 [1] also known as the "shear-lag model". The adhesive shear distribution τ is given by

$$\tau = \frac{P\omega}{2b} \cdot \frac{\cosh(\omega x)}{\sinh\left(\frac{\omega l}{2}\right)} + \left(\frac{t_t - t_b}{t_t + t_b}\right) \cdot \left(\frac{\omega l}{2}\right) \cdot \frac{\sinh(\omega x)}{\cosh\left(\frac{\omega l}{2}\right)},$$

where $\omega = \sqrt{\frac{G_a}{E t_t t_a}\left(1 + \frac{t_t}{t_b}\right)}$.

The reciprocal of ω has units of length and is the characteristic shear-lag distance, a measure of how quickly the load is transferred from one adherend to the other. t_t is the top adherend thickness, b_t is the bottom adherend thickness, a_t is the adhesive thickness, b is the bonded area width, l is the bonded area length, E is the adherend modulus, a G is the adhesive shear modulus, and P is the force applied to the inner adherend. The origin of x is the middle of the overlap and is shown in Fig. 5.1.

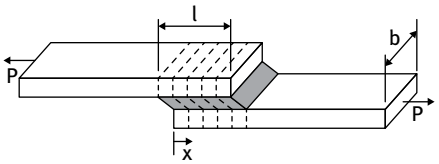

Fig. 5.1: Volkersen model.

The model was then further extended by Goland and Reissner [2], who were the first to consider the effects due to rotation of the adherends; see Fig. 5.2.

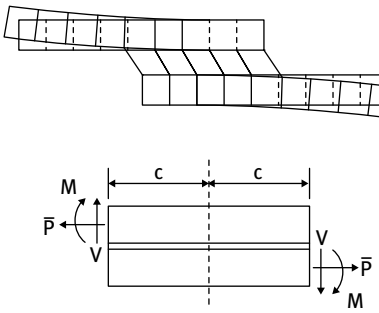

Fig. 5.2: Goland & Reissner model.

The adhesive shear distribution τ according to Goland and Reissner is given by

$$\tau = -\frac{1}{8}\frac{\overline{P}}{c}\cdot\left\{\frac{\beta c}{t}(1+3k)\frac{\cosh\left(\frac{\beta c}{t}\frac{x}{c}\right)}{\sinh\left(\frac{\beta c}{t}\right)}+3(1-k)\right\},$$

where P is the applied tensile load per unit width, c is half of the overlap length, t is the adherend thickness, and k is the bending moment factor given by

$$k = \frac{\cosh(u_2 c)}{\cosh(u_2 c)+2\sqrt{2}\sinh(u_2 c)},$$

where $u_2 = \sqrt{\frac{3(1-\nu^2)}{2}}\frac{1}{t}\sqrt{\frac{\overline{P}}{tE}}$; $\beta^2 = 8\frac{G_a}{E}\frac{t}{t_a}$ and ν is the Poisson's ratio.

Although the work of Volkersen and Goland and Reissner was a major step forward in stress analysis of adhesively bonded joint, it faces several limitations. Some analytical models are difficult to be incorporated because the analysis becomes very complex, so most of the analyses are linear elastic for both adherends and adhesive. Regarding the conditions of applicability and the stresses considered, the suitable model can be applied. In a case where the joint bending is not neglected and the adhesive is brittle, Volkersen's analysis is sufficient, but when yield and peel stresses of

the adhesive and/or the adherends are under consideration, a more complex model is necessary.

The analysis by Goland and Reissner for the single lap joint has been generalized by Bigwood and Crocombe [3, 4], so that it can be applied to an arbitrary end loaded single overlap configuration and take account of adhesive nonlinear behavior. The resulting analyses can be applied to single lap joints as well as to many other configurations, as shown in Fig. 5.3.

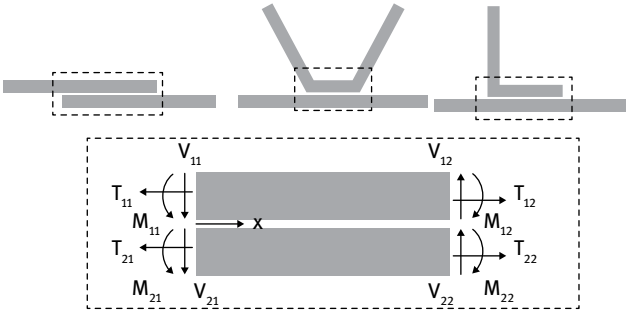

Fig. 5.3: Arbitrarily end loaded single overlap joint.

The resulting expressions for the adhesive shear and transverse direct stress in terms of the adhesive strains and hence substrate displacements are:

$$\tau = G\gamma = G\frac{(u_1 - u_2)}{\eta}, \quad s = E\varepsilon = E\frac{(v_1 - v_2)}{\eta}$$

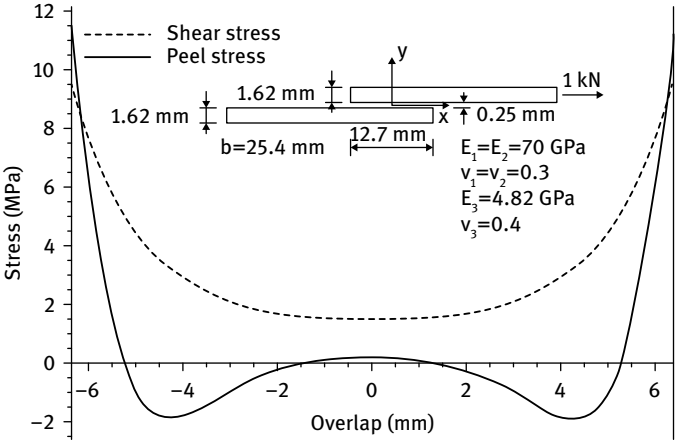

Fig. 5.4: Goland & Reissner's adhesive shear and peel stress distribution for aluminum alloy adherends and an epoxy adhesive.

Although the analyses of adhesively bonded joint failure by Volkersen and by Goland and Reissner are significant, they do have a number of limitations:

(1) the models do not take into account the variation of stress in the through thickness direction, especially the interface stresses which become significant when failure takes place close to the interface;
(2) the stress-free condition at the ends of the overlap are ignored, which results in overestimation of the stress at the overlap ends and tends to yield conservative failure predictions;
(3) the adherends are considered as thin beams, ignoring the through thickness shear and normal deformations. Adherend shear is particularly important in polymer composite adherends.

These limitations were addressed by Ojalvo and Eidinoff [5], who investigated the shear and normal deformations in the adherends. They extended the work of Goland and Reissner by using a complete shear strain/displacement equation for the adhesive layer to investigate the influence of adhesive thickness on the stress distribution. The adhesive shear stress was allowed to vary across the thickness, irrespective of the thickness of the adhesive, but the adhesive peel stress was maintained constant across the thickness. The adhesive longitudinal normal stress was neglected when compared with the adherend longitudinal normal stress. They concluded that the main difference between the theories that include and those that ignore adhesive thickness effects occurs at the ends of the overlap: the maximum shear stress increases and the peel stress decreases with the inclusion of this effect. The effect of the adhesive thickness is more significant with short overlaps, thick adherends, and stiff adhesives.

One of the drawbacks associated with adhesive joints is owed to the stress singularity which develops at the interface corner due to elastic mismatches, which may initiate failure at the interfaces. Failure can often initiate unexpectedly in a catastrophic manner under relatively low mechanical or thermal service loads.

It is, however, important to understand how cracks propagate, in terms of both their direction and directional stability, which requires more information about the stress state at the crack tip. Williams, in 1957 [6], developed an asymptotic stress expansion equation which characterises the stress state in the viscinity of the crack tip as follows:

$$\begin{bmatrix} \sigma_{xx} & \sigma_{xy} \\ \sigma_{xy} & \sigma_{yy} \end{bmatrix} = \frac{K_I}{\sqrt{2\pi r}} \cos\left(\frac{\theta}{2}\right) \begin{bmatrix} 1 - \sin\left(\frac{\theta}{2}\right)\sin\left(\frac{3\theta}{2}\right) & \sin\left(\frac{\theta}{2}\right)\sin\left(\frac{3\theta}{2}\right) \\ \sin\left(\frac{\theta}{2}\right)\sin\left(\frac{3\theta}{2}\right) & 1 + \sin\left(\frac{\theta}{2}\right)\sin\left(\frac{3\theta}{2}\right) \end{bmatrix}$$
$$+ \frac{K_{II}}{\sqrt{2\pi r}} \begin{bmatrix} -\sin\left(\frac{\theta}{2}\right)\left[2 + \cos\left(\frac{\theta}{2}\right)\cos\left(\frac{3\theta}{2}\right)\right] & \cos\left(\frac{\theta}{2}\right)\left[1 - \sin\left(\frac{\theta}{2}\right)\sin\left(\frac{3\theta}{2}\right)\right] \\ \cos\left(\frac{\theta}{2}\right)\left[1 - \sin\left(\frac{\theta}{2}\right)\sin\left(\frac{3\theta}{2}\right)\right] & \sin\left(\frac{\theta}{2}\right)\cos\left(\frac{\theta}{2}\right)\cos\left(\frac{3\theta}{2}\right) \end{bmatrix}$$
$$+ \begin{bmatrix} T & 0 \\ 0 & 0 \end{bmatrix} + O\left(\sqrt{r}\right),$$

where r and q are the polar coordinates, and K_I and K_{II} are the mode I and mode II stress intensity factors at the crack tip, respectively. The third term is nonsingular and acts parallel to the crack plane. This term is normally referred to as the "T-stress". A Cartesian coordinate is set at the crack tip and the x direction is that of the crack plane.

The stress state at the crack tip dictates the direction of crack propagation in homogeneous materials, and, following several different investigations over the past few years, three main criteria for the direction of crack propagation have received much attention:

(1) maximum opening stress criterion which dictates that the direction of cracking is perpendicular to the direction of maximum opening stress [7];
(2) mode I fracture criterion, which states that a crack will propagate along a path such that pure mode I fracture is maintained at the crack tip [8, 9];
(3) maximum energy release rate criterion, which states that the direction of crack propagation can be obtained by maximizing the energy release rate as a function of the angle of crack kinking [10].

Although these criteria were developed for homogeneous materials, they are also applicable to adhesively bonded joints, but care should be taken in dissimilar material joint interfaces, due to differences in fracture toughness in the vicinity of the interface.

In the Williams equation shown above, the T-stress is the most important term in determining the directional stability of crack propagation. If the T-stress in negative (compressive), a stable crack growth occurs. If the T-stress is positive (tensile), the crack growth is unstable, and the crack will deviate away from the original path.

The first criterion above related to the loading mode is most commonly used, since they all yield similar experimental results. This states that the direction of cracking depends on the ratio of mode II versus mode I fracture components at the crack tip. This in turn means that the crack path will be straight under mode I, but will deviate from a straight path under mixed mode loading.

The discussion of directional stability of cracks in adhesively bonded joints was described by Chai [11–13], who described the crack trajectory in the mode I delamination failure of graphite reinforced epoxy composite laminates and aluminum/epoxy bonds. In his work, the crack periodically alternated between the two interfaces with a characteristic length 3–4 times the thickness of the adhesive layer. More specifically, as the crack advanced, the crack propagated along one interface and then gradually deviated away with an increasing slope until the other interface was approached. An abrupt kink then occurred when the crack approached the opposite interface, and the crack stayed at the interface for a distance about 2–3 times the thickness of the adhesive layer before deviating from the interface again. This trajectory obviously reflects very directionally unstable crack propagation. However, it was later shown by other workers that the crack trajectory can be affected by the residual stress state in adhesive bonds [14] and the T-stress level [15, 16]

The J integral (a path independent integral) method to calculate the energy release rate (ERR), first presented by Rice in 1968 [17], has been used to assess the fracture behavior of adhesively bonded joints. For a monotonically loaded process, large-scale bulk inelasticities and nonlinear interfacial cohesive separations might be considered by the J-integral method. This approach has given rise to the development of cohesive zone models (CZM), and over the past 30 years numerous studies to investigate the nonlinear fracture of adhesively bonded joints have been carried out [18].

Parrinello et al. [19] developed an interface constitutive model in order to investigate the mechanical behavior of the internal adhesive layers in bonded substrates. Based on the damage mechanics theory this model captured the transition of the adhesive from the sound elastic condition (elastic behavior) to the entirely cracked one (frictional behavior). The interface intermediate mechanical properties during the formation and development of microcracks to macrocracks were calculated. Ouyang et al. [20] proposed a natural boundary condition based model for the local damage evolution of double cantilever beam specimens. Crack initiation and propagation, local deformation, and interfacial stress distribution were modelled as a function of the remote peel load using the bilinear cohesive laws. The nonlinear response during loading and unloading stages was predicted and verified using both experimental and numerical results.

Högberg [21] presented a traction-separation relation. The fracture process for different fracture parameters, such as fracture energy, strength, and critical separation in different mode mixities for unsymmetrical and mixed-mode double cantilever specimens, was modelled. The advantage of the proposed cohesive law is that it can be applied for mode I (peel), mode II (shear), and mode III (mixed mode) and model the fracture process without being altered for the different mode mixities.

Mixed mode double cantilever beam specimens were tested in [22] under shear and/or peel forces. Two different approaches of the J-integral expression were used to evaluate the energy dissipation in the failure process zone. The constitutive properties of the adhesive layers obtained by an inverse method were found to be coupled, i.e. the peel and shear forces depend on the peel and shear deformations.

5.1.2 Effect of adhesive thickness

The effect of thickness on the fracture performance of adhesively bonded joints has received limited attention over the past few years although there are some interesting pieces of work found in the literature where the global behavior of joints with different adhesive thicknesses have been carried out [23].

Fleck et al. [24] also showed that the T-stress is closely related to the specimen geometry i.e. the thickness of the adhesive layer and the thickness of adherends for DCB specimens. The T-stress increases with the thickness of the adhesive but decreases with the thickness of the adherend for this bonding geometry. This specimen geome-

try dependence of the T-stress level suggested a variation of the directional stability of cracks as the specimen geometry changes.

Chai [25] studied the mode II and III fracture of three different adhesive systems, i.e. two thermosetting resins, i.e. H3502 and BP-907, and PEEK, which is a semicrystalline thermoplastic. The adhesive bondline thickness varied up to a maximum value of a few microns, so that the bulk fracture behavior was exposed. The adherends were either an aluminum alloy or structural steel. For the thin bondline joints and for all three adhesives, the main source of energy consumption is due to shear yielding or distortion. As the adhesive thickness decreased, the fracture work, Gsc, decreased monotonically after it had reached a plateau. Another important conclusion extracted from this work was the coincidence of the forward and anti-plane shear components for all three cases of adhesive. Chai also incorporated particles into the epoxy adhesive aiming at the alteration of the fracture resistance [26]. DCB specimens with aluminum substrates bonded with two different types of adhesive under mode I, II, and III were evaluated. Shear strain increased with decreasing the bondline thickness, and it was higher for the FM1000 adhesive (elastic-plastic behavior) than for the F185 adhesive (strain hardening). G_{IIC} and G_{IIIC}, which were not affected by the bondline thickness, were found to coincide. In addition, when the bondline thickness was decreased as to approach the micrometre range, the three fracture energies obtained the same value.

Ikeda et al. [27] studied the J-integral and the near-tip stress of a crack in a joint with hard substrates, which were adhesively bonded with a ductile adhesive. Edge cracked plate (ECP) and tapered double cantilever beam (TDCB) types of specimens were tested. It was determined that stress distributions near a crack tip for both ECP and TDCB agreed with each other when the bond thickness was the same. However, a decrease of the bond thickness increased the stress ahead of a crack tip, resulting to the decrease of fracture toughness. Therefore, it was concluded that stress distribution did not depend on the shape of the specimens, but on the bond thickness and the J-integral.

Kafkalidis et al. [28] used an embedded-process zone (EPZ) to investigate the mode I parameters for plastically deforming adhesively bonded joints. Steel and aluminum substrates were bonded together with a thin layer of adhesive in order to manufacture symmetrical joints. It was found that the "intrinsic" toughness of these systems was not affected by either the adherend properties or the adhesive thickness. Cohesive zone elements [11] were also embedded in order to simulate the fracture process in adhesively bonded joints with steel substrates while varying the adhesive and adherend thickness. Plastic dissipation was found to be affected by the variation of the thicknesses, i.e. it increased when the adhesive thickness increased, until it decreased to reach a plateau for very thick adhesives. It also increased with the decrease of the adherend thickness.

Recently, work by Ji et al. [30] assessed the bondline thickness effect through simple DCB tests.

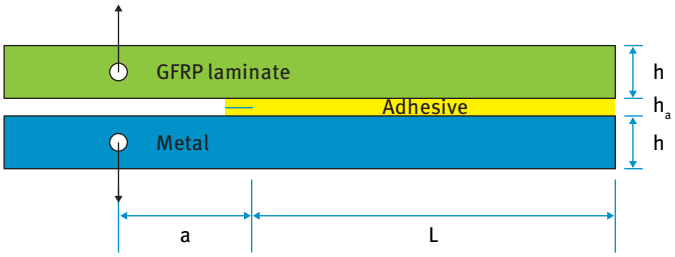

Fig. 5.5: Schematic of DCB specimen.

The analysis is based on the J-integral approach as developed by Rice [17]:

$$J = \int_{\Gamma} \left(Wdy - T\frac{\partial u}{\partial x} ds \right),$$

where $W(x,y)$ is the strain energy density, x and y are the coordinate directions, $T = n\sigma$ is the traction vector, n is the normal to the curve or path Γ, σ is the Cauchy stress, and u is the displacement vector. For the geometry of a DCB, Anderson and Stigh [31] developed an expression for the J-integral as follows:

$$J = \frac{(Pa)^2}{D} + P \cdot \theta_0 = P \cdot \theta_P,$$

where J is the energy release rate of the DCB specimen during crack initiation process, P is the global peel load at the loadline, D is the adherend's bending stiffness, θ_0 and θ_P are the relative rotations between the upper and lower adherends at the crack tip and at the loadline, respectively, and d is the crack tip opening or separation. The results of that work have shown that the fracture energy and the characteristic energy release rate both increase with increasing bondline thickness. However, it was found that the interfacial strength is high at small bondline thicknesses (< 0.1 mm) and then drops rapidly at a bondline thickness of 0.2 mm, while thereafter the increase of the adhesive thickness marginally reduces strength.

In contrast, work by Afendi et al. [32], although it demonstrated the effect of bond line thickness on failure stress, failed to show any effect on the fracture performance of bonded joints where J_{IC} remained constant for bond line thicknesses from 0.1 mm to 1.2 mm. Afendi et al. based their work on the analysis carried out by Akisanya et al. [33], who introduced the effects of the interface corner toughness H_C , which is described through a parametric expression of the form

$$H_C = \sigma_C t^q Q(\alpha, \beta),$$

where Q is a nondimensional constant function of the material elastic parameters, t is the interface thickness, σ_C is the applied stress at the free corner, and q is a constant.

Despite extensive work being carried out, the mechanisms of the dependency of joint strength and fracture on bondline thickness are not yet clarified.

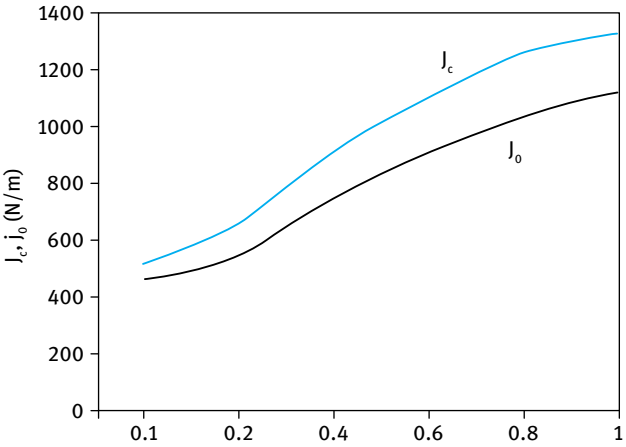

Fig. 5.6: Variation of J_0 and J_c with bondline thickness [31].

5.1.3 Carbon nanotube-enhanced adhesively bonded joints

In the past decades several research works have been carried out focusing on the effects of incorporating nanoparticles in polymers. By tailoring the adhesive properties, a stronger interfacial bonding between the matrix and the filler can be achieved, and this potentially leads to an increased load-bearing capability of the joint [34–37].

Various nanofillers have been used up to now in order to improve the adhesive properties of the joint. In [38] the effect of nano-SiC particles was evaluated in terms of mechanical and thermal properties of both lap joints and bulk matrix. A comparison of the micro- and nano-SiC was also investigated, with the nano-SiC composites having better properties. Lap shear strength was improved, when the adhesive was reinforced with silane treated SiC particles reaching a maximum value at 20 wt.%. A further increase of the particle content though led to a decrease of the lap shear strength.

Yu and Wang [39] added 10 wt.% of various particles, such as Al, Ag, and Ni (microsized) and Ag and Al (nanosized) into the neat resin in order to investigate their effect on wear rate and the several mechanisms of wear, such as deformation, delamination, and adhesion. The presence of Ag particles increased the wear rate of polyethylene (LPDE) when compared to neat resin, whereas the Al particles decreased. Nanoparticles seemed to be again more effective than microparticles.

Another type of nanofiller which is also used as reinforcement is carbon nanotubes (CNTs), due to their remarkable mechanical, thermal, electrical, and optical properties. In general, polymer-based nanocomposites exhibit much better mechanical, thermal, and multifunctional properties compared to those of the polymer matrices reinforced with microparticles. However, CNTs have also been used in adhesively bonded joints to enhance their mechanical behavior. Srivastava [40] bonded carbon/carbon and carbon-silicon carbide composites using both pure epoxy resin

and resin reinforced with 3 wt.% of CNTs. He reported that CNTs increased the joint strength and fracture toughness of the joints when compared to values obtained from the joints bonded with neat resin.

5.1.3.1 Toughening mechanisms

The addition of nanofillers to base adhesive formulations generally improves the modulus and mechanical strength. However, the main objective in these cases is to increase fracture toughness without any decrease of the adhesive characteristics. The increase in fracture toughness is often due to different toughening mechanisms which take place during the test. According to Gojny et al. [41], the toughening mechanisms that arise when CNTs are added into the matrix act at two different dimensional levels, i.e. the micro- and nanolevels. Crack pinning, crack deflection, and crack blunting are considered to be micromechanical mechanisms. Other mechanisms, such as pullout, interfacial debonding, void nucleation, and crack bridging, do exist in the microlevel; however, they can occur at the nanolevel as well.

Many researchers have investigated these toughening mechanisms in order to determine the relationship between the microstructure and fracture behavior. A brief review to explain how the CNT composite performance is affected is described below.

During the *crack-pinning mechanism* particles arrange in lines and act as obstacles for the crack front. Therefore, the crack front has to bow locally between the filler particles in order to pass through the line they form (Fig. 5.7). The particles are considered as toughening agents, because the crack front remains pinned at them resulting to an increase of the crack length. Secondary cracks can also be generated which coalesce after passing the particles [42]. As the strain energy increases, local step fracture occurs, and the pinned points are released, creating a "tail-like" feature on the fracture surface. During this process the propagation rate is slowed down, which finally leads to an increase of the fracture toughness due to the absorbed amount of energy.

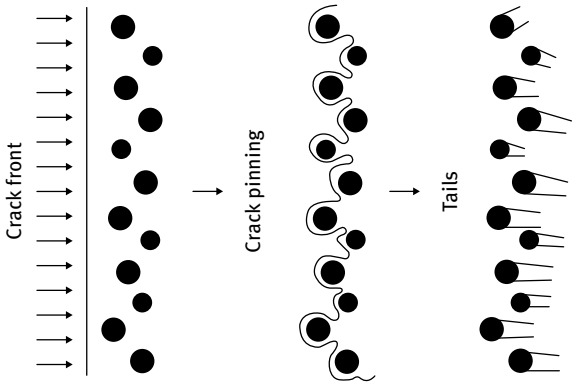

Fig. 5.7: Crack pinning process.

Faber and Evans [43] proposed another mechanism, called the *crack-path deflection mechanism*, which can also contribute to the improvement of the fracture toughness. According to this mechanism, the particles cause the crack to deviate from its original path. As the crack front approaches the particle/matrix interface, the crack is forced to change direction and pass around them along the interface. This deflection continuously changes the local stress state from mode I (crack opening) to mixed-mode. Therefore, more energy is absorbed to propagate a crack under mixed mode conditions than under pure mode I, which results in a higher fracture toughness of the material. Although this mechanism does not seem to depend on the particle size, it is believed that uneven spacing provides better results than uniform spacing [44, 45].

A key factor that greatly affects the toughening mechanisms is the nature of the interface region between the particle and the matrix. The interface must be of sufficiently low toughness, so that the particle will not be able to slide both too easily and with too much difficulty. In the case of a very strong bonding between the matrix and the CNT, fracture of the outer layer of the tube or even a complete rupture of the CNT can occur.

When the CNT/matrix bonding is weaker, another toughening mechanism called *pullout* (Fig. 5.8(a)) may be favored. In this case the CNT is pulled out of the matrix leading to a partial *interfacial debonding* and enabling the p*article bridging mechanism* (Fig. 5.8(b)), where the particles are stretched between the edged of the propagating crack, and therefore, more energy is absorbed prior to failure.

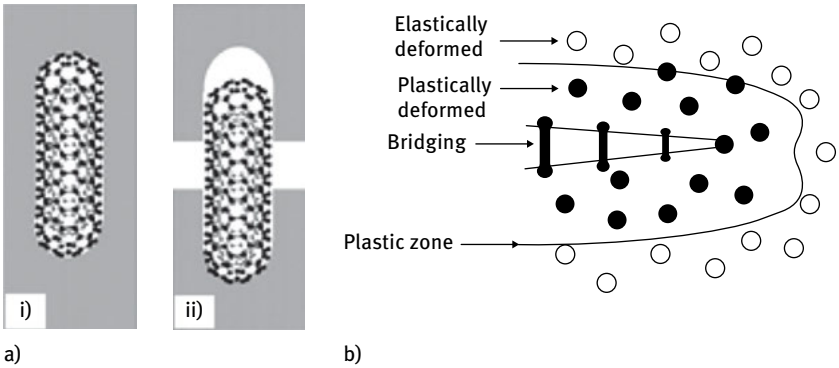

a) b)

Fig. 5.8: (a) Pullout (i) Initial state of the CNT (ii) Pullout caused by CNT/matrix debonding in case of weak interfacial adhesion, and (b) Crack Bridging

Microcracks, which can be created close to the crack tip, are able to reduce the stress intensity, because they allow the residual stress release resulting to the fracture toughness improvement. Certain size and spatial distributions of microcracks in the vicinity of the main crack tip act as a hindrance to the crack and reduce the crack propagation rate.

Another mechanism that might occur is *crack blunting* (Fig. 5.9). During crack propagation, macromolecular chains in the vicinity of the crack tip are stretched and broken. The initial sharp crack becomes more and more blunted as a result of the formation of a plastic zone and decohesion of particles. The stress concentration effect at the crack tip becomes lower and the crack is slowed down.

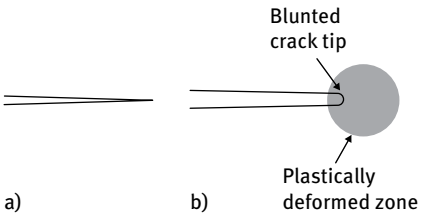

Fig. 5.9: Crack Blunting; (a) the crack at the beginning, (b) the blunted crack

Particles may also cause localized *plastic deformation* of the polymer matrix [46] (i.e. shear banding and crazing) and as a result enhance the fracture toughness. Shear banding is a narrow zone of intense shearing strain, usually of plastic nature, developed during severe deformation of a glassy polymer and results in partial orientation of the polymer chains [47]. Crazes are microscopic regions of highly localized plastic deformation similar to those developed on a macroscopic scale in glassy polymers. Crazing occurs in regions of high hydrostatic tension, or in regions of high localized yielding, which leads to the formation of microvoids (Fig. 5.10) oriented parallel to the tensile direction. If an applied tensile load is sufficient, these crazed regions elongate and break, causing the microvoids to grow and coalesce and cracks begin to form. Inclusion of rigid particles induces stress concentrations and alters the local stress state, which favors local plastic deformation. Because of the large number of particles in nanocomposites, potentially more plastic deformation may exist in these systems than in the unfilled polymer, leading to higher fracture toughness.

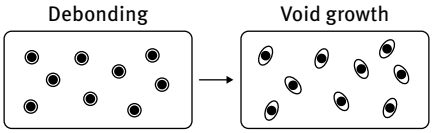

Fig. 5.10: De-bonding and Void-Growth mechanism.

Despite the various toughening mechanisms proposed by different researchers, it is difficult to explain an experimental result based only on one theory. Fracture is a complex phenomenon, and more than one of the mechanisms that were described above may take place at the same time.

The aforementioned toughening mechanisms that change the properties of the CNT/epoxy polymer can also affect the joint performance, when this polymer is used as the adhesive. Hsiao et al. [48] investigated the mechanical properties of a CFRP (carbon fiber reinforced polymer) joint with CNT/epoxy adhesive. It was found that the shear strength was increased by 31.2 % and 45.6 %, when 1 % and 5 wt.% MWCNTs, respectively, were added into the epoxy. This increase is related to the enhanced mechanical properties of the nanoreinforced adhesives and the change of the failure mode of joints. The failure mode of the bonded joints with nonmodified epoxy adhesive was adhesive, i.e. occurred at the epoxy along the bonding interface and no significant damages were observed on the composite adherends. In contrast, the failure mode changed to cohesive in the case of nanoreinforced adhesive. The nanotubes effectively transferred the load to the adherends, leading to the composite failure.

5.1.3.2 Functionalization and dispersion

It has been reported in many studies that after the addition of CNTs into the matrix, many properties of the material are improved. In [46], the average fracture toughness of 1 wt.% and 3 wt.% MWCNT/epoxy composites is 1.29 and 1.62 times that of pure epoxy respectively, and the 0.5 wt.% MWCNT/epoxy composite fatigue lives are 10.5 and 9.3 times of the average fatigue life of neat epoxy. However, CNT addition into polymers does not always improve the properties of the composite material. There are also studies confirming that the increase of some of the properties is not that significant, or it does not exist at all, especially when the weight percentage of the CNTs is increased more than a certain value. In [49], the experimental results reveal that varying the weight percentage of the nanofillers into the epoxy adhesive favorably influences the shear strength and modulus. On the other hand, the results also indicate that increasing the amount of the nanofillers beyond a certain weight fraction, a drop in the values of the properties is observed.

This inconsistency among the results in different studies may be attributed to the factors that determine the CNT performance. These factors are the state of dispersion and orientation of CNTs into the matrix. The interaction of CNT with the matrix as well as the interface between the nanoparticles and the matrix also play an important role. Uniform CNT dispersion is very challenging, because as-produced CNTs are often held together in bundles by strong van der Waals forces. Many methods have been developed to assist dispersion, and they can be generally classified [29] into three categories.

(1) Direct mixing: CNTs are dispersed in the polymer matrix by a mechanical force, such as shear-intensive mechanical stirring using a dissolver disk or ultrasonication [50]. However, the quality of dispersion is not always satisfactory and if either too aggressive or long sonication takes place, CNTs can be seriously damaged.
(2) Chemical surface modification: treatment of CNTs with strong acids, such as nitric acid, or with other strong oxidizing agents, such as $KMnO_4/H_2SO_4$. The downside

of this method is that the oxidative treatment tends to disrupt the conjugated electronic structure, shorten the CNTs, and deteriorate their electrical and mechanical properties.

(3) A third component is added to assist the dispersion of CNTs in solvents and polymer matrices. The third component might be surfactants, polyelectrolytes, or surfactant-like block copolymers [54]. These chemicals are beeing adsorbed onto the walls of CNTs during sonication, and the dispersion is stabilized by repulsive electrostatic interactions between the surfactants adsorbed on nanotubes. The use of block copolymer Disperbyk 2150 (alkylammonium salt of a low-molecular weight polycarboxylic acid polymer) was investigated in [51] and [52] and found to improve dispersion.

Konstantakopoulou and Kotsikos [55] have also reported a beneficial effect of introducing multiwall carbon nanotubes (MWCNT) in epoxy resin to bond steel to glass-reinforced composite joints. They evaluated several wt.% contents of MWCNTs in epoxy, and an improvement on shear strength was found in all cases. An optimum strength was achieved with a MWCNT content of 0.1 % (Fig. 5.11).

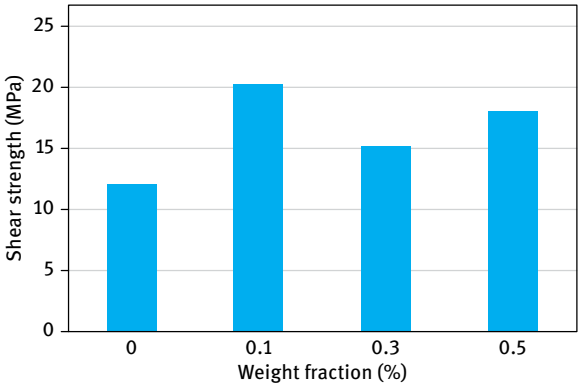

Fig. 5.11: Effect of addition of MWCNT (%wt) on the failure strength of lap shear joints.

By examining the fracture surfaces of the single lap joints, a change in the failure mode was also observed. In the case where the adhesive is pure epoxy resin, the joints failed adhesively (Fig. 5.12(a)), but after the addition of MWCNTs, this failure mode changed to cohesive where parts of the adhesive are on both substrate surfaces (Fig. 5.12(b,c)). This suggests that CNTs change the failure mechanism leading the crack to move from one adhesive/adherend interface to the opposite interface by propagating through the adhesive layer.

It was noted, however, that there is a large scatter observed in the experimental results. This was attributed to insufficient dispersion of the MWCNTs of the results.

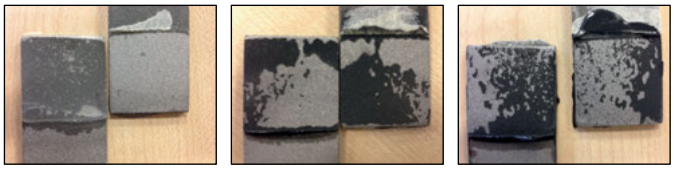

(a) (b) (c)

Fig. 5.12: Adherend surfaces after failure: (a) epoxy resin, (b) 0.1 CNT wt.%, (c) 0.3 CNT wt.%.

Examination of samples of adhesive in a scanning electron microscope (SEM) have shown regions of agglomeration of MWCNTs that act as initiators of cracks (Fig. 5.13).

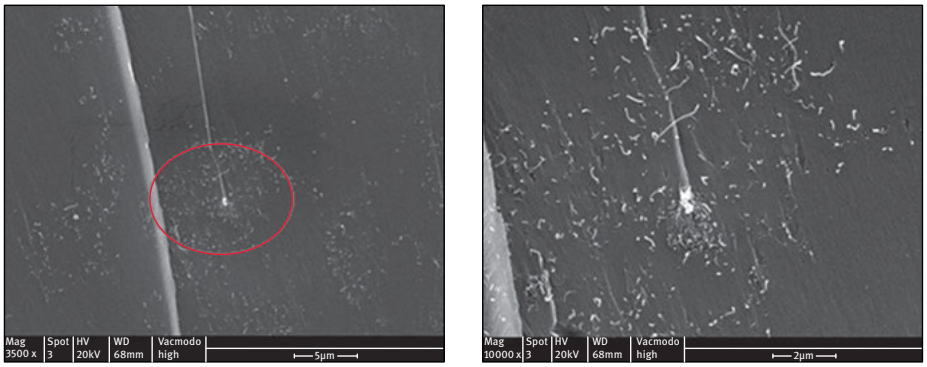

(a) (b)

Fig. 5.13: Scanning electron micrographs of MWCNT filled epoxy resin (RS-L135) fracture surface showing aggregated area (0.3 wt.% and sonication time = 30 min): (a) ×3,500 magnification, (b) ×10,000 magnification.

5.2 Conclusions

The failure prediction of adhesively bonded joints is a complex undertaking as there are several parameters that can cause premature failure. Recent development in nanotechnologies have shown that the performance of adhesively bonded joints can be improved by the introduction of nanoparticles in the adhesive. This has increased the complexity of the fracture mechanics assessment of such joints, since the presence of nanoparticles introduces further parameters that influence crack initiation and propagation. Despite theories being available to describe how nanoparticles enhance bond strength, there is still a lot of work to be done to create reliable failure models for predicting failure of nanofilled adhesives. Furthermore, the issue of adequate dispersion of the nanoparticles needs to be addressed in more detail as it introduces significant scatter in the experimental results and also uncertainties for industrial applications.

References

[1] Vokersen O. 1938. Nietkraftverteiligung in Zugbeanspruchten Nietverbindungen mit konstanten Laschenquerschnitten, *Luftfahrtforschung* **1**, 15–41.

[2] Goland M, Reissner E. 1944. The Stresses in Cemented Joints, *Journal of Applied Mechanics* **11**, A17–A27.

[3] Bigwood DA, Crocombe AD. 1989. Elastic Analysis and Engineering Design Formulae for Bonded Joints, International Journal of Adhesion and Adhesives **9**, 229–242.

[4] Bigwood DA, Crocombe AD. 1990 Non-Linear Adhesive Bonded Joint Design Analyses, *International Journal of Adhesion and Adhesives* **10**, 31–41.

[5] Ojalvo IU, Eidinoff HL. 1978. Bond Thickness Effects upon Stresses in Single Lap Adhesive Joints, *AIAA Journal* **16**(3), 204–211.

[6] Willams ML. 1957. On the stress distribution at the base of a stationary crack, *J. Applied Mechanics* **24**, 109–114.

[7] Ergodan VF, Sih GC. 1963. On crack extension in plates under plane loading and transverse shear, Trans. ASME, *J. Bas. Engng*. **85**, 519–527.

[8] Goldstein RV, Salganik RL. 1974. Brittle fracture of solids with arbitrary cracks, *International Journal of Fracture* **10**(4), 508–515.

[9] Cotterell B, Rice JR. 1980. Slightly curved or kinked cracks, International Journal of Fracture **16**(2), 155–156.

[10] Palaniswamy K, Knauss WG. 1978. On the problem of crack extension in brittle solids under general loading, in S. Nemat-Nasser ed.), *Mechanics Today*, vol. 4, 87–148, Oxford, Pergamon Press.

[11] Chai H. 1984. The characterization of mode I delamination failure in non-woven, multidirectional laminates, *Composites* **14**(4), 277–290.

[12] Chai H. 1986. On the correlation between the mode I fracture of adhesive joints and laminated composites, *Engineering Fracture Mechanics* **24**(3), 413–431.

[13] Chai H. 1987. A note on crack trajectory in an elastic strip bounded by rigid substrates, *Int. J. Fracture* **32**, 211–213.

[14] Daghyani HR, Ye L, Mai YM. 1996. Effect of thermal residual stress on the crack path in adhesively bonded joints, *J. Materials Science* **31**, 2523–2529.

[15] Akisanya AR, Fleck NA. 1992. Analysis of a wavy crack in sandwich specimens, International *J. Fracture* **55** 29–45.

[16] 18. Akisanya AR, Fleck NA. 1992. Brittle fracture of adhesive joints, *Int. J. Fracture* **58**, 93–114.

[17] Rice JR. 1968. *A Path Independent Integral and the Approximate Analysis of Strain Concentration by Notches and Cracks*. J. Applied Mechanics **35**(2), 379–386.

[18] Wei Y, Hutchinson J. 1998. *Interface strength, work of adhesion and plasticity in the peel test. Int. J. Fracture* **93**(1–4), 315–333.

[19] Parrinello F, Failla B, Borino G. 2009. *Cohesive–frictional interface constitutive model*. International Journal of Solids and Structures **46**(13), 2680–2692.

[20] Ouyang Z, Li G. 2009. Local damage evolution of double cantilever beam specimens during crack initiation process: a natural boundary condition based method, *J. Appl. Mechanics* **76**(5), 051003.

[21] Högberg JL. 2006. Mixed mode cohesive law, *Int. J. Fracture* **141**(3–4), 549–559.

[22] Högberg JL, Sørensen BF, Stigh U. 2007 Constitutive behaviour of mixed mode loaded adhesive layer, *Int. J. Solids and Structures*, **44**(25–26), 8335–8354.

[23] Kinloch AJ, Shaw SJ. 1981. The fracture resistance of a toughened epoxy adhesive. J. Adhesion **12**, 59–77.

[24] Fleck NA, Hutchinson JW, Suo Z. 1991. Crack path selection in a brittle adhesive layer, Int. *J. Solids and Structures* **27**(13), 1683–1703.
[25] Chai H. 1988. Shear fracture, *Int. J. Fracture* **37**(2), 137–159.
[26] Chai H. 1995. *Deformation and fracture of particulate epoxy in adhesive bonds*. Acta Metallurgica et Materialia, **43**(1), 163–172.
[27] Ikeda T, et al. 1999. Failure of a Ductile Adhesive Layer Constrained by Hard Adherends, *J. Engineering Materials and Technology* **122**(1), 80–85.
[28] Kafkalidis MS, et al. 2000. Deformation and fracture of adhesive layers constrained by plastically-deforming adherends, *J. adhesion science and technology* **14**(13), 1593–1607.
[29] Pardoen T, et al. 2005. Constraint effects in adhesive joint fracture, *J. Mechanics and Physics of Solids* **53**(9), 1951–1983.
[30] Ji G, et al. 2010. Effects of adhesive thickness on global and local Mode-I interfacial fracture of bonded joints, *Int. J. Solids and Structures* **47**(18–19), 2445–2458.
[31] Andersson T, Stigh U. 2003. The stress-elongation relation for an adhesive layer loaded in peel using equilibrium of energetic forces, *Int. J. Solids and Structures Elsevier* **41**, 416–418.
[32] Afendi M, Teramoto T. 2010. Fracture toughness test of epoxy adhesive dissimilar joint with various adhesive thicknesses, *J. Solid Mechanics and Materials Engineering* **4**(7), 999–1010.
[33] Akisanya AR. 2003. Initiation of fracture at the interface corner of bi-material joints, *Mech Phys Solids* **51**, 27–46.
[34] Hasegawa N, Okamoto H, Kato M, Usuki A, Sato N. 2003. Nylon-6/Na-montmorillonite nanocomposites prepared by compounding Nylon-6 with Na-montmorillonite slurry, *Polymer* **44**(10), 2933–2937.
[35] Huang JC, Qian XF, Yin J, et al. 2001. Preparation of soluble polyimide-silver nanocomposites by a convenient ultraviolet irradiation technique , *Mater. Chem. Phys.* **69**, 172.
[36] Reynaud E, Gauthier C, Perez J. 1999. *Rev. Metall.* **96**, 169.
[37] Yu LG, Yang SR, Wang HT. 2000. An investigation of the friction and wear behaviors of micrometer copper particle- and nanometer copper particle-filled polyoxymethylene composites, *J. Appl. Polym. Sci.* **77**, 2404.
[38] Zhou T, et al. 2008. Study on Mechanical, Thermal and Electrical Characterizations of Nano-SiC/Epoxy Composites, *Polym. J.* **41**(1), 51–57.
[39] Irwin P, Zhang W, Cao Y, Fang X, Qi Tan D. 2000. Wear Resistance and Wear Mechanisms in Polymer+Metal Composites, *Appl. Polym. Sci.* **77**, 2404.
[40] Srivastava VK. 2011. Effect of carbon nanotubes on the strength of adhesive lap joints of C/C and C/C–SiC ceramic fibre composites, *Int. J. Adhesion and Adhesives* **31**(6), 486–489.
[41] Gojny FH, et al. 2005. Influence of different carbon nanotubes on the mechanical properties of epoxy matrix composites – A comparative study, *Composites Science and Technology* **65**(15–16), 2300–2313.
[42] Irwin P, Zhang W, Cao Y, Fang X, Qi Tan D. 2009. Mechanical and Thermal Properties, in Nelson, J. Keith (ed.). *Dielectric Polymer Nanocomposites*, chap. 6, Springer Science+Business Media.
[43] Evans KT, Faber AG. 1983. Crack deflection Process – 1. Theory, *Acta Metallurgica* **31**(4), 577–584.
[44] Adams RD, Comyn J. 2000. Joining using adhesives, *Assembly Automation* **20**(2), 109–117.
[45] Prolongo SG, Gude MR. 2010. Ureña A., Nanoreinforced Adhesives, in: Kumar A (Ed.), *Nanofibres* **3**, InTech Publisher, 438.
[46] Yu N, Zhang ZH, He SY. 2008. *Fracture toughness and fatigue life of MWCNT/epoxy composites*. Materials Science and Engineering: A **494**(1–2), 380–384.
[47] Barenblatt GI. 1972. Deformation and Fractuere of High Polymers, in: Kausch, Hassell, Jaffe (Eds.), New York: Plenum Press, 239–258.

[48] Hsiao K-T, Alms J, Advani SG. 2003. Use of epoxy/multiwalled carbon nanotubes as adhesives to join graphite fibre reinforced polymer composites, *Nanotechnology* **14**, 791.
[49] Meguid SA, Sun Y. 2004. On the tensile and shear strength of nano-reinforced composite interfaces, *Materials & Design* **25**(4), 289–296.
[50] Chen H, et al. 2007. Dispersion of carbon nanotubes and polymer nanocomposite fabrication using trifluoroacetic acid as a co-solvent, *Nanotechnology* **18**(41), 415606.
[51] Frømyr TR, Hansen FK, Olsen T. 2012. The Optimum Dispersion of Carbon Nanotubes for Epoxy Nanocomposites: Evolution of the Particle Size Distribution by Ultrasonic Treatment, *J. Nanotechnology*, Article ID 545930, 1–14.
[52] Zhao L, Gao L. 2003. Stability of multi-walled carbon nanotubes dispersion with copolymer in ethanol, *Colloids and Surfaces A: Physicochemical and Engineering Aspects* **224**(1–3), 127–134.
[53] Li Q, Zaiser M, Koutsos V. 2004. Carbon nanotube/epoxy resin composites using a block copolymer as a dispersing agent, *Physica status solidi (a)* **201**(13), R89–R91.
[54] Cho J, Daniel IM, Dikin DA. 2008. Effects of block copolymer dispersant and nanotube length on reinforcement of carbon/epoxy composites, *Composites Part A: Applied Science and Manufacturing* **39**(12), 1844–1850.
[55] Konstantakopoulou M, Kotsikos G. 2015. Failure Mode and Strength of FRP/Steel Joints Bonded with MWCNT Epoxy Adhesive, International Conference on Engineering Against Failure (ICEAF IV), Skiathos.

Index

adhesion, 68
adhesive bonding, 53, 58, 104
adhesive thickness, 109
affect, distribution of nanoparticle, 29
agglomeration, 43, 118
aggressive environment, 86
Al+CFRP galvanic system, 90
alloying element, 55
aluminum, 110
– alloy, 23

barrier coating, 81
bentonite, 93
bilinear cohesive law, 109
brittle, 105
– intermetallic, 58

carbon nanotube, 23, 49, 64, 112
cathodic protection, 61
cavities, 37
ceramic particle, 26
chemical surface modification, 116
chemical vapor deposition, 26
CNT, 114
– cluster, 33
coating, 66, 68
– defect, 83
– process, 82
composition, 54
containers, 84
– β-cyclodextrin fillers, 84
– ion exchangers (anion and cation), 84
– oxide nanoparticles, 84
corrosion, 54, 55
– crevice, 56
– degradation, 73
– exfoliation, 55
– galvanic, 55
– intergranular, 55
– local galvanic, 55
– localized, 55
– pitting, 55
– resistance, 96
– stress-induced, 55
corrosion inhibitors, 66, 68, 77, 85
– 1,2,3-benzotriazole (BTA), 85
– Cerium (III), 85
– nitrate ($Ce(NO_3)_3$), 85
crack, 58, 109
– blunting, 113, 115
– deflection, 113
– initiation, 109
– propagation, 109
– tip, 108
current, 89
– maximal anodic, 89
– maximal cathodic, 89
cyclic test, 57

damage mechanic, 109
direct mixing, 116
dispersion, 116
dissimilar alloy, 24
dissimilar material, 54, 63, 73, 103
ductile fracture, 37
ductility, 47
durability, 58
dynamic, 32
dynamic recrystallization, 24

EDS, 33
elastic modulus, 37, 39, 48
electrochemical activity, 54
encapsulation, 91

failure, 37
failure mode, 104
fatigue life, 116
fatigue loading, 57
fractography, 47
fracture, 37
– brittle, 47
– ductile, 47
– mechanics, 104
– toughness, 110
friction stir processing, 23
friction stir welding, 23, 59, 68
functionalization, 116
functioning kinetics, 88

galvanic cell, 55
galvanic compatibility, 96
galvanic corrosion, 74
glue bonding, 68
grain size, 31
green process, 25

Hall–Petch relation, 34
hardness, 34
hybrid assembly, 63
hybrid structure, 74
hydrogen embrittlement, 56
hydrogen-induced cracking, 56

indentation, 29
inhibition efficiency, 90
inhibitor efficiency, 88
integrated ionic currents, 89
interface, 103, 114
interfacial zone, 56
intergranular corrosion, 59
intergranular dissolution, 60

J-integral, 109, 111
joined assembly, 56
joining, 53
joint strength, 111

layered double hydroxides, 92
lifetime of joined component, 62
light design, 73
lightweight metals, 54
local deformation, 109
local values, 48
localized plastic deformation, 115
localized technique SVET, 87

macrostructure, 31
magnesium, 74
material mixing, 32
mechanical integrity, 68
mechanical joining, 53
mechanical property, 26
mechanical stresses, 54
metal matrix composite, 23
microhardness distribution, 34
microstructure, 25, 59
multielectrode, 77
multifunctional coating, 93

nanocomposite, 112
nanocontainers, 84
nanohardness, 38
nanoindentation, 28

onion ring, 43
optimization of welding, 29
optimum welding parameter, 29
oxidation, 56, 86
oxide layer, 54

passes, direction of FSW, 29
passive protection, 80
percentage of elongation, 37
plasma electrolytic oxidation, 67
polarization resistance, 77
polymer sealant, 81
pore, 58
premature failures, 96
properties, 54
protective coating, 85
protectiveness, 54

reactivity, 54
reduced elastic modulus, 39
residual stress, 114

self-healing, 94
– active, 84
SEM, 33
shear-lag model, 104
silane, 84
smart nanocontainers, 97
sol-gel, 84
steel, 110
– fastener, 74
stress corrosion cracking, 61
stress intensity factors, 108
stress singularity, 107
structural design, 103
surface treatment, 61, 83
synergistic parameter, 90

Taguchi, 29
– method, 41
tensile specimen, 28
tool pin, 25
tool rotational, 29
toughening mechanisms, 116

transgranular dissolution, 55
travel speed, 29

ultimate tensile strength, 37

verification, 94
Vickers microhardness, 28

weight reduction, 73
welding, 53
welding zone
– heat affected, 34
– thermomechanically affected, 34

yield stress, 37